On the interaction of ocean waves and turbulence

by

José F. Beyá

A thesis submitted for the degree of Master of Engineering by Research

School of Civil and Environmental Engineering

The University of New South Wales

Australia

December, 2010

ORIGINALITY STATEMENT

'I hereby declare that this submission is my own work and to the best of my knowledge it contains no materials previously published or written by another person, or substantial proportions of material which have been accepted for the award of any other degree or diploma at UNSW or any other educational institution, except where due acknowledgment is made in the thesis. Any contribution made to the research by others, with whom I have worked at UNSW or elsewhere, is explicitly acknowledged in the thesis. I also declare that the intellectual content of this thesis is the product of my own work, except to the extent that assistance from others in the project's design and conception or in style, presentation and linguistic expression is acknowledged.'

COPYRIGHT STATEMENT

'I hereby grant to the University of New South Wales or its agents the right to archive and to make available my thesis or dissertation in whole or part in the University libraries in all forms of media, now or hereafter known, subject to the provisions of the Copyright Act 1968. I retain all proprietary rights, such as patent rights. I also retain the right to use in future works (such as articles or books) all or part of this thesis or dissertation. I also authorise University Microfilms to use the abstract of my thesis in Dissertations Abstract International (this is applicable to doctoral theses only). I have either used no substantial portions of copyright material in my thesis or I have obtained permission to use copyright material; where permission has not been granted I have applied/will apply for a partial restriction of the digital copy of my thesis or dissertation.'

AUTHENTICITY STATEMENT

'I certify that the Library deposit digital copy is a direct equivalent of the final officially approved version of my thesis. No emendation of content has occurred and if there are any minor variations in formatting, they are the result of the conversion to digital format.'

ABSTRACT

The interaction of ocean waves and turbulence is a fundamental process in the ocean. Understanding and prediction of wind-wave generation, propagation, breaking, non-linear interactions and extreme wave development are directly linked to this complex and not well understood phenomenon (Thorpe 2005). Despite its significance in ocean engineering, there are no complete theories that explain the influence of turbulence in these processes. Further, available laboratory and field observations are limited mainly due to the difficulty in measuring turbulence within a wave field, particularly in the region above the wave trough. Instead most engineering applications rely on parameterizations and formulas based on empirical relations and the linear wave theory, which potential flow assumption does not support turbulence (CEM2008, SPM84). This lack of understanding of the wave-turbulence interaction processes is in part responsible for inaccurate predictions that ultimately translate in higher failure risks, and infrastructure and operational costs for engineering and navigational assets.

In this investigation two new wave tank laboratory experiments have been developed to enhance present understanding on wave-turbulence interactions. The first experiment quantified the attenuation of deep water surface waves caused by rainfall induced subsurface turbulence. Significant challenges in the measurement and extraction of the turbulence statistics were overcome. Observations of near-surface velocity fluctuations revealed that wave attenuation rates induced by the unexpectedly weak rainfall-triggered turbulence were greater than previously anticipated by Teixeira and Belcher (2002). Measured near-surface velocity fluctuations are also in excellent agreement with Braun (2003) but contrast strongly with recent measurements by Zappa

et al. (2009) and well-established theories that predict high levels of rainfall induced subsurface turbulence (e.g. Ho *et al.* 2000).

The second experiment intended to verify a controversial and recently proposed laminar-turbulence transition produced under steep freely propagating deep water waves (Babanin and Haus 2009). This new finding has major implications that could dramatically change present understanding of ocean waves. Dye visualization experiments showed no evidence of turbulence unless wave steepness was large enough to produce breaking. Moreover, unique measurements of the Stokes drift and the Stokes harmonic coefficients showed remarkable agreement with high order irrotational Stokes theories. However, measured higher order Stokes coefficients were larger than the theoretical predictions. Nevertheless, general good agreement of the present observations with the irrotational theories is in contrast with the recent challenges by Monismith *et al.* (2007) who proposed the cancellation of the Stokes drift and inferred closed orbital particle paths in freely propagating waves.

ACKNOWLEDGEMENTS

The author would like to thank sincerely the help and support of the Water Research Laboratory staff and the financial support of Becas Bicentenario, CONICYT-Chile. The author is also indebted to Prof. Michael Banner for being a highly knowledgeable and experienced guide on this not always “laminar” journey and to Dr. William Peirson for his dedicated supervision, patience and indefatigable drive to overcome difficult challenges that arose.

DEDICATION

To my beloved parents, Marilyn and Francisco for their unconditional support and guidance in all my enterprises and adventures.

TABLE OF CONTENTS

LIST OF FIGURES

LIST OF TABLES

LIST OF SYMBOLS AND ACRONYMS

a = wave amplitude (amplitude of the first harmonic, infinitesimal waves).

ADV=acoustic Doppler velocimeter.

c= wave speed.

c_0=linear theory wave speed.

c_g=wave group speed.

d = water depth.

E= wave energy density (per unit of crest width).

E_0= initial wave energy density (per unit of crest width).

EF= energy flux per unit area.

EF_T= energy flux dissipated by subsurface turbulence per unit surface area.

EF_V= energy flux dissipated by viscous wave attenuation of rain waves per unit surface area.

EF_R= energy flux dissipated by turbulent wave attenuation of rain waves per unit surface area.

f=raindrop probability distribution

$g=9.81 m/s^2$, gravity acceleration.

H=wave height.

I=rainfall intensity

$k=2\pi/L$, wave number.

$k_T=2\pi/l$, wave number associated to the characteristic turbulence length (l).

$k_0=2\pi/L_0$, deep water linear wave number.

KEF_{rain}=rainfall kinetic energy flux per unit of surface area.

l=characteristic turbulence length.

L = *wave length.*

L_0 = *deepwater linear wave length.*

PIV=particle image velocimetry.

Re=mean flow Reynolds number.

Re_L=*turbulence Reynolds number.*

Re_W=*wave turbulence Reynolds number.*

Re_λ=*Taylor microscale Reynolds number.*

S_w=*wave spectral energy.*

t=time.

T = wave period.

$TKE=(u'^2+v'^2+w'^2)/2$=*turbulent kinetic energy per unit of mass.*

u=wave horizontal velocity

u'=x-component of velocity fluctuations associated to turbulence.

u_*=*friction velocity.*

U=*mean velocity profile.*

U_s=*Stokes drift mean velocity profile.*

$\bar{U}$= *mean depth averaged velocity.*

v'= y-component of velocity fluctuations associated to turbulence.

V_{drop}=*raindrop impact velocity.*

w=wave vertical velocity

w'=z-component of velocity fluctuations associated to turbulence.

x=horizontal coordinate along wave propagation direction coordinate.

y= horizontal coordinate across wave propagation direction coordinate.

z= vertical coordinate.

z_0=*roughness length.*

δ=*mean horizontal particle displacement.*

Δ=*wave attenuation coefficient.*

Δ_b= *viscous wave attenuation coefficient due to solid boundaries.*

Δ_R= *wave attenuation coefficient due to rainfall.*

Δ_s=*viscous wave attenuation coefficient due to the water surface.*

Δ_s^{clean}=*viscous wave attenuation coefficient due to a clean water surface.*

Δ_s^{imm}=*viscous wave attenuation coefficient due to an immobile water surface.*

Δ_T=*total wave attenuation coefficient.*

Δ_V= *wave attenuation due to viscosity*

ε=*turbulent kinetic energy dissipation rate per unit volume.*

θ=*surface tension in air-water interface.*

η=*water surface elevation.*

η_k=*Kolmogorov length microscale.*

κ=*0.41=Von Karman constant.*

λ_T=*Taylor length microscale.*

μ=*water dynamic viscosity.*

ν=*water kinematic viscosity.*

ξ=*kH/2, wave steepness*

ρ=*density of water.*

ρ_{air}=*density of air.*

τ= *shear stress*.

τ_k= *Kolmogorov time microscale.*

ϕ=*rain drop diameter.*

Φ=*wave velocity potential.*

Φ_k=*wave number velocity fluctuations spectra.*

$\omega=2\pi/T$, *wave angular frequency.*

ω_p= *wave angular frequency associated to the peak of the spectrum.*

ω_T=*angular frequency in velocity fluctuations spectra.*

$\Omega=\omega-k\bar{U}$, *angular frequency for waves propagating on a mean current,* $\bar{U}$.

1 INTRODUCTION

1.1 Motivation

The co-existence of waves and turbulence is a common phenomenon in the ocean, particularly during storms when waves and turbulence interact in an extremely intricate manner. Our present understanding of wave-turbulence interactions is relatively scant considering its importance in the prediction of extreme conditions in the ocean. Correct understanding of intense waves, surges and currents and their impact on environmental, engineering and navigational assets has significant implications in the assessment of potential human and material losses during severe storms.

Present calculation methods provide poor estimates of the wave hydrodynamics under these extreme conditions where engineering designs rely on broad parameterizations based mostly on empirical laboratory data that incorporate the effect of turbulence implicitly.

In spite of remarkable improvements that wave modelling has experienced in recent years, uncertainties in wave generation and dissipation parameterisations are still a major concern. Model reliability depends strongly on the adequate calibration of the parameters in the generation and dissipation terms. Research efforts in this area have not yet delivered a good understanding of the generation and dissipation processes fundamentally due to the mathematical and experimental complexity when dealing with waves and turbulence.

Further, the not uncommon occurrence of unpredictable deadly rogue waves impacting ships and coastal assets has brought to the surface the weakness of our capabilities in forecasting extreme wave conditions where complex phenomena such as

non-linear wave interactions, grouping, breaking and turbulence interact in an unknown fashion.

Hence, laboratory experiments providing new understanding on wave-turbulence interactions are necessary to progress present mathematical representations of the hydrodynamics and associated transport processes in the sea.

Figure 1-1. Photo of wave breaking, spray and white-capping in the ocean.

Figure 1-2. Photo of wave impact on an oil rig during rough seas.

1.2 Scope of the investigation

The main focus of this investigation is the study of wave attenuation caused by surface generated turbulence which is normally present in the wind-wave generation zone and during storms and breaking in the ocean. A secondary focus is on the existence of non-turbulent flow under waves and the validity of irrotational wave theories motivated on recent claims of a laminar-turbulent transition under freely propagating non-breaking waves. The work presented in this thesis is based on laboratory experiments.

1.3 Thesis outline

1) Chapter 2 presents the general theoretical background on which this investigation is based.
2) Chapter 3 describes the general experimental facilities, equipment and data processing methods.
3) Chapter 4 describes the specific background, measurement and data processing techniques used for the measurement of wave attenuation due to rainfall generated surface turbulence, followed by the presentation of the results, comparisons with other studies and a specific discussion.
4) Chapter 5 describes the specific background, measurement and data processing techniques used for the experimental proof of non-turbulent flow under freely propagating non-breaking waves, followed by the presentation of the results and a specific discussion.
5) Chapter 6 include conclusions and recommendations for future work arising from the findings of this investigation.

2 BACKGROUND

2.1 Wave phenomena

Water oscillations in the surface of the ocean are subject to a number of processes as they travel and approach the coast. These processes are commonly: generation, propagation, nonlinear wave interaction, refraction, shoaling, diffraction, reflexion, breaking and dissipation. Depending on the water depth (d) relative to the wave length (L) waves can be classified in: deep water, transitional water and shallow water. In this thesis focus will be centred on turbulence and deep water waves, which interaction is fundamental in the physics of the predominant processes in the open ocean: wind-wave generation, dissipation, nonlinear wave interaction, and breaking.

2.1.1 Airy (linear) theory

Linear wave theory is one of the cornerstones in coastal engineering (CEM2008). Most of the present understanding and representation of waves including the state of the art propagation models is based on its simple formulation (Tolman 2009).

Linear theory has been developed under the following assumptions (Wiegel 1964):

1. Invicid, homogenous, irrotational, incompressible flow.
2. Small amplitude waves ($ak \ll 1$, a is the wave amplitude, $k = 2\pi/L$, is the wave number).
3. Impermeable bed.
4. Uniform depth (flat bed).
5. Kinematic condition (a parcel of fluid at the surface remains at the surface).
6. Dynamic condition (pressure at the surface is constant).

7. Waves are long crested (infinitely wide, two dimensional).

The dispersion relation in equation (2-2) is derived from linear theory for the monochromatic wave represented in equation (2-1):

$$\eta = a\,sin(kx - \omega t) \tag{2-1}$$

$$\omega^2 = gk\,tanh(kd) \tag{2-2}$$

where, η is the water surface elevation, $\omega=2\pi/T$ is the angular frequency of the wave, x the horizontal coordinate, g the gravitational acceleration and t is time.

From (2-2) waves can be classified in: deep water ($kd>\pi$), transitional water and shallow water ($kd<0.25$).

The most relevant results for the present investigation are those for deep water monochromatic gravity waves (for which surface tension effects are negligible) as summarized in the following expressions:

The deep water linear dispersion relation:

$$\omega^2 = gk_0 \tag{2-3}$$

and the deep water velocity potential:

$$\phi = ace^{kz}\,sin(kx - \omega t) \tag{2-4}$$

where k_0 is the deep water linear wave theory wave number, $c=\omega/k$ the wave phase speed and z the vertical coordinate with origin in the still water level.

Other useful results that can be derived from the deep water wave linear theory are: the particle paths describe closed circular orbits centred at the mean depth, velocity magnitudes in an Eulerian frame of reference are constant and the wave energy density (E) is transported at the wave group velocity (c_g) which corresponds to half of c in deep water.

2.1.2 Stokes non-linear theories

When waves are steep, the assumption of small amplitude waves is not sufficient to explain observed wave behaviour. Thus, finite amplitude Stokes wave theories were developed to represent more realistically the observed shape of the surface elevation profile for steep waves, which differentiate themselves from the linear small amplitude sinusoidal shape by having sharper crests and flatter troughs (Stokes 1847). Although, only using linear theory results, Stokes (1847) also predicted that the particle paths of the fluid parcels become open with a forward drift in the direction of the wave propagation generating a mean forward velocity profile, the Stokes drift (U_s):

$$U_s(z) = (ak)^2 c \cdot e^{2kz} \tag{2-5}$$

Stokes theories include higher order terms of the dispersion relation, water elevation and velocity potential solutions derived from a Taylor series expansion on the wave steepness ($\xi=kH/2$, H is the wave height). Stokes theories are based on similar assumptions than the Airy theory. Wiegel (1964), Kinsman (1984) and Fenton (1985) provide formulations for the dispersion relation, water elevation and velocity potential for the second, third, fourth and fifth order deep water Stokes theories.

The following tables contain solutions terms of higher order Stokes theories for the water elevation and wave velocity.

Table 2-1: Coefficients for the normalized water elevation $\eta k = \sum_n A_n \xi^n \cos(n(kx - \omega t))$ for different order Stokes deep-water wave theories.

Order	1	2	3	4	5
Reference	Wiegel (1964)	Wiegel (1964)	Kinsman (1984)	Kinsman (1984)	Fenton (1985)
A_1	1	1	$1-\frac{3}{8}\xi^2$	$1-\frac{3}{8}\xi^2$	$1-\frac{3}{8}\xi^2-\frac{422}{384}\xi^4$
A_2	-	$\frac{1}{2}$	$\frac{1}{2}$	$\frac{1}{2}+\frac{1}{3}\xi^2$	$\frac{1}{2}+\frac{1}{3}\xi^2$
A_3	-	-	$\frac{3}{8}$	$\frac{3}{8}$	$\frac{3}{8}+\frac{297}{384}\xi^2$
A_4	-	-	-	$\frac{1}{3}$	$\frac{1}{3}$
A_5	-	-	-	-	$\frac{125}{384}$

**Coefficients expressed in terms of ξ=kH/2 (H= wave height) instead of ak as by Fenton (1985). To second order ξ =ak. Coefficients for third and fourth order theory from Kinsman (1984) were adapted using his own methodology.*

Table 2-2: Coefficients for the normalized horizontal velocity $u/\sqrt{g/k} = \sum_n B_n \xi^n \cos(n(kx - \omega t))e^{nkz}$, for different order Stokes deep-water wave theories.

Order (n)	1	2	3	4	5
Reference	Wiegel (1964)	Wiegel (1964)	Kinsman (1984)	Kinsman (1984)	Fenton (1985)
B_1	1	1	$1-\xi^2$	$1+\frac{1}{4}\xi^2$	$1-\frac{1}{2}\xi^2-\frac{37}{24}\xi^4$
B_2	-	-	-	ξ^2	ξ^2
B_3	-	-	-	-	$\frac{1}{4}\xi^2$

2.1.3 Other theories

Despite the widespread use of Stokes theories to represent and explain wave behaviour there are other wave theories that have been developed under different assumptions:

1) Gerstner (1802) theory for rotational waves with closed circular particle paths where the small amplitude assumption is not invoked (Kinsman 1984, p.241). This theory predicts the same dispersion relation and velocity profile as those in linear wave theory, yet it also predicts a trochoidal water elevation profile which have sharper crests and flatter troughs that resemble more the shape of real waves.
2) Capillary-gravity waves. At high frequencies waves the effect of the surface tension becomes comparable to gravity, leading to a modified wave theory where the linear dispersion relation becomes:

$$\omega^2 = \frac{\rho - \rho_{air}}{\rho + \rho_{air}} gk + \frac{\theta \cdot k^3}{\rho + \rho_{air}} \tag{2-6}$$

Where ρ is the density of the water, ρ_{air} is the density of the air and θ is the air-water surface tension (Lamb 1932, p.459).

3) Longuet-Higgins (1953) developed a wave theory to explain the existence of bottom forward jets in wave tank experiments by relaxing the irrotational assumption and including viscous boundary layers adjacent to the water surface and the bed. The theory predicts an increase in the Stokes drift gradient to double its original value near the surface. This increase induces a second order vorticity diffusing from the surface on a time scale $O(z^2/\nu)$, where ν is the fluid's kinematic viscosity. Note that the existence of this second order vorticity does not imply turbulent flow. His findings were verified by laboratory experiments (Longuet-Higgins 1960).

2.1.4 Growth and decay

Predicting the growth and decay of wind waves is an ongoing challenge in the air-sea interaction discipline. Complex processes occur in the formation of waves where

wind and white-capping induced turbulence plays a fundamental role. Empirical formulae used in the state of the art wave propagation models and in engineering design formulations relate wind speed, duration and fetch with wave heights and periods (Tolman 2009, p.17, CEM2008, II-2-2).

In this investigation, focus will be on the attenuation of homogeneous steady two dimensional wave trains where wave decay and growth is conventionally assumed to be exponential:

$$E = E_0 e^{-\Delta x} \tag{2-7}$$

where E_0 is the initial wave energy density and Δ is the wave attenuation coefficient (Peirson *et al.* 2003, Mitsuyasu and Honda 1982).

Viscous attenuation of infinitesimal waves can be modelled as:

$$EF_V = -2\mu a^2 k\omega^2 \tag{2-8}$$

Where EF_V is the energy flux dissipated by viscosity per unit area and μ is the dynamic viscosity of the water (Phillips, 1977, p.52).

2.2 Turbulence characterization and measurement

Turbulence is an extremely complex and not well understood phenomenon in fluids. Its chaotic and unpredictable behaviour in many different applications has led to the development of a significant number of models and parameterizations to represent the turbulent energy intensity and the dissipation across a range of length scales within the fluid. Due to its complexity, turbulence is commonly characterised through scale relations and statistical representations of characteristic times, velocities and lengths. The most widely used turbulence formulas in field and laboratory measurements have been derived for steady flow and isotropic turbulence.

Some of the most important quantities in the study of turbulence are:

1) Turbulent velocity fluctuations *(u',v' w')*.
2) Turbulent kinetic energy per unit of mass, (*TKE=(u'²+v'²+w'²)*/2).
3) Turbulent kinetic energy dissipation rate per unit volume *(ε)*.
4) Turbulence integral length *(l)*.
5) Mean flow Reynolds number (*Re*=Ū*D*/*v*, where *D* is a characteristic length scale of the mean flow and Ū is the characteristic mean velocity).
6) Turbulence Reynolds number *($Re_L=TKE^2/(\varepsilon v)$,* Pope 2000).

2.2.1 Scale relations

A useful scale relation derived for steady flow and isotropic turbulence from the concept of the balance of the turbulence production and dissipation when viscosity is not important (i.e. at high *Re*) is:

$$\varepsilon = A\frac{u'^3}{l} \tag{2-9}$$

where *A* is a constant of O(1), (Tennekes and Lumley 1972, p.20).

Kolmogorov length and time microscales define the smallest turbulence scales at which the flow is dominated by viscosity.

$$\eta_k = \left(\frac{\nu^3}{\varepsilon}\right)^{1/4} \tag{2-10}$$

$$\tau_k = \left(\frac{\nu}{\varepsilon}\right)^{1/2} \tag{2-11}$$

The Taylor microscale defines the largest length scale at which viscosity influences significantly the dynamics of turbulent eddies.

$$\lambda_T = \sqrt{\frac{15\cdot\nu\cdot u'^2}{\varepsilon}} \tag{2-12}$$

$$Re_{\lambda} = \frac{u' \lambda_T}{\nu} \tag{2-13}$$

where λ_T is the Taylor microscale and Re_{λ} is the Taylor-microscale Reynolds number.

2.2.2 Kolmogorov spectra and the energy cascade

The concept of the energy cascade can be summarized in the often cited verse:

" Big whirls have little whirls
which feed on their velocity;
and little whirls have lesser whirls,
and so on to viscosity
in the molecular sense".

Richardson L. F.(1922)

This concept is the basis for another way of estimating the dissipation rate. Kolmogorov (1941) derived, using a statistical and scaling approach, a universal subinertial range wave number spectrum for high Reynolds numbers and isotropic turbulence.

$$\Phi_k = A\varepsilon^{2/3} k_T^{-5/3} \tag{2-14}$$

where Φ_k is the wave number spectra of the velocity fluctuations, A is a constant O(1) and k_T is characteristic eddy wave number. One of the inconveniences of this technique is that it requires the measurement of the velocity fluctuations simultaneously in many points in space. However a frequency spectrum obtained from a single point measurement can be converted to a wave number using the Taylor frozen turbulence hypothesis in the presence of steady advective flow and using the conversion $t=x/\bar{U}$, where $\bar{U}$ is the mean flow velocity in the x direction (Tennekes and Lumley 1972, p.253). When the frozen turbulence hypothesis is invoked, the measured turbulence spectrum usually corresponds to one of the 3 velocity components. This changes the

value of A in equation (2-14) to A=0.5 for the spectrum measured in the direction of the mean flow and to A=0.65 for the spectra in the other 2 directions.

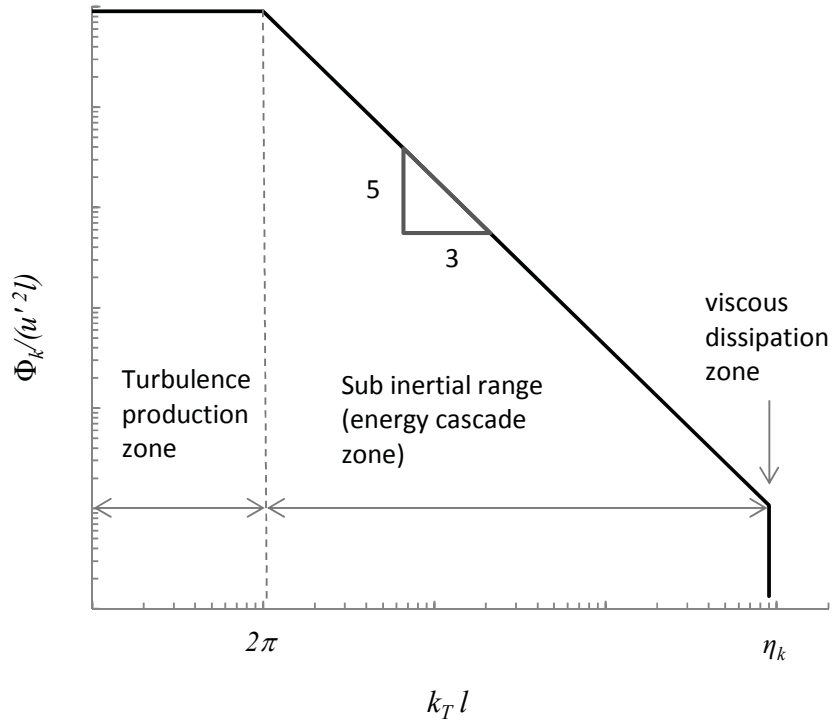

Figure 2-1. Schematic wave number turbulence spectrum.

2.2.3 Wall boundary layer

Many turbulence applications relate to the development of turbulence induced by a solid boundary where turbulence induces a logarithmic mean velocity profile adjacent to the boundary by defining a friction velocity (u_*) and the von Karman parameter (κ=0.41).

$$\mathrm{U}(z) = \frac{u_*}{\kappa} ln(\frac{z u_*}{\nu}) + A \tag{2-15}$$

where A is a constant (Tennekes and Lumley 1972, p.54).

When the non-slip condition is applied, the shear stress at the boundary is related to the friction velocity according to:

$$\tau = \rho \cdot u_*^{\,2} \tag{2-16}$$

Air-sea interaction applications use these concepts to obtain a friction velocity and relate it to the transfer of momentum from the wind to the ocean surface.

2.2.4 Turbulence measurement, waves and noise

The measurement of velocity fluctuations in wavy environments using conventional instruments is complex, requires wave-turbulence decomposition (Cheung and Street 1988, Magnaudet and Thais 1995) and is subject to the noise of the instrumentation (Voulgaris and Trowbridge 1998, Chang and Liu 2000). It is therefore essential to carefully process the velocity measurements and extract the wave and noise contributions in order to obtain reliable estimates of the turbulence parameters. In a velocity time series the turbulent velocity fluctuations are represented by the root mean squared value (standard deviation of the signal) from which the effect of the noise and fluctuations not associated with turbulence needs to be assessed and removed if significant.

In addition to the complexity of the problem, the highest intensities of both the wave and turbulent motions are immediately adjacent to the moving interface and predominantly above the trough levels of the waves, a region that is very difficult to probe with fixed point measurements (Peirson 1997, Hristov et al. 2003).

In slow flows, the noise inherent in acoustic Doppler velocity instruments can induce significant bias in the turbulence statistics extracted from the velocity measurements. Acoustic noise can also be a function of the flow itself (Voulgaris and Trowbridge 1998). However, in this case, spectral techniques such as those explained by Nikora and Goring (1998) can substantially improve the results by removing the identifiable effects of the noise.

Particle imaging velocimetry (PIV) measurements are also subject to noise. In this case the particle density, size, pixel size and window interrogation size play a significant role in defining the ability of the system to measure turbulence (Adrian 1990, Chang and Liu 2000).

2.3 Wave-turbulence interaction theories

Only few wave-turbulence interaction theories have been developed despite the previously discussed significance of this process for engineering applications. Estimates of wave attenuation due to turbulence validated with limited field and experimental data have been carried out by Ardhuin and Jenkins (2006) and have recently been incorporated in wave models, e.g. WAVEWATCH III (Tolman 2009).

Reynolds stresses and turbulence profiles under wind sheared wavy flows have been measured by Cheung and Street (1988) and Magnaudet and Thais (1995) using elaborate velocity decomposition techniques to separate the wave non-turbulent velocity contributions from the turbulent fluctuations. The theoretical analysis of the interaction of Reynolds stresses with the wave field attempted by these authors has not been further developed and the mechanisms of the energy transfer from the wind to the waves, subsurface turbulence, and mean currents remain unresolved.

In spite of all the complexities in the wave-turbulence interaction processes, more simplistic approaches taken by Teixeira and Belcher (2002) and Boyev (1971) have yielded with theoretical estimates for the attenuation of waves due to turbulence.

2.3.1 Teixeira and Belcher (2002)

Teixeira and Belcher (2002) developed a rapid distortion theory to study the interaction of a single irrotational monochromatic wave and weak turbulence. The

model is applicable when the orbital velocity is larger than the turbulence and the slope of the wave is sufficiently high that the straining of the turbulence by waves dominates over the straining of the turbulence itself. The model provides a direct estimate of the wave attenuation coefficient which, for deep water finite amplitude waves, is an increasing function of the square of the velocity fluctuations and the fourth power of the wave frequency:

$$\Delta = 4\frac{\alpha \cdot u'^2\, \omega^4}{g^3} \tag{2-17}$$

where $\alpha = 0.6$ is a constant.

2.3.2 Boyev (1971)

Boyev (1971) proposed a model for the attenuation of low amplitude deep water surface waves by intense turbulence. The model assumes that the energy contained in the turbulence is much greater than the energy contained by the waves and that the mechanism responsible for the wave attenuation is the interaction between vertical mixing caused by the turbulent motion and the non-uniformity of the wave flux over the depth. Boyev (1971) found that the attenuation coefficient is an increasing function of the spatial spectrum of the velocity fluctuations and the wave frequency:

$$\Delta = ku' \int_0^\infty \hat{\Phi}_s^{1/2} s^{-1/2} (1 - e^{-2\pi \cdot k/s})ds \tag{2-18}$$

where $\hat{\Phi}_s = \Phi_s / u'^2 =$ wave number spectra normalized by the velocity fluctuation and s represents the turbulence wave number in the integration variable.

3 GENERAL EXPERIMENTAL FACILITIES

3.1 Wave tank

All experiments were carried out at the UNSW Water Research Laboratory, in the glass sidewall wave tank of 30*m* length, 0.6*m* width and 0.6*m* total depth. At one end a programmable servo-controlled actuator drives a flexible plate wave generator cantilevered from near the tank floor specially designed to efficiently produce deep water waves. At the other end a gently-sloping beach is used to dissipate the wave energy. An automatic control system maintains the tank water depth within ±1*mm*.

Any slicks on the surface of the tank were visually monitored and, prior to testing each day, removed by generating steep waves for approximately 1 hour which carried any surface material to the downstream end of the tank by the Stokes drift. A fan set near the beach was used to ensure that surface slick material was swept onto and retained on the beach.

3.2 Artificial rainfall simulator

A rainfall simulator based on the design of Shelton *et al.* (1985) was used to generate artificial rain over the wave tank. The simulator was shown to produce near-uniform droplet fields with size distributions similar to natural rainfall at terminal vertical velocities across a range of rain intensities from 85 to 168mmh^{-1}. Eight 30WSQ nozzles were installed at 3*m* above the tank surface located with a spacing of 2.13*m* along the tank. Separate water and air manifold systems supplied pressurised air and water immediately upstream of the nozzles. Compressed air is used to increase the exit velocity of the water droplets to yield rain drops at terminal velocity 2.5*m* below the

nozzles. Water from the tank was recirculated through the rainfall system. The mean rainfall rate was controlled by a rotameter.

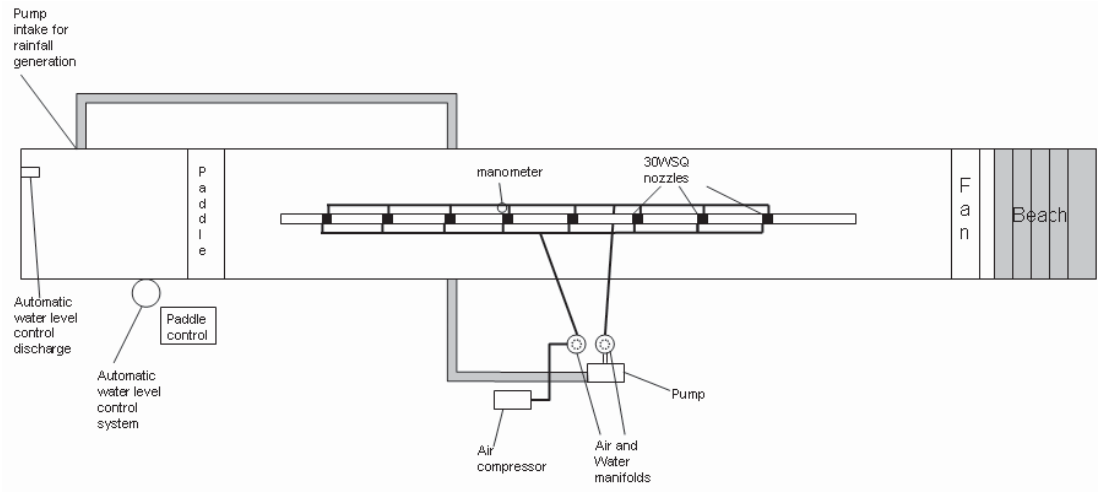

Figure 3-1. Plan layout of rainfall generator and wave tank.

Table 3-1. Nozzle pressure v/s rainfall intensity in rainfall simulator without added air (a) and with added air (b), (from Shelton *et al.* 1985).

a)

Nozzle pressure, kPa	Uniformity coefficient, Cu (%) and intensity, I (mm/h) by nozzle spacing (m)					
	1.98		2.13		2.29	
	Cu	I	Cu	I	Cu	I
21	72	93	73	85	63	79
28	69	79	61	73	73	65
28	81	107	73	100	73	84
31	76	97	68	89	66	79
47	72	122	73	117	76	105
55	61	87	66	87	76	84

b)

Test no.	Nozzle pressure, kPa	Rainfall intensity, mm/h	Uniformity coefficient, %
1	3	89	38
2	7	92	70
3	17	114	85
4	24	142	90
5	31	156	94
6	41	168	94

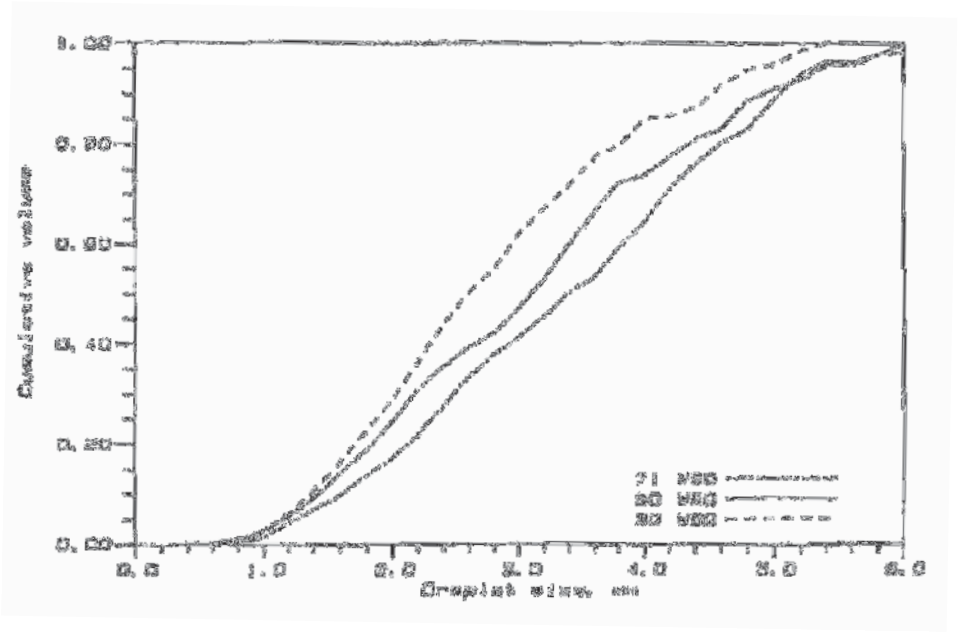

Figure 3-2. Rain drops cumulative distribution produced by the rainfall simulator (Shelton *et al.* 1985).

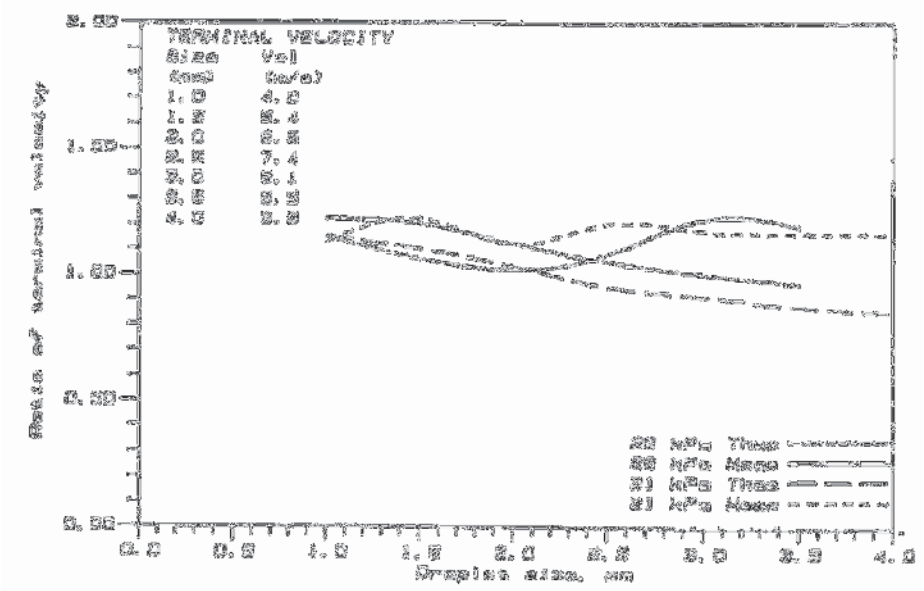

Figure 3-3. Ratio of measured drop impact velocity produced by the rainfall simulator v/s theoretical terminal velocity (Shelton *et al.* 1985).

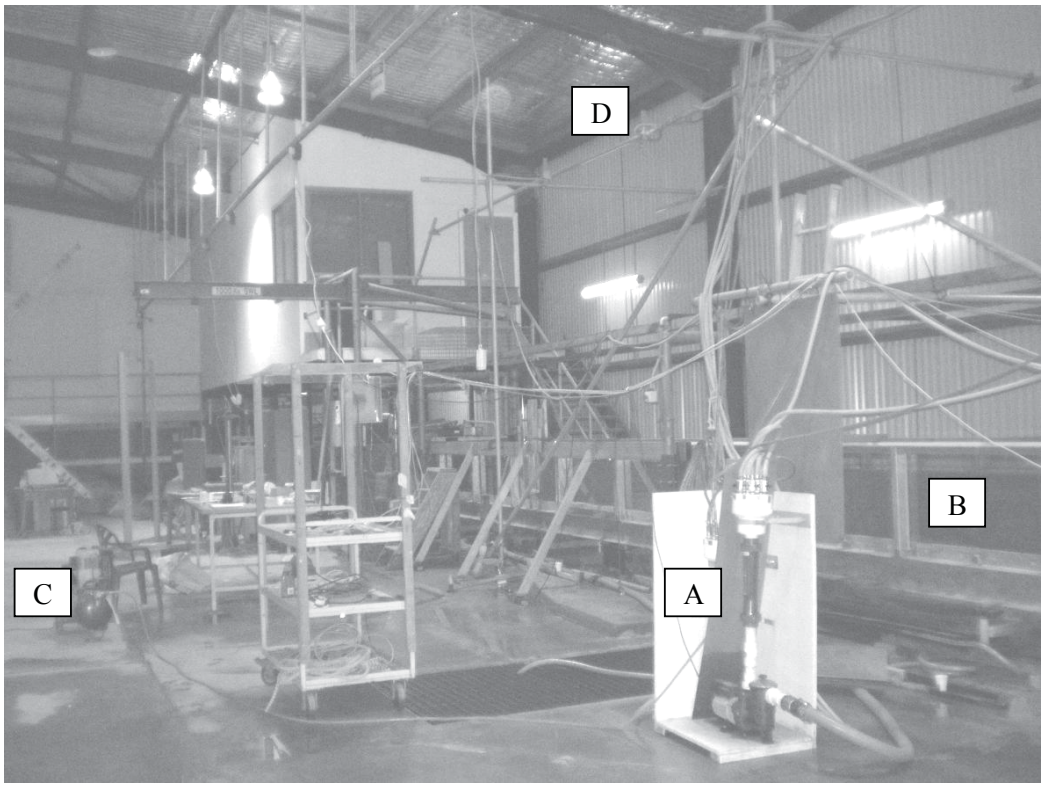

Figure 3-4. Photo of the rainfall simulator and facilities. A) Pump and manifold system, B) wave tank, C) air compressor, D) Nozzles

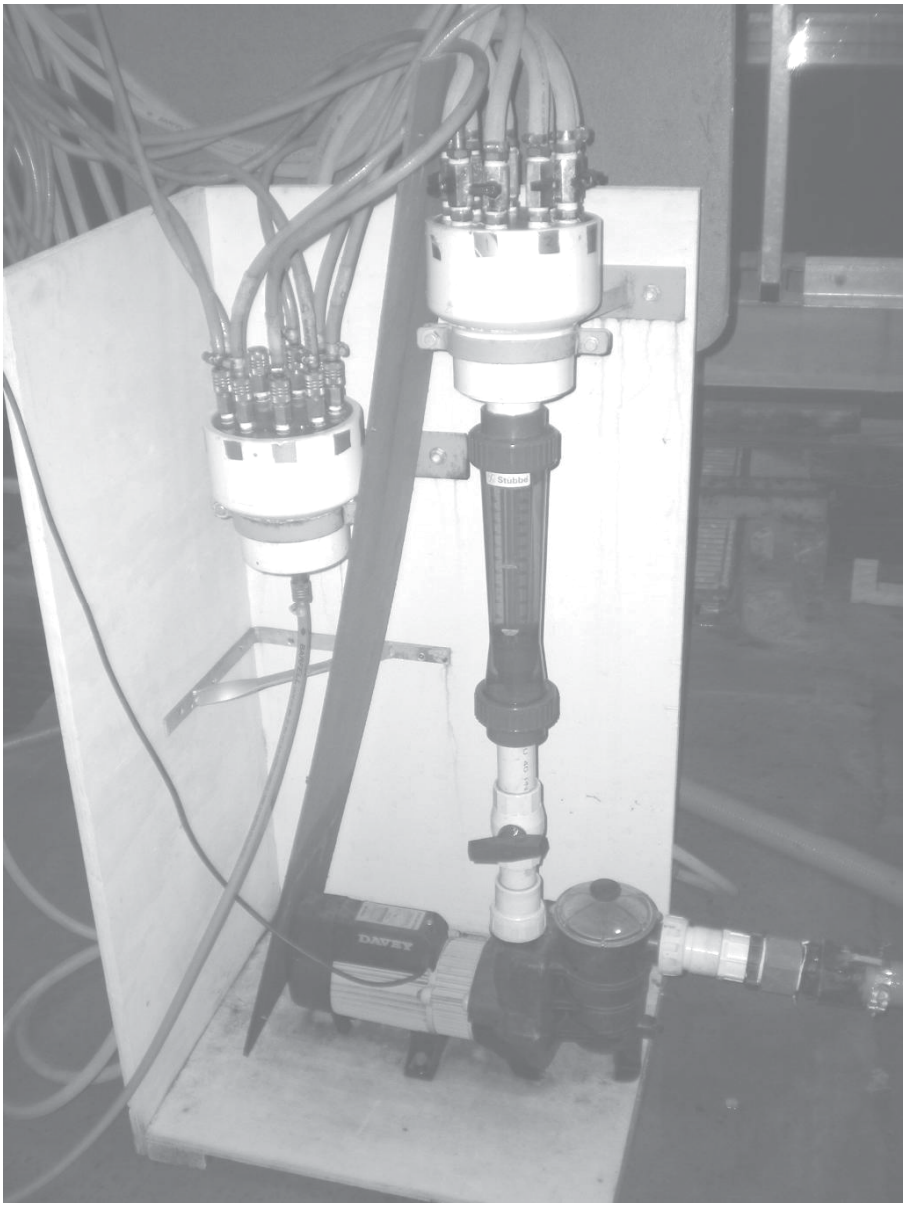

Figure 3-5. Photo of pump, rotameter and manifold system. This allows distribution of water and air evenly to each nozzle.

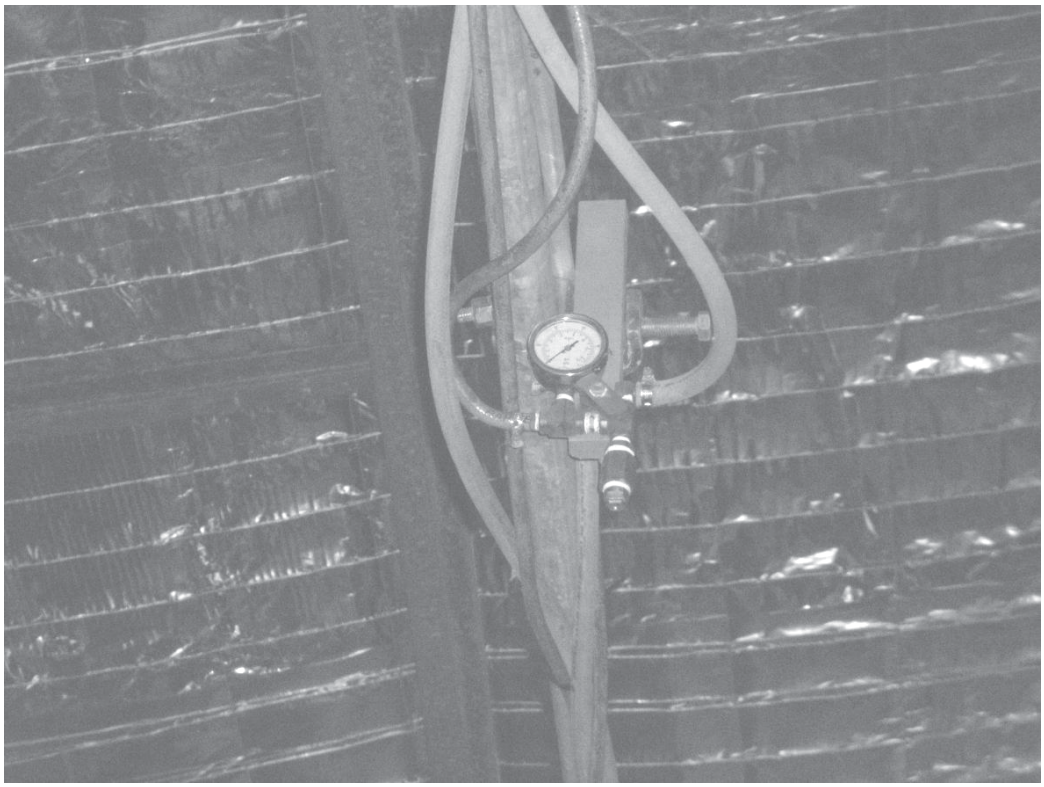

Figure 3-6. Photo of nozzle and manometer.

3.3 Surface elevation measurements

MHL-Mk-V capacitance probes were placed along the tank at the measurement locations. Each probe was calibrated at least twice before and after measurements and showed gain stability better than ±2%. Wave development along the tank was monitored by capturing data at a 600*Hz* sample rate per channel using a National Instruments PCI-6225 data acquisition card fitted to a conventional personal computer. The capacitance wave probe noise levels at the sampling rate for static conditions had a standard deviation less than 0.05*mm*. The raw data were averaged using 15 point bins to obtain a net sampling rate of 40*Hz* prior to spectral processing.

3.4 Acoustic Doppler velocity measurements

A Sontek A827 side-looking 16*MHz*, 5*cm* focal distance, three-dimensional micro acoustic Doppler velocimeter (ADV) was used to measure the velocity field near the water surface. The ADV was mounted on a static structure with a system that allowed the head to move vertically but with the ADV measurement volume projecting away from its body and any supporting appurtenances.

The water column was seeded with 10-30μm diameter white pliolite and rendering clay which was then mixed over the entire depth at least 5 minutes before the start of data recording. The seeding was required to maintain an acoustic signal to noise ratio greater than 15 during the measurement period and the time delay before recording was to allow turbulence generated by the stirring to be dissipated. Testing showed that 5 minutes was an adequate delay to ensure that the measurements were not contaminated by the initial seeding process. Longer times were avoided to prevent low signal to noise ratios near the surface induced by the settling of the seeding material. An ADV beam check was also carried out before each measurement.

An important characteristic of this ADV is that its most sensitive component (i.e. least noisy) is measured in the direction perpendicular to the head while the head parallel components have a higher background level of Doppler noise.

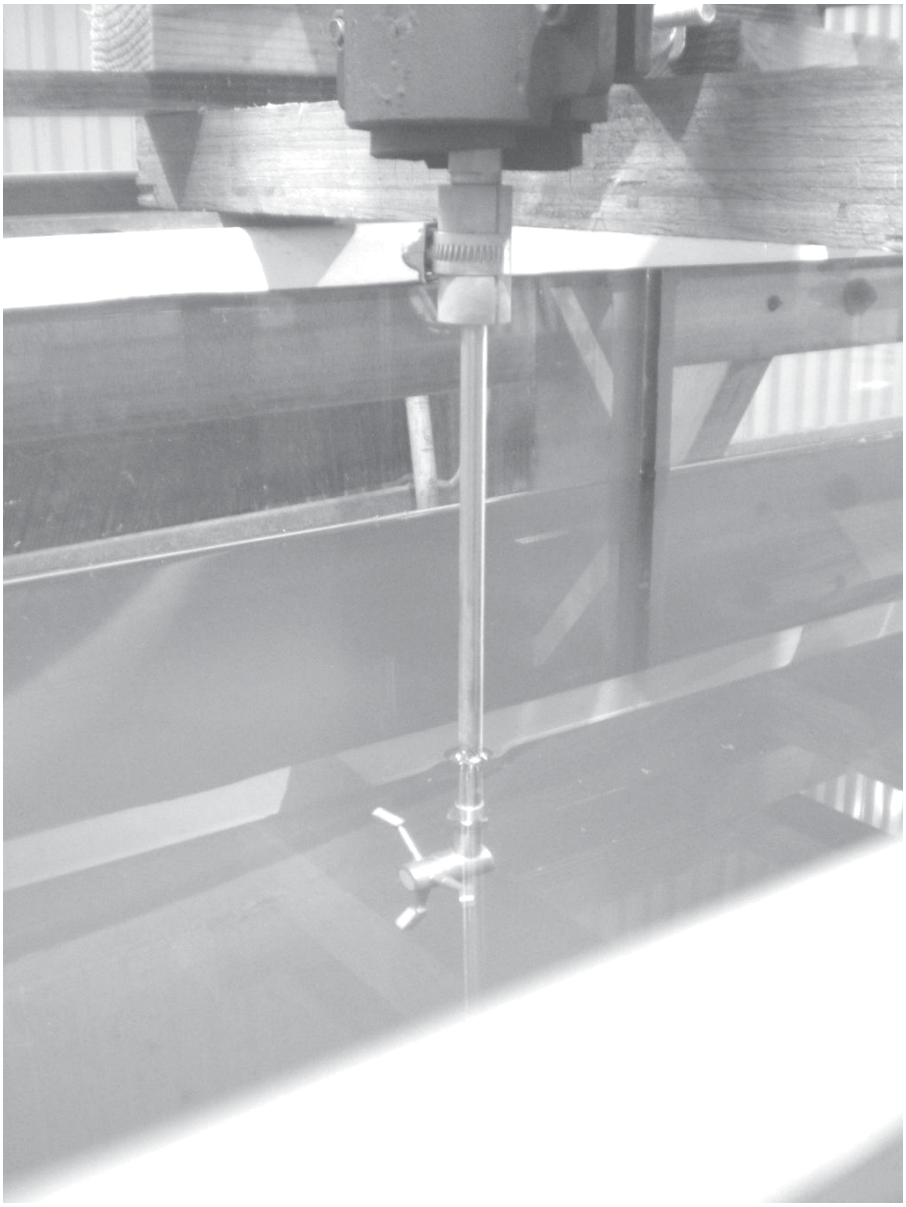

Figure 3-7. Photo of ADV head in the wave tank.

3.5 Dye visualizations

Permanganate crystals and food colorant was used to generate dots, lines and dye patches to visualise turbulent mixing in the flow. A detailed description of the dye visualization techniques for the non-turbulent flow measurements under waves is given in Chapter 5.

4 WAVE ATTENUATION DUE TO RAINFALL-GENERATED SURFACE TURBULENCE

4.1 Background

4.1.1 Wave-turbulence interaction

Very few theoretical assessments of wave attenuation due to turbulence have been undertaken beyond those described in section 2.3. Teixeira and Belcher (2002) predicted theoretically that wave attenuation by turbulence would remove energy from the wave field at a rate approximately 33% of the rate at which energy is fed to the wave field by the wind. Their expressions were calibrated against measurements of wave attenuation in the presence of subsurface generated turbulence.

Peirson *et al.* (2003) measured much higher levels of wave attenuation by opposing wind than would be anticipated from drag considerations, suggesting that wave-turbulence interactions are stronger than the rates estimated by Teixeira and Belcher (2002). Subsequent work by Peirson and Garcia (2008) found that most direct measurements of wind-wave growth already incorporate attenuation due to subsurface turbulence and that the role of turbulence in wind-wave growth remained unresolved.

Another major challenge has been to develop experimental testing conditions for wave-turbulence interactive behaviour that are sufficiently representative of air-sea interaction processes. Olmez and Milgram (1992) used a subsurface stirring grid to provide the wave-dissipating turbulence field. However, turbulence intensity decreases away from the grid, whereas, when the water column is forced by interfacial or near-interfacial shear stresses, turbulent intensity decreases away from the surface as shown in laboratory measurements of pure wind and wind-ruffled waves by Cheung and Street

(1988). A principal difficulty is that the zone of highest wave velocities and turbulent intensities lies above the wave troughs: a region that has proved difficult to obtain reliable direct measurements of the Reynolds stresses (Cheung and Street 1988, Rapp and Melville 1990, Magnaudet and Thais 1995, Siddiqui and Lowen 2006).

Wave breaking is an additional source of turbulence at the surface (Banner and Peregrine 1993) which may generate wave-destructive Reynolds stresses but the significance of this potential process is unknown. Energy fluxes from the wave field due to breaking are presently believed to be dominated by the wave roller doing work on the subsurface current (Duncan 1983).

4.1.2 Rainfall as a surface turbulence generation mechanism

Vertical rainfall was originally selected as the turbulence generating mechanism in these laboratory experiments for the following reasons:

1) Turbulence diffuses from the surface in a similar manner to white-capping and wind shear generated turbulence in the ocean (Craig and Banner 1994).

2) No net horizontal momentum is imparted to the propagating waves.

3) It is steady and homogeneous across the surface which simplifies the analysis when compared with turbulence generated by wind and breaking waves where turbulence cannot be easily separated from propagating waves and where bursting events are present inducing a non-stationary process (Cheung and Street 1988, Magnaudet and Thais 1995, Rapp and Melville 1990).

4) Past studies have assumed a direct relationship between the rainfall kinetic energy flux (KEF_{rain}) and the turbulence dissipation implying the KEF_{rain} had a direct influence in wave attenuation (Tsimplis 1992, Poon *et al.* 1992, Le Méhauté and Khangaonkar 1990).

4.1.3 Rain and wave attenuation

The role of rain in calming the sea is well known amongst mariners and was first studied by Reynolds (1874). Reynolds proposed a mechanism by which rain can attenuate wind waves: raindrops striking the ocean surface generate subsurface vortex rings that penetrate downward mixing a thin layer of subsurface water, and effectively destroying the wave motion in the layer. In more recent times, this process has been the subject of detailed investigations by Manton (1973), Nystuen (1990), Le Méhauté and Khangaonkar (1990), Tsimplis (1992), Poon *et al.* (1992) and Craeye and Schlüssel (1998). All have assumed that the fundamental process responsible for the wave attenuation is an increase in the turbulence intensity adjacent to the surface induced by the raindrops falling on the free surface but these investigators did not quantify the nature of the turbulence and its role in the observed attenuation rates.

Rainfall intensity can be characterised by two primary quantities. The rainfall rate is the volumetric flux rate of water impacting the surface and provides a readily quantifiable and familiar measure of rainfall intensity. However, it can be difficult to get the droplets to achieve terminal velocity at the water surface in the laboratory. Consequently, the rainfall energy flux per unit of surface area (KEF_{rain}) may be a better characterisation of rainfall (Tsimplis 1992).

$$KEF_{rain} = \frac{1}{2}\int_0^\infty \rho \cdot I \cdot f(\phi) \cdot V_{drop}^2(\phi) d\phi \tag{4-1}$$

where I= rainfall intensity, ϕ = rain drop diameter, $f(\phi)$ = rain drop diameter probability distribution, $V_{drop}(\phi)$= raindrop impact velocity as a function of ϕ.

Over the last century extensive investigations of the interactions of rainfall and water waves have been undertaken. Le Méhauté and Khangaonkar (1990) developed a theoretical approach that included the effect of intense rain on waves based on the

momentum exchange from the wind and raindrops impacting the surface at different angles. For vertical rain falling on deep water waves, their model predicted that the attenuation coefficient increases proportionally with the rain intensity and the wave number.

Tsimplis (1992) completed an extensive experimental investigation using a 2.35*m* long, 0.15*m* wide and 0.33*m* deep wave tank exposed to rainfall over a total fetch length of 0.55*m*. Waves of variable steepness in the capillary-gravity range (frequencies between 15.7 and 31.5$rads^{-1}$, his Figure 4) were mechanically generated at one end of the tank using a hinged paddle. The rainfall simulator was an array of vertical hypodermic needles fed by a water-filled box. Mean raindrop sizes were 3.61*mm* and with a fall height of 1.75*m*, drop surface impact velocities were 62% of predicted terminal velocity. High simulated rainfall rates of 300mmh^{-1} and 600mmh^{-1} were used to provide a rain kinetic energy flux similar to natural rain. Individual wave gauges were located immediately adjacent to both ends of the rain section to record the change in wave amplitude. The wave amplitude attenuation coefficient was obtained characterising the local amplitude and assuming an exponential decay with distance (see equation (2-7)).

Tsimplis (1992) found that the wave attenuation coefficient increased systematically with the wave frequency and that it was independent of the wave steepness. Furthermore, his findings showed that wave attenuation was independent of rainfall intensity, in contrast with the theory proposed by Le Méhauté and Khangaonkar (1990). The study concluded that the effect of rainfall can be modelled as constant eddy viscosity of 0.3±0.15cm^2s^{-1}.

A concomitant study by Poon *et al.* (1992) measured the attenuation coefficient for wind-generated waves under rain in an oval recirculating wind-wave tank of 0.31*m*

width, 0.445*m* height, water depth 0.24*m* and 19.7*m* perimeter. A 1*m* long hypodermic needle module was located 0.2*m* above the mean water surface, generating 2.6*mm* mean diameter raindrops at rates of 35, 65 and 100mmh^{-1}. Winds of 3.4, 4.9 and 6.3ms^{-1} were generated in the air cavity to generate surface water waves. Wave frequency spectra were obtained from capacitance probes located up- and down-wind of the rain section. Characteristic rain-induced wave amplitude attenuation rates were obtained by quantifying the changes in spectral energy with the imposition of rainfall.

The attenuation coefficients found by Poon *et al*. (1992) are much higher than those found by Tsimplis (1992). Poon *et al.* (1992) results (however not their written conclusions) corroborate the Tsimplis (1992) finding of no dependence of wave attenuation on rain intensity despite their measurements having been undertaken at much lower rainfall rates (Table 4-1).

4.1.4 Rainfall generated turbulence

Studies of near-surface turbulence and mixing due to rainfall have been undertaken experimentally by Green and Houk (1979), Lange *et al.* (2000), Braun (2003) and Zappa *et al*. (2009). Table 4-1 shows an inter-comparison of the main investigations on rain-wave interaction.

Green and Houk (1979) used a hypodermic needle rainfall simulator mounted at 14m height to study the mixing layers in still water under different temperature and salinity conditions. Generated drop sizes ranged from 1.5 to 5.5*mm* with impact velocities close to terminal velocity for rainfall intensities from 3 to 37mmh^{-1}. They found that a surface mixed layer with a thickness of the order of 200*mm* developed below the free surface after a rainfall period of 15 minutes and that the larger drops play the dominant role in the mixing process. The thicknesses of the surface mixed layers in

salt water were found to be about of a third of those in fresh water under similar drop size and intensity conditions

Braun (2003) completed an investigation of the interaction between radar and rain-irradiated water surfaces and carried out ADV and PIV turbulence measurements in two facilities. ADV measurements were carried out in a wind/rain tunnel 26m long, 1m wide 1.5m total depth. Rainfall was generated over a total tank length of 2.3m using a needle rain generator producing 2.9mm drops falling from 4.5m height. Using a Nortek ADV with a 1cm^3 sample volume and 25Hz sampling rate, Braun (2003) captured water-side turbulence intensities for a single rainfall rate of 40mmh^{-1}. The reported root mean square turbulent velocities were of order 0.02ms^{-1} declining systematically with depth. Braun (2003) also carried out PIV measurements in a different facility using a still tank and a 3.9m height hypodermic needle rainfall simulator able to produce 2.1 and 2.9mm drops at rates of 8 and 216mmh^{-1} respectively.

Lange *et al.* (2000) visualised single droplet impingement processes and found droplet penetration depths of approximately 20mm.

Zappa *et al.* (2009) undertook turbulent dissipation measurements near the water surface irradiated vertically by raindrops of natural sizes falling at close to terminal velocity in an attempt to prove the dependence of the gas transfer rate on rainfall-generated turbulence, an idea introduced in a previous publication by Ho *et al.* (2000). Velocity fluctuation measurements were carried out with a modular acoustic velocity sensor and a coherent Doppler sonar. The dissipation rate was estimated from a Kolmogorov type turbulence spectrum, using the measured mean velocity as the advection velocity required by the Taylor hypothesis (see section 2.2). Dissipation rates near the surface were $O(10^{-3})m^2s^{-3}$ and did not vary significantly for rainfall intensities

between 25 and 50mmh^{-1}. A dissipation rate of $4x10^{-6}m^2s^{-3}$ was measured for zero rainfall at an unspecified depth (Zappa *et al.* (2009), his fig. 9.b).

Table 4-1. Summary of investigations of rain-wave interactions.

Investigators	Facility	Rainfall rates [mmh^{-1}]	Rainfall Energy flux [Wm^{-2}]	Comments relevant to this study
Reynolds (1874)		theoretical		First insights about rain generated turbulence and wave interaction
Manton (1973)		theoretical		Eddy viscosity model for wave attenuation due to rain
Houk and Green (1976)	Still tank hypodermic needle rain simulator (0.64x0.64m area, 14m drop height, 0.5m water depth)	4-35	0.01-0.35	Surface waves generated by rain
Green and Houk (1979)	Still tank hypodermic needle rain simulator (0.62width, 14m drop height, water depth 0.5m)	3-37	0.02-0.44	Mixing layer and surface waves caused by rain
Nystuen (1990)		theoretical		Eddy viscosity model for wave decay due to rain
Le Méhauté and Khangaonkar (1990)		theoretical		Momentum exchange model for wave decay due to wind and rain
Poon *et al.* (1992)	Circular wind-wave tank, hypodermic needle rain simulator (1m fetch, drop 0.2m height, 0.24m water depth)	35-100	0.02-0.05	Wind wave attenuation due to wind and rain
Tsimplis(1992)	Wave tank hypodermic needle rain simulator (0.55m fetch, 1.75m drop height, 0.1m water depth)	300, 600	1.05, 2.10	Wave attenuation due to rain
Bliven *et al.* (1997)	Still tank hypodermic needle rain simulator (4x4m area, 17m drop height, 0.8m water depth)	5-200	0.04-1.69	Surface waves generated by rainfall, radar scatter
Craeye and Schlüssel (1998)		theoretical		Wave attenuation model based on kinetic energy flux and friction velocity
Ho *et al.* (2000)	Still tank hypodermic needle rain simulator (4x4m area, 17m drop height, 0.53m water depth)	14-115	0.09-127	Gas exchange and its relation to turbulence generated by rain
Braun (2003)	Still tank hypodermic needle rain simulator (2.3x1m area, 4.5m drop height, water depth<1.5m, ADV)[1] and (3.9m drop height PIV)[2]	(40)[1], (8, 216)[2]	(0.26)[1], (0.04, 1.31)[2]	Turbulence profile measurements, radar scatter, wind and rain.
Zappa *et al.* (2009)	Still tank nozzle rain simulator (45x19m area, 10m drop height, water depth<6m)	25-50	0.05-1.30	Turbulence profile measurements, Gas exchange and its relation to turbulence generated by rain
This study	Wave tank nozzle rain simulator (17m fetch, 3m drop height, 0.4m water depth)	108,141	0.85,1.11	Turbulence profile measurement, wave attenuation, wave turbulence interaction

4.2 General experimental conditions

Two types of measurements were carried out for all the rainfall scenarios in Table 4-2:

1. Rainfall-induced velocity fluctuations in the wave tank without mechanically generated waves.
2. Rainfall-induced wave attenuation where waves were mechanically generated. Figure 4-1 shows a scheme of the experimental set up for both experiments.

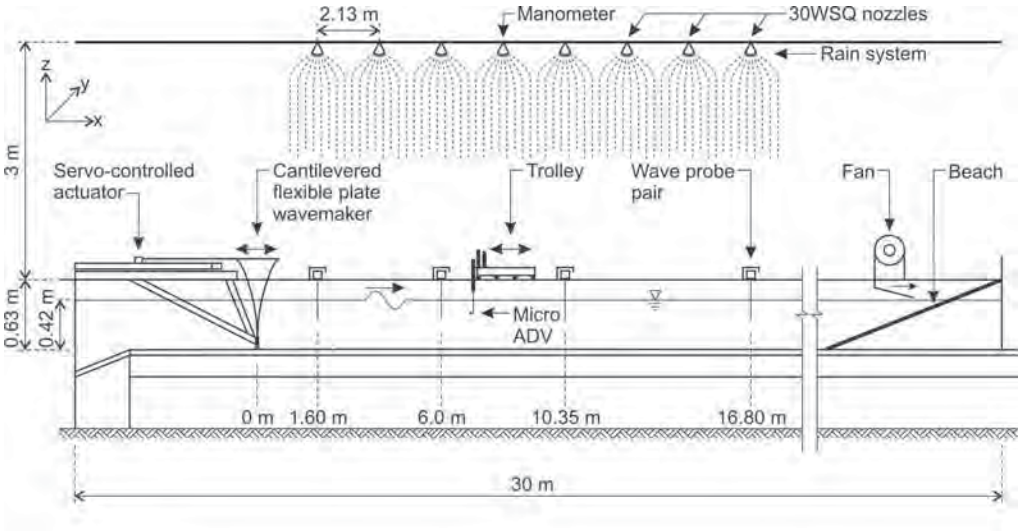

Figure 4-1. Schematic diagram showing the experimental layout and key equipment (not to scale).

For the wave attenuation measurements, only monochromatic waves were generated. The mean water depth was maintained at $0.415m \pm 1mm$ for all experiments by an automatic control system. The two rainfall rates, low rainfall (LR) and high rainfall (HR), were achieved by setting the flow rates and nozzle air pressures in accordance with the corresponding values in Table 2 of Shelton *et al.* (1985) (see section 3.2). Rainfall intensity and uniformity was confirmed during the experiments by

visual inspection and measurements using temporary rain gauges located beneath each nozzle. Wave probes were placed in pairs at 4 fetches along the tank with a 20*cm* width roof top to avoid rain water seeping through the probe boxes and reaching the electronics.

Table 4-2: Rainfall scenarios

code	measured rainfall intensity (mmh^{-1})	pressure at nozzle (kPa)	pump flow rate (lh^{-1})	air	expected rainfall rate from Shelton *et al.* (1985) (mmh^{-1})
NR	0	0	0	off	-
LR	108 ± 7	22	30	off	85
HR	141 ± 6	43	40	on	168

4.3 Measurement of rainfall induced velocity fluctuations

The near-surface rainfall induced vertical velocity fluctuations profile was measured in the absence of any mechanically-generated waves using the ADV described in section 3.4. It was important to ensure that the measurements were taken beneath a sufficiently clear area of surface freely irradiated with rain.

Alternative geometric arrangements with the ADV were possible including submerging the ADV horizontally beneath the surface with its body aligned along the tank. However, subsequent measurement of turbulent dissipation rates required propelling the ADV along the tank at shallow depths. Submerging the ADV had consequent significant wake and wave generation. The selected geometric arrangement was judged to be the least intrusive arrangement and the selection was justified by the subsequent analysis of the captured data.

Preliminary static measurements showed that the turbulent velocities generated by the rainfall were very small. Consequently, for the static measurements, the ADV velocity range was set at its most sensitive level of $\pm 3 cms^{-1}$. Measurement ensembles

consisting of 163.84s of 25Hz velocity samples were used to characterise the turbulence over a depth range between 0.031m and 0.151m. Studies by Voulgaris and Trowbridge (1998) have shown that accurate measurement of turbulence properties can be obtained from ADVs provided that the geometric nature of the instrument and the underlying acoustic noise is properly recognised. The practical outcome of this was that the root mean square noise level was approximately 5 times greater for those velocity components measured parallel to the ADV head (*v'* and *w'* in this present study, Figure 4-1) in comparison to the head-normal component (*u'*). Voulgaris and Trowbridge (1998) show that the ADV reliably measures the *u'* component directly provided that the turbulence levels are not too high.

4.3.1.1 Static ADV measurements

Representative velocity spectra obtained from the static ADV measurements are shown in Figure 4-2. Following Voulgaris and Trowbridge (1998) and Nikora and Goring (1998), the ambient acoustic noise was determined directly from the measured velocity spectra. In Figure 4-2, the instrument acoustic noise level is clearly apparent above 45$rads^{-1}$. The spectra shown in Figure 4-2 also show low frequency (<8$rads^{-1}$) velocity fluctuations induced by seiches and other low frequency motions within the tank itself. The intensities of velocity fluctuations directly induced by the rain were calculated by partitioning the spectra at the minimum spectral level at the lower frequencies and then deducting the acoustic noise from the remaining high frequency spectrum. This process assumes that the instrument noise is uncorrelated with the velocity fluctuations (Bradshaw, 1971).

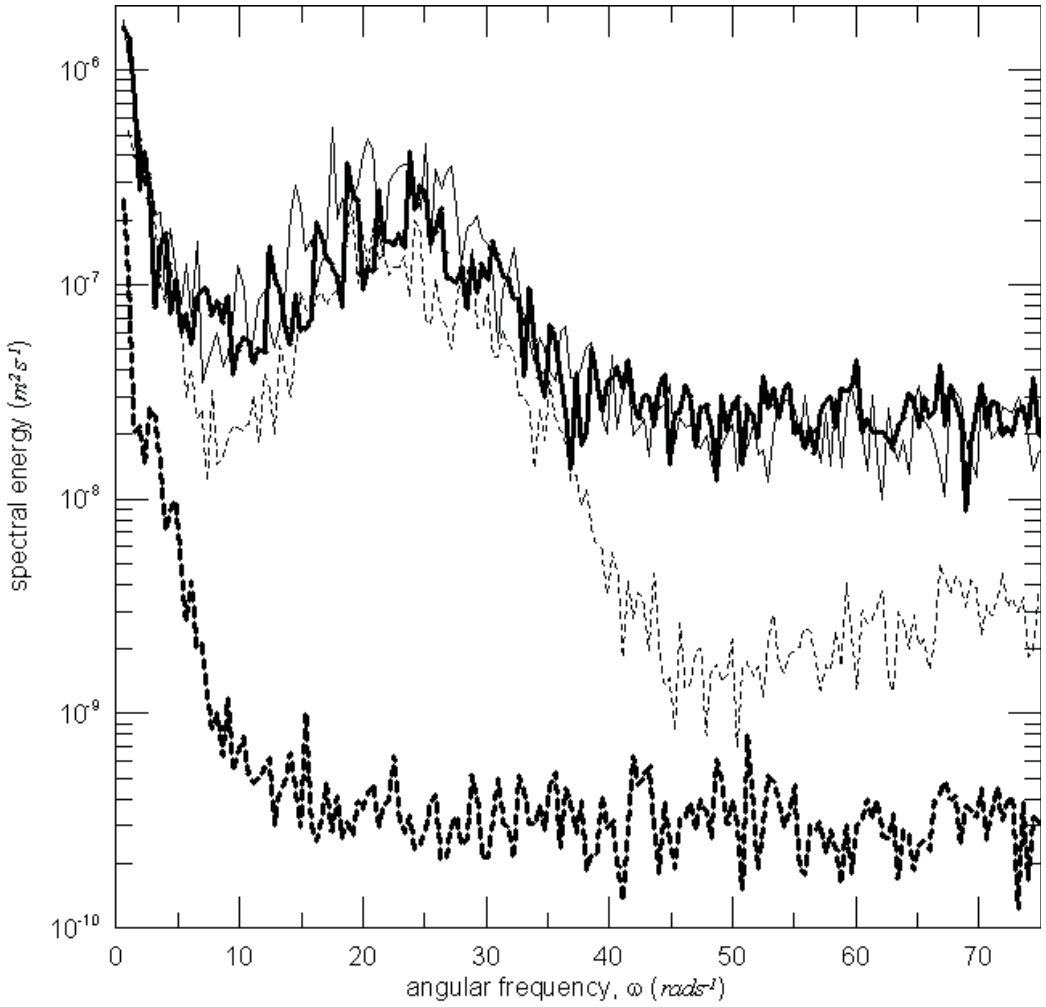

Figure 4-2. Representative fluctuating velocity spectra obtained from the acoustic Doppler velocimeter in static mode. HR *u'* light dashed line, HR *v'* heavy solid line, HR *w'* light solid line, NR *u'* heavy dashed line. Note the clearly defined minimum in spectral energy at approximately 8$rads^{-1}$ and the approximately constant acoustic noise level above 45$rads^{-1}$. Note also the much lower acoustic noise of the head-normal velocity component (*u'*) and the flat (white noise) spectrum obtained under the NR case.

4.3.1.2 Moving ADV measurements

Vertical rainfall generates negligible mean flow, therefore wave number spectrum measurement required profiling with the ADV along the tank at constant speed and invoking Taylor's frozen turbulence hypothesis (see section 2.2). A mean

speed of 8.5cms^{-1} was used with the ADV measurement volume projected forward of the trolley assembly. The noise inherent in the measurements increased for two reasons:

1. The ADV velocity range has to be increased to ±30cms^{-1} thereby also increasing the system acoustic noise.
2. In spite of considerable care in the manufacture and operation of the trolley system, the along-tank jitter in the instrument package motion contaminated the measurements in the *u'* direction.

Within all the velocity components *w'* was selected for computing wave number spectra because it exhibited the lowest noise level and an approximately white spectral response in the absence of rainfall (Figure 4-3).

For each depth, smoothed spectra were obtained by averaging four repeat measurements. The corresponding wave number spectrum in the presence of rainfall (with acoustic noise deducted) yielded an energy peak at the integral turbulence *l* and a form of energy spectrum compatible with determining a dissipation rate (Figure 4-3). On the other hand, the estimated Taylor-scale Reynolds number (see section 2.2.1 and Pope 2000, p. 200) is less than 26, revealing the weakness of the turbulence and suggesting that a significant portion of the kinetic energy may be dissipated directly by viscosity. This indicates that the turbulence spectra is in the lower limit of the validity of Kolmogorov's assumptions making it unsuitable for reliably determining the turbulent dissipation rate (Pope 2000, p. 235).

Nevertheless the turbulent wave number spectra did yield reliable values of the outer turbulence scales (Figure 4-3). The integral lengths in Figure 4-4 were extracted from the measured spectra and were anticipated to conform to a wall-type layer form:

$$l = \kappa\left(z_0 + |z|\right) \qquad \textbf{(4-2)}$$

where z_0 is the roughness length on the water side and z is the vertical coordinate measured positive upwards from the mean water level (Craig and Banner, 1994). The error in l was estimated from the upper and lower peak wave number values of the peak of the spectrum (Figure 4-3). A value of z_0=23±2mm was obtained from the same figure.

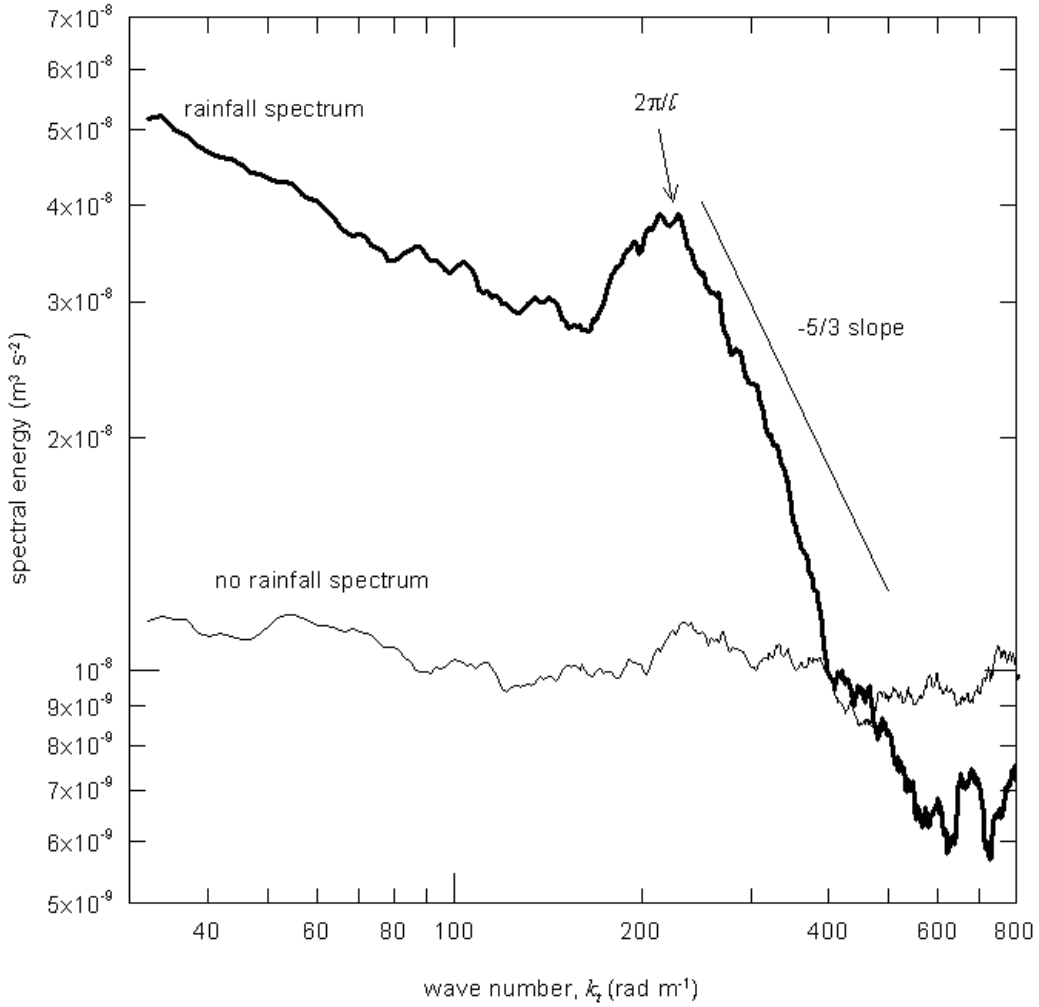

Figure 4-3. Representative wave number spectra obtained from the towing trolley experiments for the *w'* velocity component (ADV mounted at 0.037m depth). Plotted spectra are the mean of 4 independent measurements, smoothed with 11 point bin averages. Light line shows the spectrum obtained in the absence of rainfall and shows little modulation with wave number. Heavy line shows the high rainfall case without acoustic noise deducted. A line with -5/3 slope is shown as a reference. The integral length scale (ℓ) for the high rainfall case is indicated. Note the higher noise levels in comparison with the static measurements shown in Figure 4-2.

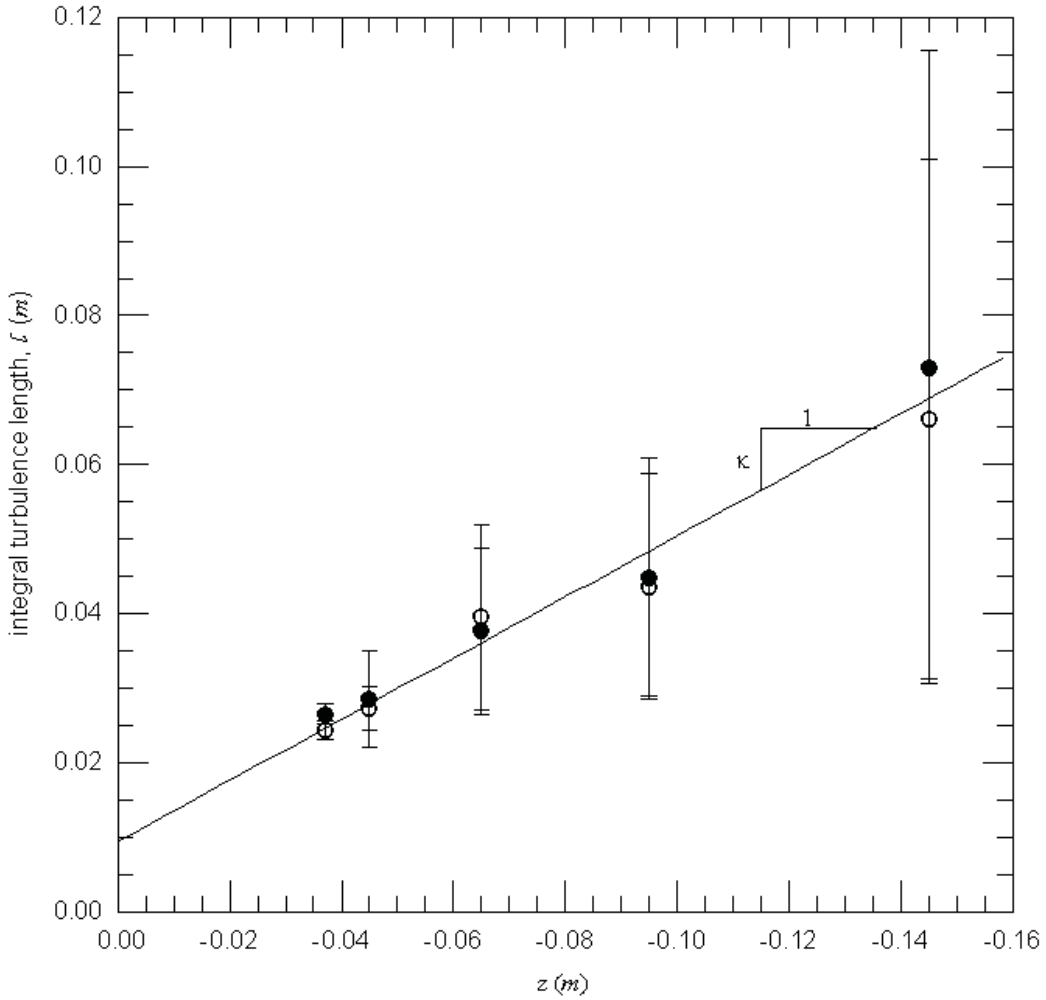

Figure 4-4. Vertical profile of the turbulent integral length scale (*l*) obtained from the intensity spectra. Solid and hollow circles indicate the LR and HR values respectively. The error bars were obtained from the uncertainty in determining the spectral peak (Figure 4-3). The solid line shows a linear fit with a slope equivalent to the von Karman parameter, κ= 0.41. Data fits Craig and Banner (1994) wall type model shown in equation (4-2).

4.4 Measurement of rainfall induced wave attenuation

Wave measurements were undertaken for all rainfall scenarios indicated in Table 4-2. Four pairs of capacitance probes were located along the tank at fetches 1.60*m*, 6.00*m*, 10.35*m* and 16.80*m* from the wave paddle (Figure 4-1). Water elevation time series of 102.4*s* were recorded for all probes all tests and all rainfall scenarios as

explained in section 3.3. Water temperature varied from 10.9 to 12°*C* during the measurement period.

Table 4-3 summarises the tests conditions in the same order of data recording for each rainfall scenario.

Table 4-3: Wave characteristics for attenuation measurement tests

test number	$\omega(rads^{-1})$	$k\ (radm^{-1})$	*ak*	*a (mm)*
2	15.7	25.1	0.05	2.0
3	15.7	25.1	0.10	4.0
4	15.7	25.1	0.15	6.0
5	12.6	16.1	0.05	3.1
6	12.6	16.1	0.10	6.2
7	12.6	16.1	0.15	9.3
8	10.5	11.2	0.05	4.5
9	10.5	11.2	0.10	8.9
10	10.5	11.2	0.15	13.4
11	18.0	33.1	0.10	3.0
12	18.0	33.1	0.15	4.6
14	14.0	19.6	0.05	2.5
15	14.0	19.6	0.10	5.0
16	14.0	19.6	0.15	7.5
17	11.4	13.4	0.05	3.8
18	11.4	13.4	0.10	7.5
19	11.4	13.4	0.15	11.3
20	15.7	25.1	0.05	2.0
21	15.7	25.1	0.10	4.0

Figure 4-5. Photo during rainfall wave attenuation measurements. Note roof protecting the wave probe pair.

The attenuation of monochromatic waves with frequencies between 10.5 and 21.0$rads^{-1}$ and mean steepnesses (ak) from 0.05 to 0.15 was measured during the course of the investigation. The ceiling value of ak=0.15 was determined from preliminary observations of the formation of Benjamin-Feir (1967) instabilities in the absence of rainfall. At steepnesses greater than 0.15, the wave trains were found to degenerate into groups sufficiently steep to initiate breaking within the test section. Breaking would directly remove energy from the wave field and would contaminate the measurement approach taken during this study.

For each test, wave generation commenced at least two minutes prior to data collection. Initial measurements were undertaken with no rain (NR) to obtain the background viscous attenuation within the test facility.

A representative set of spectra obtained for the three rain scenarios are shown in Figure 4-6. Fast Fourier transform techniques were used to compute the energy

characteristic of the monochromatic waves from each water level time series. The high digitisation rate coupled with the large FFT sample size enabled excellent resolution and extraction of the monochromatic wave energy. As shown in Figure 4-6, the spectral energy (S_w) of the monochromatic waves can be clearly distinguished from the energy of waves generated by the rain. In the absence of rain, the non-linear harmonics of the fundamental wave are clearly apparent in these spectra highlighting the low noise characteristics of the wave probes. The energy associated with a monochromatic wave of angular frequency ω_p was extracted from each record by integrating the spectral energy within the angular frequency band $(1\pm0.05)\omega_p$.

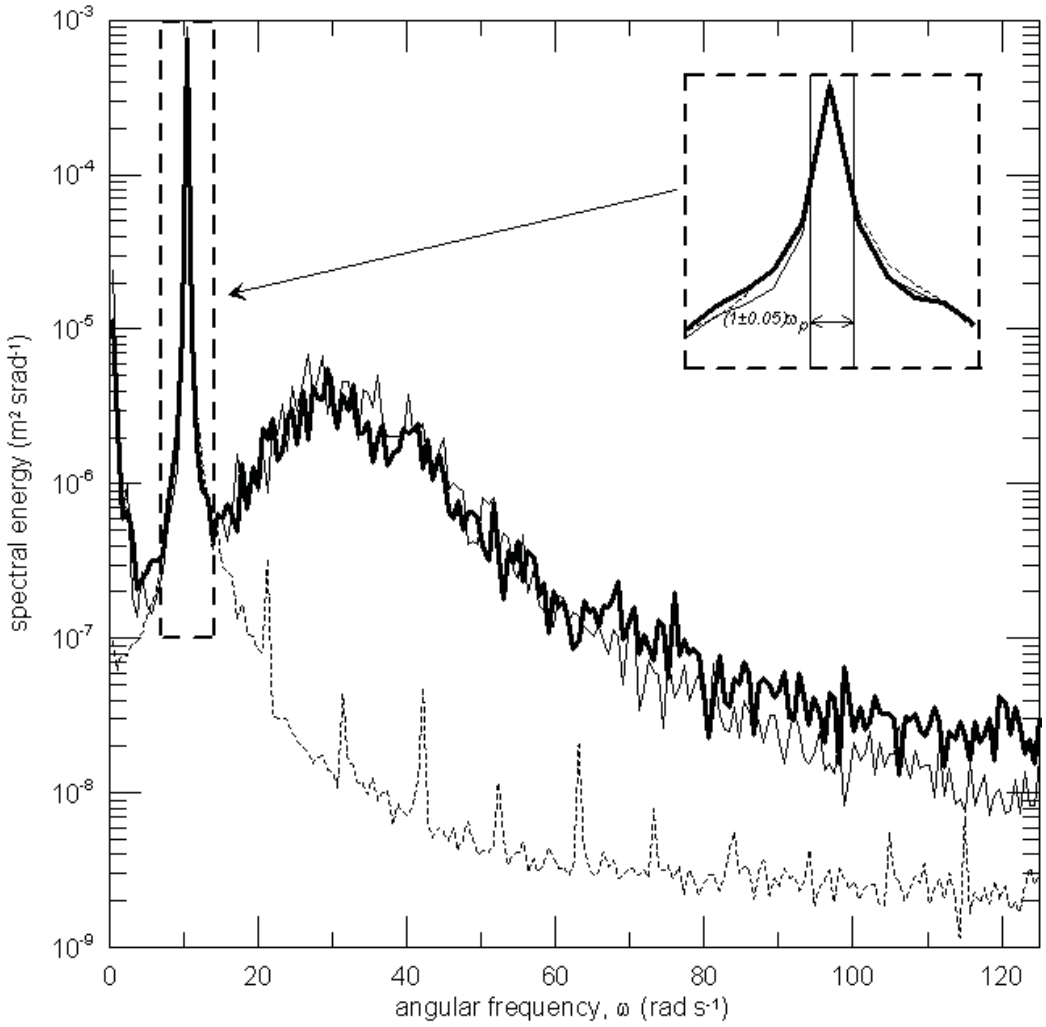

Figure 4-6. A set of representative wave spectra (S_w) for the test case ω=10.46*rads*$^{-1}$, *ak*=0.05 and recorded at a distance of 10.35*m* from the wave generator: NR dashed line; LR solid thin line; HR solid thick line. Note the clearly defined harmonic peaks in the NR spectrum and the negligible difference in the spectral wave energy for the LR and HR cases. The inset region shows the frequency region used to characterise local monochromatic wave energy.

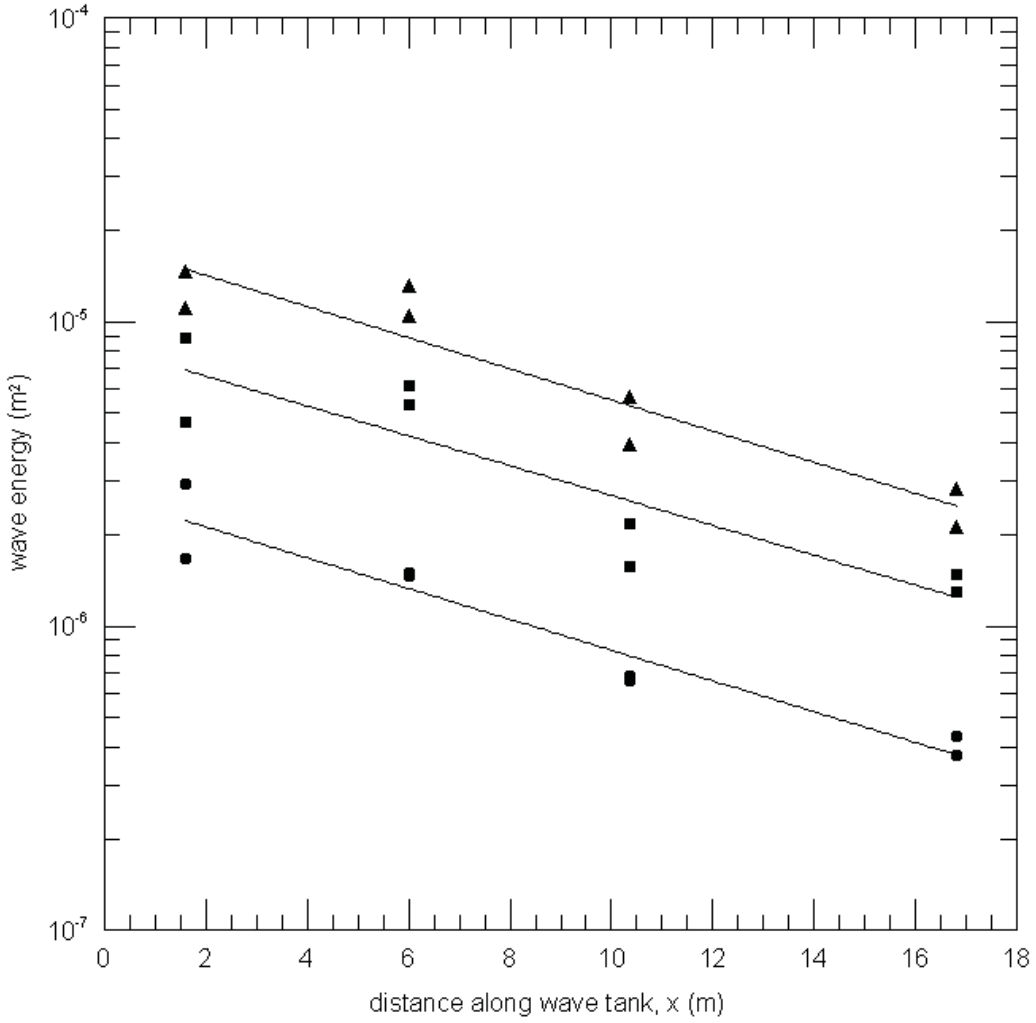

Figure 4-7. Wave energy as a function of distance from the wave maker for the highest rainfall condition with ω =15.7*rads*$^{-1}$: circles *ak*=0.05, squares *ak*=0.10; triangles *ak*=0.15. Lines show the exponential best fits used to determine the attenuation rate. Note the fitted lines are near-parallel, indicating the weak dependency of attenuation on wave steepness.

Total wave attenuation was assumed of the form of equation (2-7) with the total attenuation coefficient corresponding to Δ_T.

Figure 4-7 shows the decline in monochromatic wave energy with fetch for waves of angular frequency 15.7 *rads*$^{-1}$ and varying wave steepnesses under the action of rainfall. For each experiment Δ_T was determined by a least-squares fit of the data. Error bars represent the 90% confidence interval determined according the method described by

Peirson *et al.* (2003), p. 354. It was observed that the correlation coefficient systematically decreased with decreasing wave frequency reflecting the low attenuation rates at the lower frequencies.

4.5 Comparison with other studies

4.5.1 Rainfall induced turbulence

Figure 4-8 shows fluctuating velocity profiles measured with the ADV in static mode contrasted with other studies. Note that measured *v'* and *w'* remain approximately 40% higher than the comparable *u'* as might be anticipated from Figure 4-2. This effect is caused by different noise levels in the ADV components (see section 3.4) and it does not imply anisotropic turbulence. In fact the similitude between the ADV *v'* and *w'* profiles indicates that turbulence is isotropic in the profile given the similar response to noise of those ADV components. The maximum deducted RMS acoustic noise levels were $5.1\times10^{-4} ms^{-1}$ for the *u'* component and $2.1\times10^{-3} ms^{-1}$ for the *v'* and *w'* components.

The most reliable static ADV data are obtained from the velocity component normal to the ADV head, which corresponds to the along-tank axis component (*u'*) whilst Braun (2003) aligned the head normal component vertically upwards (*w'*). Although the velocities recorded in the head-parallel directions are less accurate, the data of Braun (2003) and this present study confirm a significant result: the turbulence measured beneath rainfall is isotropic for all practical measurement depths. Although Braun (2003) does not appear to address the issue of ADV acoustic noise, this appears to be the reason for the rapid divergence of the head-normal and head-parallel velocity components in her results.

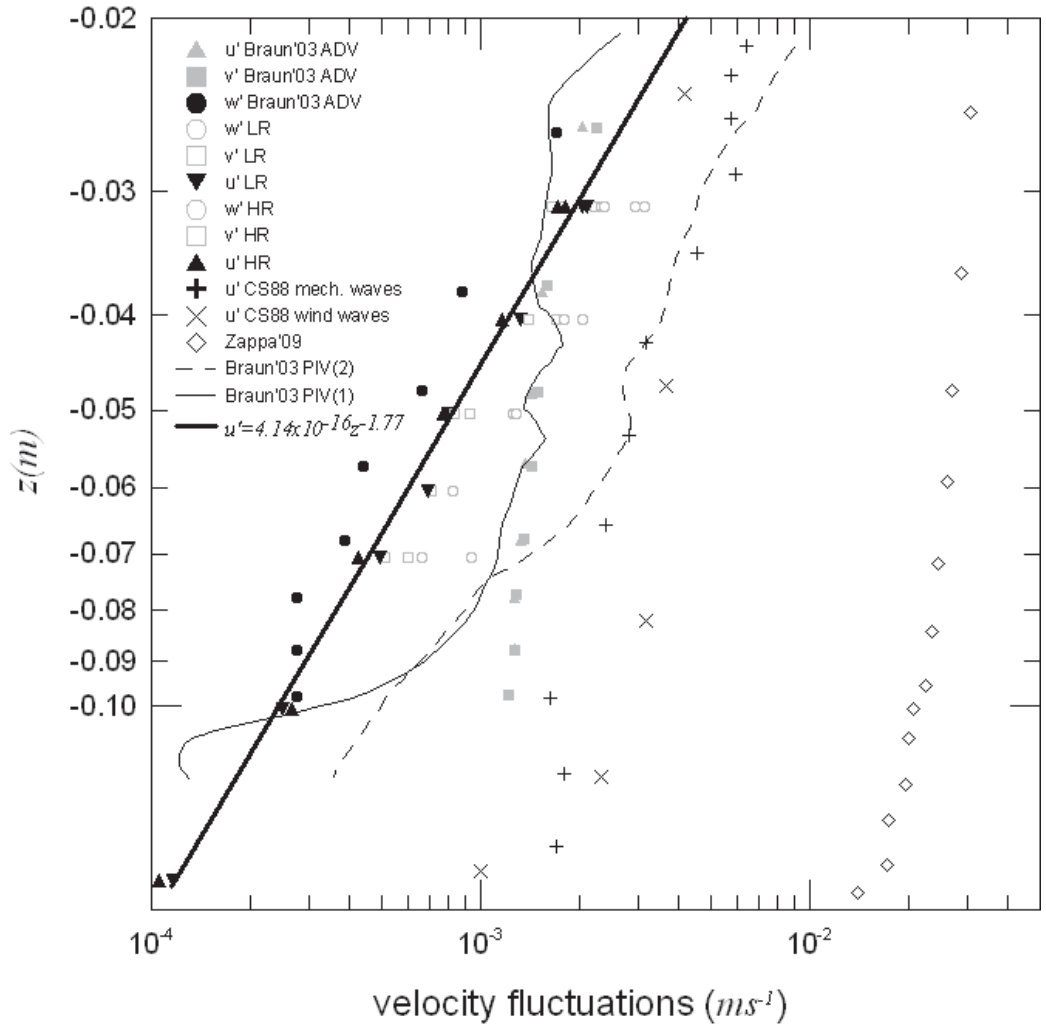

Figure 4-8. Vertical profiles of velocity fluctuations obtained from the static ADV measurements for both rainfall conditions compared with other studies. All ADV velocity components *u'*, *v'* and *w'* are distinguished by triangles, squares and circles respectively. Black solid symbols indicate the ADV head normal component (most reliable). Multiple identical symbols indicate repeat measurements. *u'* LR (Low Rainfall) and HR (High Rainfall) conditions are indicated by black downward and upward pointing triangles respectively while *v'* and *w'* are indicated by hollow symbols. Solid thick line corresponds to a power fit $u'=4.14x10^{-16}z^{-1.77}$ to LR and HR data. *u'*, *v'* and *w'* ADV components data of Braun (2003, 40$mmhr^{-1}$) are indicated by black circles and gray squares and triangles respectively. Braun (2003) PIV measurements are shown as solid-thin (8mmh^{-1}, 2.1mm drop size)(1) and dashed (216mmh^{-1}, 2.9mm drop size)(2) lines. x and + indicate Cheung and Street (1988) *u'* measurements at their lowest wind (1.7ms^{-1}) for Case I wind waves and Case II wind-ruffled mechanical waves respectively. Hollow diamonds are the corresponding *u'* velocities obtained from the turbulent dissipation measurements of Zappa *et al.* (2009) using equations (2-9) and (4-2) and the value of z_0 measured during this study (z_0=23mm).

The consistency of the two sets of results is remarkable given the significantly different tank configurations, rainfall rates, generation methods and consequent rain energy flux. Present measurements showed no systematic change in the turbulent intensity by changing the rainfall rate. Braun (2003) found an almost identical exponential decay in fluctuating velocity intensity with depth at levels approximately 75% of those found in this study. Note that the ADV measurements by Braun (2003) were carried out under a KEF_{rain} of approximately 30% of those in the present study. The apparent insensitivity of the fluctuating velocities to the rainfall intensity is remarkable.

Braun (2003) PIV measurements covered a wider range of KEF_{rain}, from 4% to 120% the values of the present study. Her near-surface velocity fluctuations show an increase with KEF_{rain}. However, the velocity profiles have a similar decaying trend compared to those of the present study and the near-surface values remain below $10mms^{-1}$. The influence of the noise in her PIV turbulence measurements and the potential bias this could cause towards higher values was not indicated (Chang and Liu 2000).

To clarify this issue further, the variation in u' as a function of rainfall rate was examined with the ADV measurement point at a fixed depth of $31mm$. As shown in Figure 4-9, no systematic trend in turbulent intensity can be detected with the rainfall rates that could feasibly be generated with this facility.

Figure 4-9 also shows the u' values intensities computed from the interpolation of the turbulent dissipation profile of Zappa *et al.* (2009) at z=-$31mm$. The estimate of u' was carried out using equation (2-9) with the constant A=1 and the integral length, l, obtained from equation (4-2) using the value z_0=$23mm$ obtained from the present

measurements. The derived fluctuating velocities are approximately an order of magnitude higher than the values observed during this study (Figure 4-8 and Figure 4-9). At present, no obvious explanation has been found for the disparity between these data sets. However, in our experiments we noted the weakness of the rainfall-triggered turbulence and the potential for measurement contamination by acoustic noise, which may have not been fully assessed by Zappa *et al*.

A comparison with Cheung and Street (1988) wind-induced turbulence measurements has also been included in Figure 4-8 showing significantly smaller turbulence levels than those in Zappa *et al.* (2009).

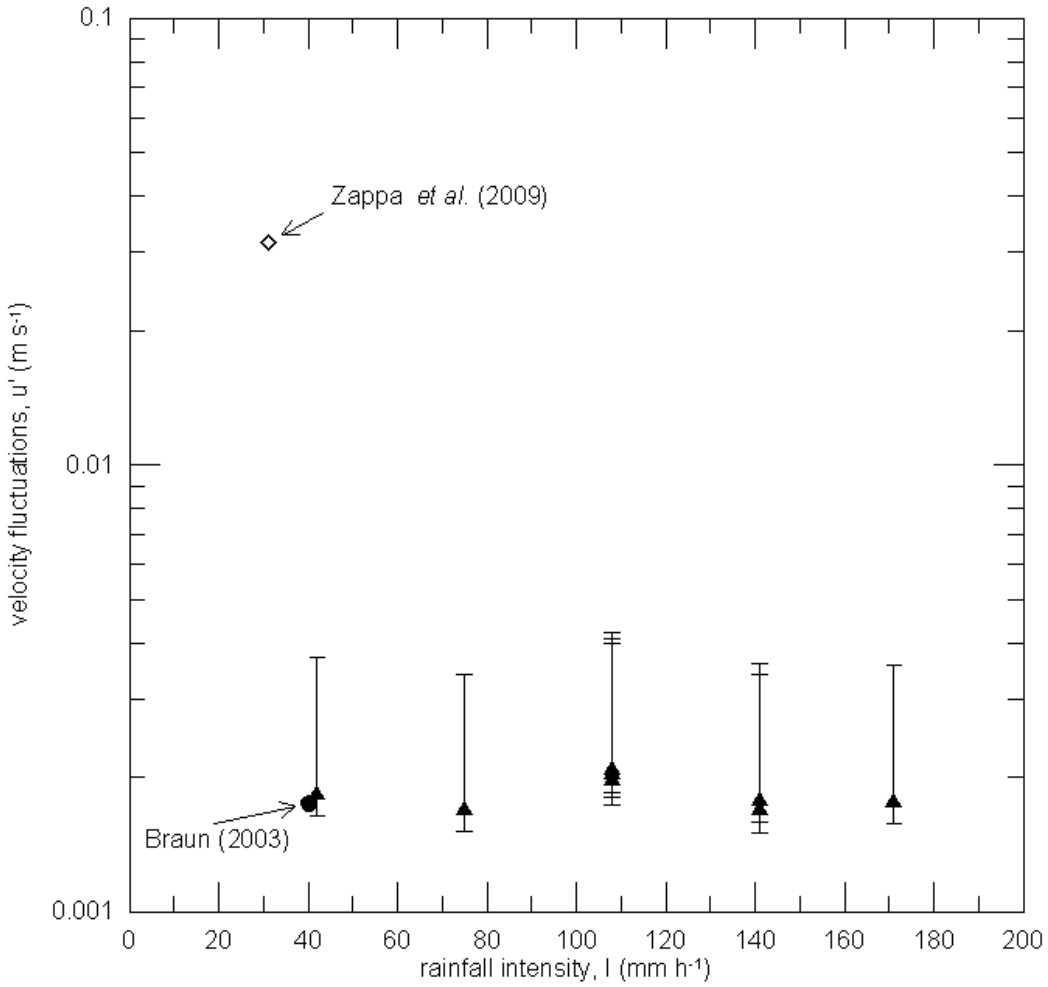

Figure 4-9. Velocity fluctuations recorded at 31*mm* depth showing the relative insensitivity to rainfall intensity. Circles, *u'* present study measurements at *z*=-31*mm*; solid square *w'* Braun (2003, interpolated); diamond, *u'* Zappa *et al.* (2009) estimated as for Figure 4-8. Rainfall rates outside the operating range recommended by Shelton *et al.* (1985) were achieved by adjusting the pump and the air flow rate to produce the desired approximately uniform rainfall rate. Error bars represent the maximum uncertainty. The high limit corresponds to the raw u RMS value without filtering and noise deduction. The low limit corresponds to an estimate of a 10% error in the evaluation of the noise level and frequency band in the *u'* calculation.

4.5.2 Wave attenuation induced by viscosity in the tank

Wave attenuation coefficients measured for the NR scenario show good agreement with van Dorn (1966) viscous attenuation predictions (Figure 4-10). No clear wave steepness dependence is observed that is consistent with the van Dorn (1966)

findings. Measured values of the damping coefficient due to viscosity are within the predictions of van Dorn (1966) showing that the experiments were carried out in a clean tank. Shown also is the van Dorn (1966) expression for an immobile surface.

Van Dorn (1966) verified Hunt (1952) and Lamb (1932) side walls and surface viscous attenuation theoretical expressions in wave tank experiments with small amplitude waves propagating on a clean water surface.

$$\Delta_b = \frac{4k}{b}\left(\frac{\nu}{2\omega}\right)^{1/2}\left[\frac{kb + sinh\,2kd}{2kd + sinh\,2kd}\right] \qquad \textbf{(4-3)}$$

$$\Delta_s^{clean} = \frac{16\nu k^2}{c_g} \qquad \textbf{(4-4)}$$

Note: original expressions have been multiplied by a factor of 2 in order to convert wave amplitude attenuation into wave energy attenuation, assuming E α a^2.

where Δ_b is the viscous wave attenuation coefficient due to solid boundaries, Δ_s^{clean} is the viscous wave attenuation coefficient due to a clean water surface and b is the wave tank width.

Assuming linear superposition of the attenuation effects and using linear wave theory for deep water gravity waves (see section 2.1.1), equations (4-3) and (4-4) yield the total attenuation coefficient due to viscosity (Δ_V) for the conditions of these experiments:

$$\Delta_V = \Delta_s^{clean} + \Delta_b = \frac{32\nu}{g^3}\omega^5 + \frac{2\sqrt{2\nu}}{gb}\omega^{3/2} \qquad \textbf{(4-5)}$$

Van Dorn (1966) showed substantial differences in the attenuation coefficient for different water surface conditions (clean, semi-polluted, fully contaminated), where the wave attenuation coefficient for a fully contaminated (or immobile) surface is:

$$\Delta_s^{imm} = \frac{4k}{b}\left(\frac{\nu}{2\omega}\right)^{1/2}\left[\frac{kb\sinh^2 kh}{2kh + \sinh^2 kh}\right] \qquad \textbf{(4-6)}$$

Note: original expression has been multiplied by a factor of 2 in order to convert wave amplitude attenuation into wave energy attenuation, assuming E α a^2.

which yields equation (4-7) after the linear theory approximations for deep water waves.

$$\Delta_s^{imm} = \frac{2\sqrt{2\nu}}{g^2}\omega^{7/2} \qquad \textbf{(4-7)}$$

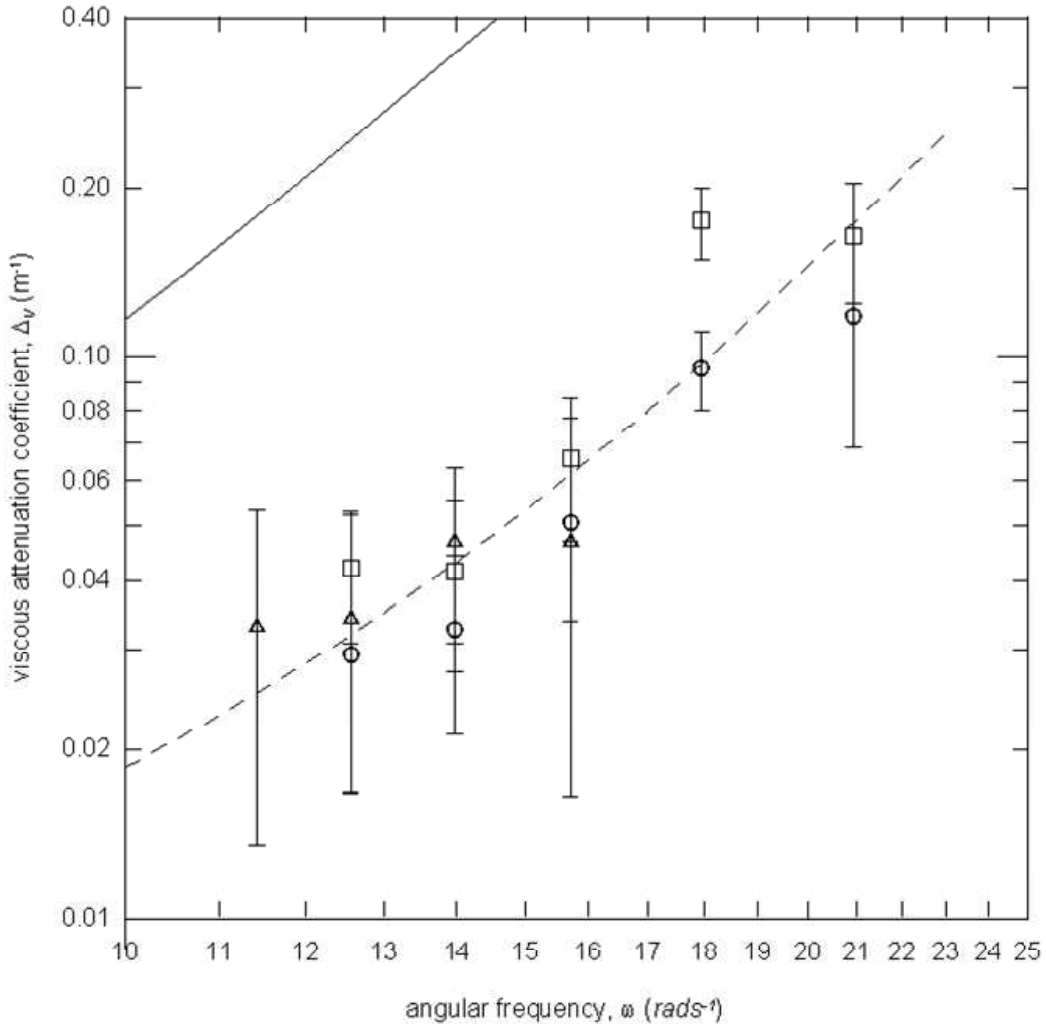

Figure 4-10. Spatial attenuation coefficient in the absence of rainfall as a function of wave frequency and mean steepness. Symbols indicate mean wave steepness as follows: triangles *ak*=0.05; circles 0.10; and, squares 0.15. Van Dorn (1966) predictions for a clean surface (dashed line) and fully contaminated surface (solid line). Note the absence of any clear dependence on mean wave steepness.

4.5.3 Wave attenuation induced by rainfall

Figure 4-11 shows the attenuation coefficient due to rainfall (Δ_R) calculated by deducting the van Dorn (1966) viscous attenuation (Δ_V) from the rainfall-influenced attenuation data (Δ_T), from the LR and HR cases.

The total attenuation rate in the presence of rain is systematically between 1.3 and 2.0 times higher than the attenuation rate in the absence of rain (Figure 4-10 and Figure 4-11). However, no systematic difference can be observed between the attenuation rates obtained under different rainfall scenarios (Figure 4-11). This finding is consistent with the findings of Tsimplis (1992) and Poon *et al*. (1992) in spite of the markedly different conditions under which each of those studies was undertaken. A threshold rainfall rate or KEF_{rain} for variable wave attenuation rate has not been previously reported and is yet to be identified.

Further, the attenuation rate does not change as a function of the wave steepness, a finding also previously established by Tsimplis (1992) and Poon *et al*. (1992). A remarkable fact considering that the attenuation rates determined by these three studies are significantly different.

The attenuation rates obtained by these different studies are markedly different. The attenuation rates obtained by Tsimplis (1992) are systematically lower than those found during this investigation. Nonetheless, the frequency dependence of the Tsimplis (1992) data is similar to that of the present study with the mean attenuation curves forming a systematic upper envelope.

At higher frequencies, attenuation rates measured by Poon *et al.* (1992) coincide with the mean attenuation curves of this present study. However, the Poon *et al*. (1992) data show very weak frequency dependence in comparison with both Tsimplis (1992) and the present study. Consequently, at an angular wave frequency of ~11$rads^{-1}$, Poon

et al. (1992) measured attenuation rates that are an order of magnitude higher than those obtained during this study. Note that Poon *et al.* (1992) data also shows growth due to rainfall which is indicative of possible inaccuracies due to the small scale of the waves they generated in their facility when compared with the normal size of the rainfall generated ripples.

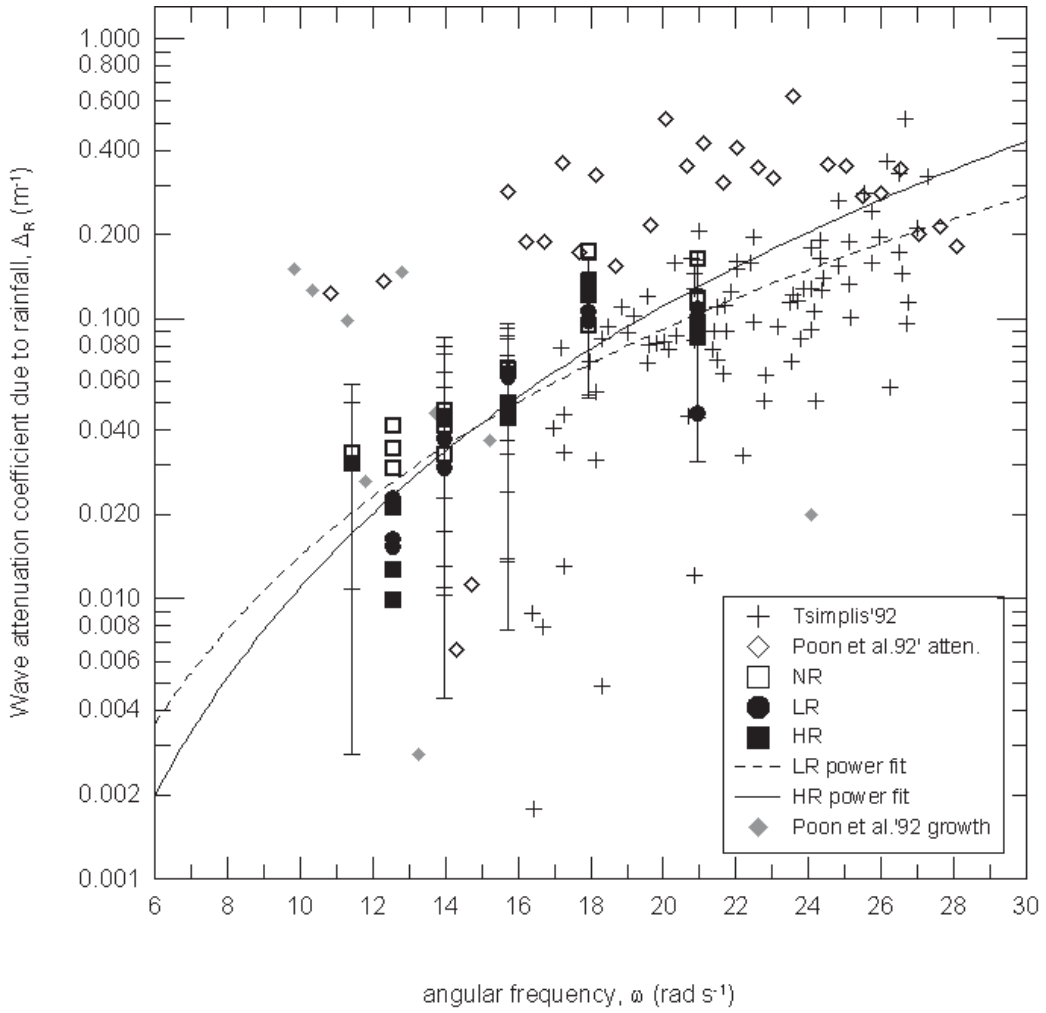

Figure 4-11. Wave attenuation coefficient due to Rainfall obtained subtracting the van Dorn (1966) viscous attenuation. NR (no rainfall, only viscous tank and surface attenuation), hollow squares. LR, circles. HR, solid squares. Tsimplis (1992), crosses. Poon *et al.* (1992) attenuation, hollow diamonds. Poon *et al.* (1992) growth, gray filled diamonds. Dashed ($\Delta_R=2.9\text{x}10^{-5}\omega^{2.69}$) and solid ($\Delta_R=5.0\text{x}10^{-6}\omega^{3.33}$) lines correspond to best fit curves to LR and HR data respectively. Measured attenuation coefficients follow a similar trend and an upper bound to the scattered data in Tsimplis (1992). No dependence on wave steepness nor rainfall intensity was detected confirming Tsimplis (1992) and Poon *et al.* (1992) findings. Error bars for LR and HR data correspond to 90% confidence intervals as in Peirson *et al.* (2003).

4.5.4 Comparison with turbulence attenuation theories

In section 2.3 two theoretical turbulence attenuation coefficients were described. Teixeira and Belcher (2002) was applied using a value of $u'=3.3mms^{-1}$ obtained from an

extrapolation at a depth $z=-z_0=-23mm$ of the power fit model of the measured turbulence profile (Figure 4-8). The use of this value requires increasing the original constant α in equation (2-17) by a factor of 35 in order to match the observations. This may be indicative of enhanced turbulence induced wave attenuation caused by rainfall-triggered surface turbulence. Figure 4-12 shows the observed wave attenuation coefficient contrasted with the Teixeira and Belcher (2002) model with the increased α constant.

The Boyev (1971) expression is more complicated. However if the turbulence spectrum is simplified to the form of Figure 2-1 and the value of the exponential in equation (2-18) is assumed negligible when $k>>s$, the attenuation coefficient is approximately proportional to ω^2. Figure 4-12 also shows a best fitted ω^2 curve representing the Boyev (1971) model. More information about a wave number spectrum which could characterise the measured turbulence profile is required to compute Boyev (1971) attenuation rate to a greater level of detail.

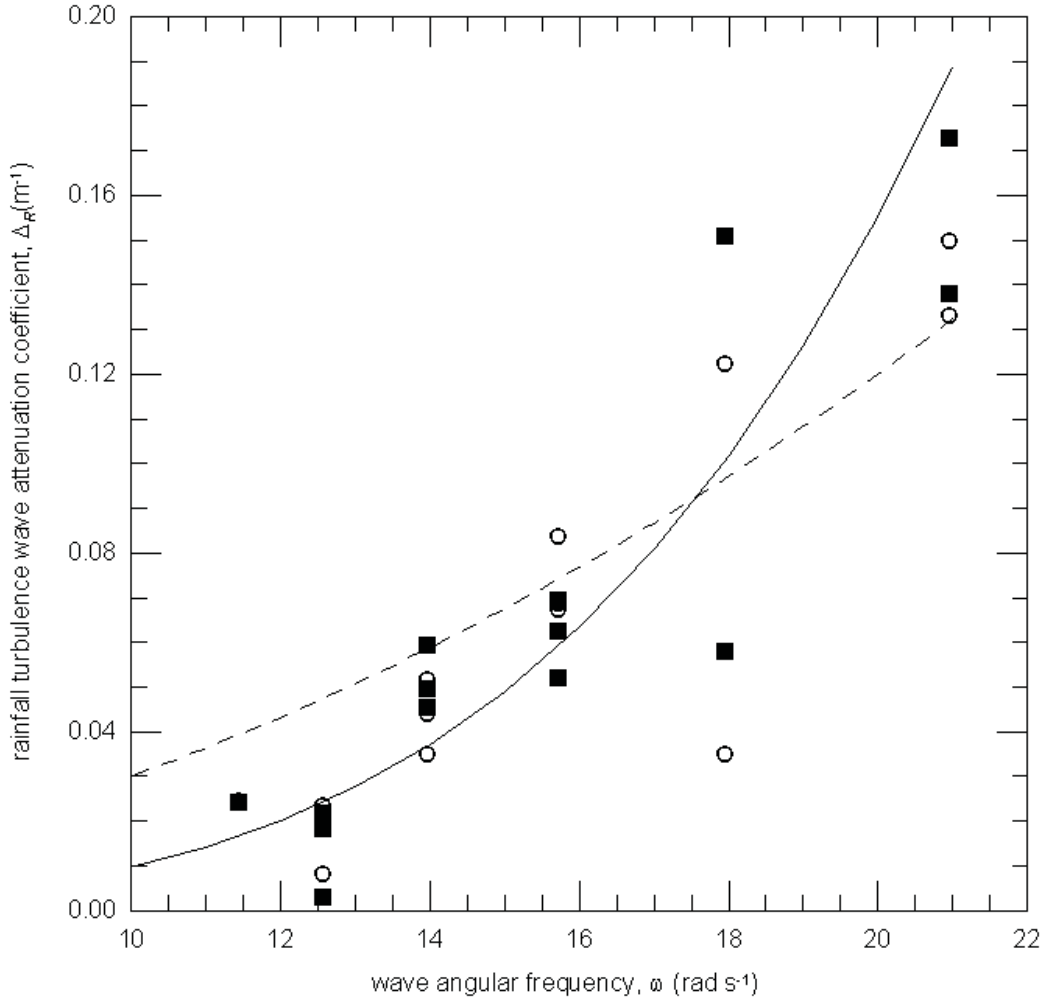

Figure 4-12. Observed wave attenuation coefficient due to rainfall compared to theoretical estimates. LR (circles), HR (squares), Teixeira and Belcher (2002) (solid line) and a simplification of Boyev (1971) proportional to ω^2 (dashed line).

Observations agree, in a broad sense, with theoretical estimate of Teixeira and Belcher (2002). Both models require a turbulence intensity value representative from a depth-decaying profile (Figure 4-8). Note that a rapidly decaying turbulence profile resembles adequately conditions in the ocean under whitecapping and wind shear (Terray *et al.* 1996, Craig and Banner 1994). Teixeira and Belcher (2002) recommend the use of *u'* measured at a depth equal to the integral length (*l*). However there are two issues with such an approach:

1. Their rapid distortion turbulence theory assumes a turbulence profile based on Hunt and Graham (1978) where grid-generated turbulence is convected by a free stream and blocked by a solid boundary moving at the same speed of the mean flow. This is conceptually a different process to what occurs in the ocean where turbulence is generated at the surface and diffused down the water column (Craig and Banner 1994).
2. The integral length varies with depth (Figure 4-4, Craig and Banner 1994).

On the other hand, in this study, the weak levels of measured turbulence and the invariance with rainfall rate did not yield the anticipated broad range of turbulence intensities that could be contrasted with theoretical estimates.

4.6 Discussion

The original objective of the experiments in this study was to measure the attenuation of waves caused by different levels of surface turbulence controlled by varying the intensity of simulated rainfall (i.e. rainfall KEF_{rain}) in order to provide a suitable data set to validate existing wave-turbulence interaction theories. This was based in the concept of a direct dependence between KEF_{rain} and levels of subsurface turbulence, a concept embraced in several previous studies (Tsimplis 1992, Ho *et al.* 2000, Zappa et al. 2009) without empirical verification.

Present observations showed that turbulence was not as strong as previously envisaged. Further, turbulence and wave attenuation were found to be weakly dependent on rainfall intensity. These findings, although initially unanticipated, were found to be consistent with:

1) Braun (2003) who found similar levels of rainfall induced turbulence by testing a wide range of rainfall rates (see section 4.1.4).

2) Poon *et al.* (1992) and Tsimplis (1992) whose measurements of wave attenuation due to rainfall showed no significant differences between varying rainfall rates.

3) Bliven *et al.* (1997) who reported a weak variation in the raindrop wave spectra for different rainfall rates. Their measurements involved a broad range of rainfall intensities generated with a tall hypodermic needle rainfall simulator in which raindrops achieved impact velocities close to terminal. They as well as Tsimplis (1992) and Poon *et al.* (1992) recommended wave and turbulence measurements to resolve whether a possible "saturation" limit due to the interaction between rain waves and turbulence exists.

Figure 4-13 shows a comparison of different rainfall generated wave spectra. Preliminary measurements carried out without roofing over the wave probes are shown and compared with Bliven *et al.* (1997). A visual and a spectral comparison showed that the wave probe roofs (section 4.2) used in the definite wave attenuation measurements significantly filtered the rain generated ripples. Note the undistinguishable variation between measured spectra with and without propagating paddle waves for frequencies greater than $20 rads^{-1}$. Note also in Figure 4-6 a similar effect between the two rainfall scenarios.

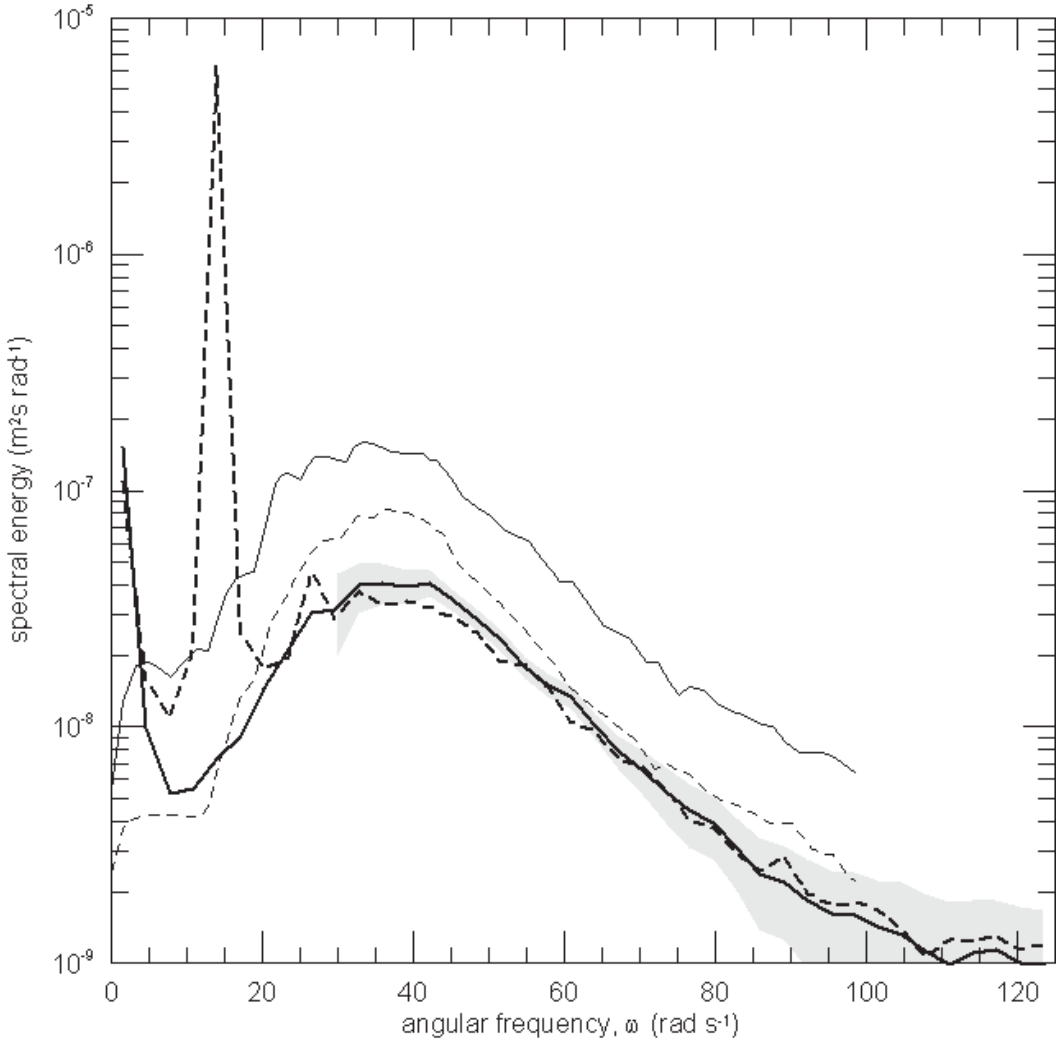

Figure 4-13. Comparison of wave spectra generated under different rainfall conditions. Heavy solid and dashed lines show preliminary LR data without roofing over wave probes. Heavy solid line shows spectrum measured with no paddle waves generated. Dashed heavy line shows an example spectrum for LR test case 18 (ω=11.4$rads^{-1}$, ak=0.10). Thin dashed and solid lines show spectra from Bliven *et al.* 1997 cases 50mmh^{-1} and 200mmh^{-1} respectively. Gray area represents statistical error above 30$rads^{-1}$ obtained from all measured wave spectra.

Rain ripples have the potential of contributing to the measured velocity fluctuations near the surface. Estimates of the potential contribution of the rain wave orbital velocities, based on the most energetic rain spectrum measured by Bliven *et al.* (1997) (Figure 4-13), indicate that they could add approximately 50% of the measured fluctuating velocities at 31*mm* depth reducing to a potential 30% contribution at 62*mm*

depth. However rain-wave turbulence interaction at the surface can cause the rapid destruction of the rain-wave orbitals and the contribution could be negligible.

Nevertheless, non-turbulent high frequency motion was not evident from the measurements results, particularly in the velocity fluctuations spectra which showed a shape compatible with a Kolmogorov type of turbulence spectrum.

4.6.1 Energy balance at the water surface

Some of the questions arising from the discussion above are: Where does the rainfall energy go? And, how much of the input energy goes to subsurface turbulence?

Figure 4-14 shows a scheme of the energy balance in the water column for rain falling on still water. Estimates of the energy fluxes indicate that a small percentage of the rainfall energy is transferred to subsurface turbulence (Table 4-4).

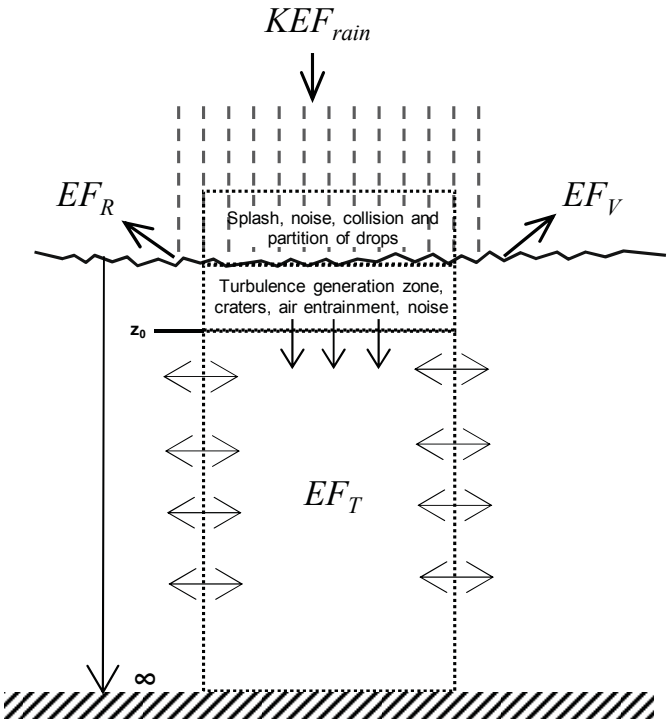

Figure 4-14. Scheme of energy balance for rainfall falling on still water surface. See symbol definitions in Table 4-4.

Table 4-4. Energy fluxes of rain falling on a still water surface.

Type of Energy Flux	Symbol	Energy flux LR (Wm^{-2})	Energy flux HR (Wm^{-2})
Rainfall kinetic energy	KEF_{rain}	0.850	1.110
Subsurface turbulence dissipation	EF_T	-0.001	-0.001
Viscous attenuation of rain waves	EF_V	-0.004	-0.004
Turbulent attenuation of rain waves	EF_R	-0.013	-0.044

Energy fluxes were calculated upon the following considerations:

1. Zero net horizontal flux assuming horizontal homogeneity.

2. The input rainfall kinetic energy flux (KEF_{rain}) can be calculated using equation (4-1) and assuming the raindrop size distribution given in Shelton *et al.* (1985) for the rainfall simulator.

3. The subsurface turbulence dissipation (EF_T) can be calculated using the measured turbulence profiles (Figure 4-8), equation (2-9) with A=1 combined with equation (4-2).

$$EF_T = -\int_{z_0}^{\infty} \rho \cdot \varepsilon(z) dz \tag{4-8}$$

4. The viscous attenuation of rain waves (EF_V) can be calculated using the rain ripples wave spectrum (S_w) in Figure 4-13, the capillary-gravity linear equations (section 2.1.3 and Phillips 1977, p.37-38) and equation (2-8).

$$EF_V = -\int 4 \cdot \mu \cdot \omega^2 \cdot S_w(\omega) \cdot k \cdot d\omega \tag{4-9}$$

5. The turbulent attenuation of rain waves (EF_R) can be calculated from (Phillips 1977, p.70) and equation (2-7). The rain-wave spectrum was obtained as explained above, the wave group velocity from the linear capillary-gravity equations, and the rainfall wave attenuation from the power fit model in (Figure 4-11) assuming it is valid in the high frequency range.

$$EF_R = -\int \rho \cdot g \cdot S_w(\omega) \cdot c_g(\omega) \cdot \Delta_R(\omega) \cdot d\omega \tag{4-10}$$

Table 4-4 shows that the energy transfer from rainfall to subsurface turbulence is a very inefficient process. Further, rain-wave viscous (EF_v) and turbulent dissipation (EF_R), consume a greater proportion of the energy input (KEF_{rain}) than the subsurface turbulence dissipation (EF_T). However, all these processes together, EF_V, EF_R and EF_T, dissipate less than 5% of the total energy input (KEF_{rain}). It appears then, that the

majority of the energy dissipation occurs within the first few centimetres of the air-water interface where the complex interaction between raindrops and the water surface induces unexplained potentially dissipative processes such as noise, air entrainment, splash, air collision and partition of rain drops.

The proportion of the energy transferred to subsurface turbulence is very low and insensitive to variations in the rainfall intensity. Instead, transfer ratios are expected to increase with raindrop size (Green and Houk 1979). Energy flux calculations confirmed the unanticipated but observed invariability of the wave attenuation and turbulence levels with the rainfall rate.

5 NON-TURBULENT FLOW UNDER NON-BREAKING WAVES

5.1 Background

Recently, a laminar-turbulence transition wave parameter ($a^2\omega/\nu$) has been proposed by Babanin and Haus (2009) to explain the appearance of turbulence under non-breaking, monochromatic, deepwater laboratory waves (ω=9.42$rads^{-1}$, d=0.38m). The transition was identified using PIV measurements immediately beneath the troughs of waves for a wide range of steepnesses (ak<0.29). Dissipation rates greater than $10^{-3}m^2s^{-3}$ were obtained from the sporadic appearance of a Kolmogorov-type spectrum leading to their proposed threshold value of $a^2\omega/\nu$=3000 that was determined for the occurrence of turbulence.

Babanin and Haus (2009) can be compared with a theoretical analysis found in Kinsman (1984, p.510). Using conventional turbulence scaling analysis and diffusion of vorticity, it was shown that wave-induced turbulence is a third order effect governed by a Reynolds wave turbulence parameter defined as $R_W=\omega/(\nu k^2)$, and further stated, since in the ocean R_W is very large, the wave induced turbulent attenuation can be neglected. Note the counter-intuitive inverse relation between a Reynolds number and the occurrence of turbulence in this case. No independent empirical verification of this analysis has been found.

If borne out, the findings of Babanin and Haus (2009) have potentially significant and widespread implications in the current understanding of ocean waves. Is it possible that past experiments failed to identify the presence of turbulence beneath waves due to the small scale of their experiments or lack of sensitivity of their instrumentation? Do freely propagating waves produce surface shear capable of creating

turbulence? Is this high level of turbulence under waves indicative of a fundamental flaw in conventional irrotational wave theory? The potential significance of this finding motivated a careful examination using direct measurements of wave motion above the wave trough level designed to detect the initiation of turbulence under freely propagating waves. Observations above the wave trough have only been attained by few investigators (Swan 1990a, Peirson 1997). Before proceeding to describe these experiments and the consequent findings, it is useful to revisit previous measurements in the context of the parameter $a^2\omega/\nu$.

Figure 5-1 summarises relevant previous experimental studies. Careful experiments by Longuet-Higgins (1960) showed no sign of turbulent motions. These experiments were undertaken at smaller values of $a^2\omega/\nu$ and may not be expected to detect such a transition in view of the proposed threshold parameter.

The validity of Stokes wave theories were extensively examined by Wiegel (1964) and included time exposure photographs of wave orbitals (p.19) which supported the assumption of a non-turbulent condition within the subsurface flow. Wiegel (1964) experiments were undertaken at large scales but it is possible that his visualisation techniques were not sufficiently sensitive to detect the presence of turbulence. Swan (1990a) compared laser velocity measurements of monochromatic waves with Fenton (1985) finding excellent agreement. However his data showed fluctuating velocities within an intensity of $0.02ms^{-1}$ that could be indicative of turbulence, instrument noise or variations in the wave field. Consequently, these previous experiments do not provide conclusive contradictory or collaborative findings to those of Babanin and Haus (2009).

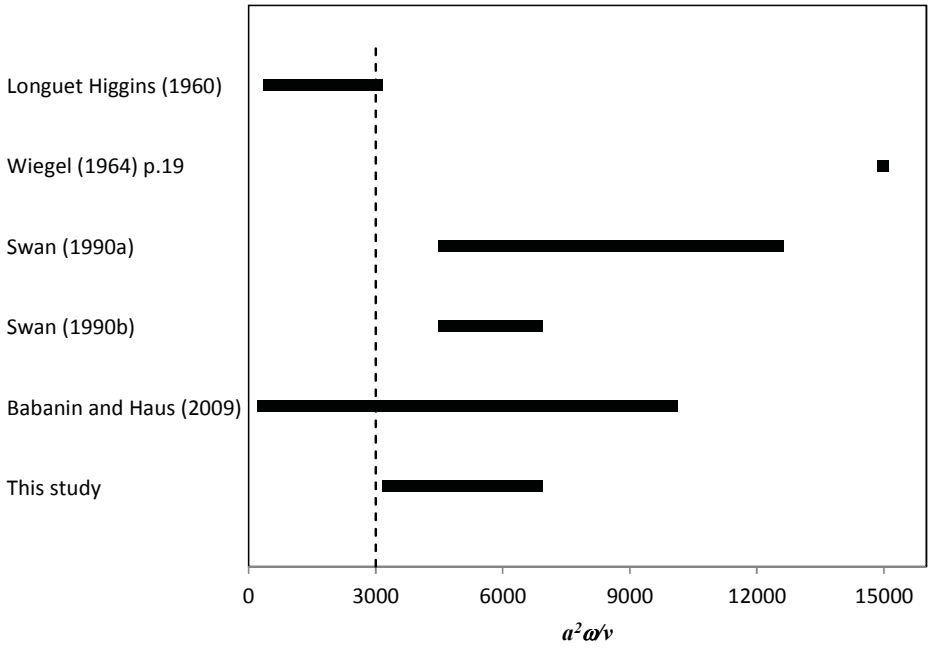

Figure 5-1: Range of $a^2\omega/\nu$ for relevant experimental wave studies. Longuet-Higgins (1960) and Swan (1990a) used waves in transitional depths. All other studies in this comparison used deep water waves ($k_0 d > \pi$), k_0=linear theory wavenumber. Vertical dashed line shows transitional value in $a^2\omega/\nu$.

5.2 Experimental method

5.2.1 Test Facility

The experiments were carried out in the wave tank as described in section 3.1. The tank was cleaned and filled with clean tap water before the experiments to a depth of $0.405m$. To ensure that no residual turbulence diffused along the tank, the fan and the waves were stopped and a clean plastic sheet was placed on the water surface at the end of the tank in order to stop the slick returning to the cleaned surface, as used by Longuet-Higgins (1960). The wave tank was left to settle for one hour taking care that air currents and any movement in the water were minimal.

A steep monochromatic wave train of angular frequency ω=9.42$rads^{-1}$ was generated for 3 test cases from a still water starting condition. Between tests a solid

screen was carefully placed in the middle of the tank for 5 minutes in order to dissipate any seiche motions in the tank. Then the screen was carefully removed and the next test was run when water movement was minimal.

Observations were undertaken at a distance of 5.25*m* from the wave generator in order to match similar experimental conditions to those in Babanin and Haus (2009).

Wave trains were measured using the equipment and techniques specified in section 3.3. Characteristic wave train heights (H) and periods ($T=2\pi/\omega$) were obtained with a zero crossing analysis.

5.2.2 Dye visualization experiments

Dye visualisation techniques have been used to detect fluid velocities and turbulence since the birth of turbulence research over one hundred years ago (Reynolds 1883).

For this investigation, the flow visualisation was carried out by placing an approximately 2.5*mm* diameter magnesium permanganate crystal at the bottom of a slightly conical plastic tube. The tip of the plastic tube was rigidly supported so that it just touched the water surface at the centre of the tank. Contact with the water caused the crystal inside the tube to dissolve, yielding a dense, intensely-coloured descending plume of dye with a diameter of approximately 3*mm*. Slight modulations in the dye dissolution created identifiable features in the developed dye line.

Dye lines were also possible to be created in the presence of waves by dropping a small permanganate crystal (~1*mm* diameter) at the crest of the passing wave. Larger crystals tended to fall too fast without allowing sufficient contact time to dissolve and generate a line. Crystal selection was important since different shape crystals could create sinuous falling patterns. Preferred crystals had a round shape of approximately

1*mm* diameter which created significantly thinner lines that were difficult to detect. Other dye injection techniques were tested without success. No further efforts were made to improve the quality of the lines in the presence of waves since the primary objective of this investigation was to visualise turbulence under the experimental conditions of Babanin and Haus (2009), which involved waves propagating through quiescent water.

Appropriate lighting and diffusive screens were used to avoid reflections and to provide even illumination of the dye line. A Casio Exilim EX-F1 digital photo camera with a 35*mm* lens was set to observe the dye line through the glass walls of the tank. The lens was carefully focused on the dye line with the camera set looking slightly upwards below the still water level in order to visualise the fluid underneath the water surface (Peirson 1997). High definition video imagery (1280 by 720 pixels) was captured at a rate of 30 frames per second.

The wave generator was started immediately after video recording commenced. The crystal and the tube were removed as soon as movement in the water surface was perceptible at the measurement point. Wave generation ceased after 30 waves had passed the measurement point. All dye experiments were undertaken over a period of 4 hours during which time the water temperature remained at $14.6 \pm 0.2C$.

Once the suite of dye line imagery had been captured for all wave test conditions, the water level in the tank was raised by approximately 0.1*m* and a square grid was immersed into the field of view at the centre of the tank for post-processing scaling and image rectification. Sample grid points were manually digitised from the grid image to create a transformation matrix and rectify all images using the Matlab image processing toolbox (Matlab, 2010).

Images of the evolving dye lines were extracted from the video at full resolution at selected times prior to rectification. Dye features were digitized from the rectified images according to the calibration scaling. The measurement resolution achieved by the measurement system was 0.49*mm* per pixel within the measurement region of primary interest.

Wave velocities at different depths were obtained by digitising the motion of individual dye line features at 30*Hz* resolution during the measurement period. The instantaneous horizontal and vertical wave velocities (u and w) were determined using second order centred finite differences from the digitized points (Hornbeck 1974). Orbital vertical velocities were obtained from the measured instantaneous velocity time series by best-fitting an $Asin(\omega t+B)$ model, with A and B constants found with the least squares method, A corresponding to the orbital velocity (Figure 5-2).

The total horizontal displacement of the individual dye features over one wave period (the Stokes drift) was calculated from the differences between minima and maxima in the x coordinate of the digitized points (i.e. when the particle orbital motion was vertical) as this minimized the error in the determination of the horizontal displacement. The corresponding mean z coordinate for each displacement measurement was calculated by averaging the z coordinates over one wave period. See Figure 5-9 in section 5.3.3.

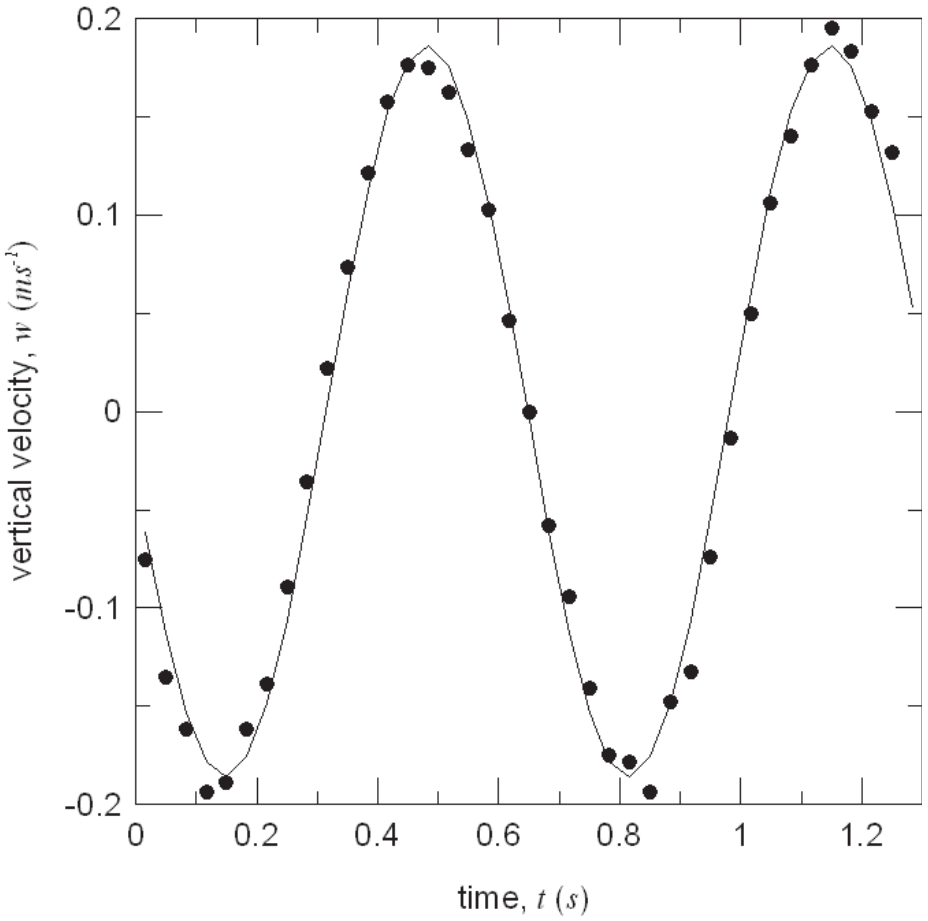

Figure 5-2: Sinusoidal model fitted to measured instantaneous wave vertical velocity measured for case 2, *z*=-9*mm*.

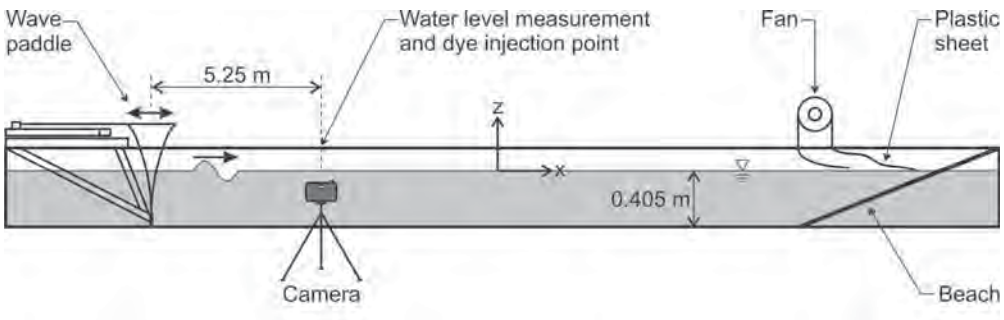

Figure 5-3: Experimental setup (not to scale).

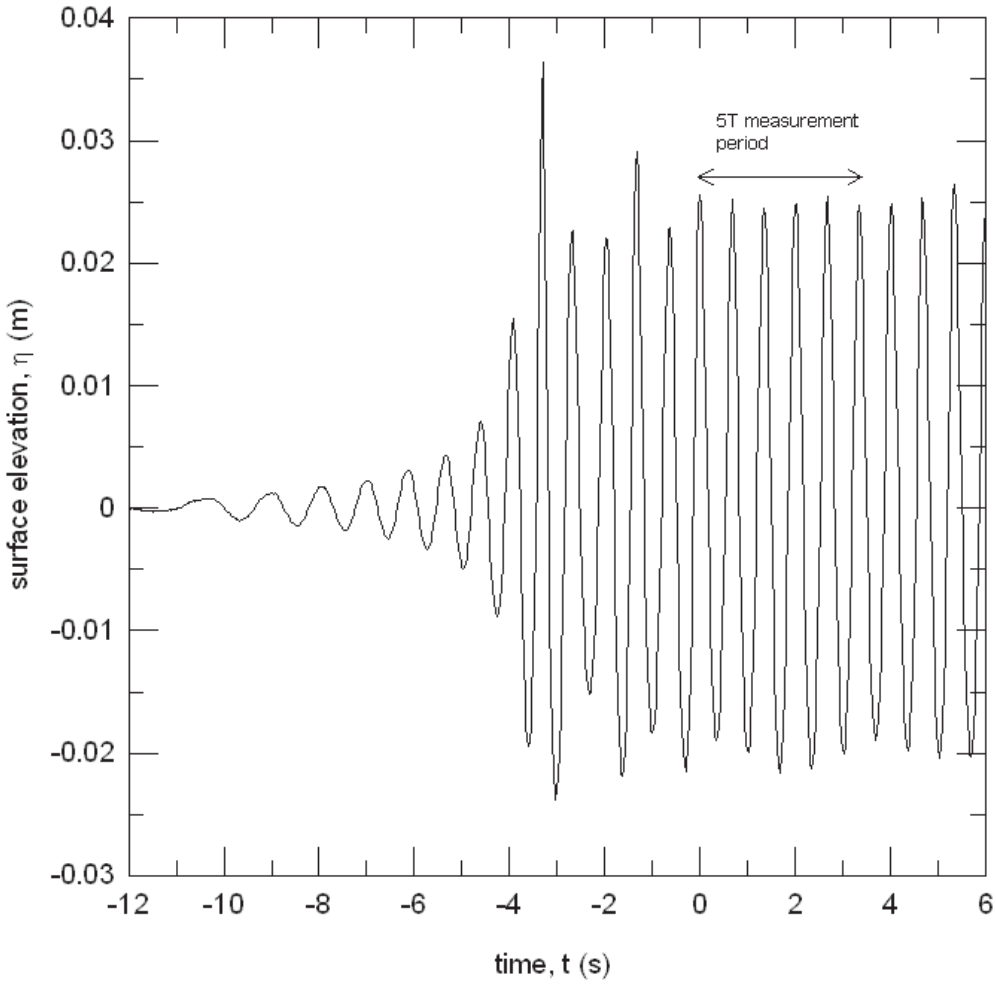

Figure 5-4: Measured surface elevation (η) time series Case 2. Note the start of the measurement period at t=0, i.e. when the wave train becomes stable five wave crests after the largest crest. Cases 1 and 3 showed similar behaviour. For all cases H was calculated as the average of the zero crossing values in the measurement period.

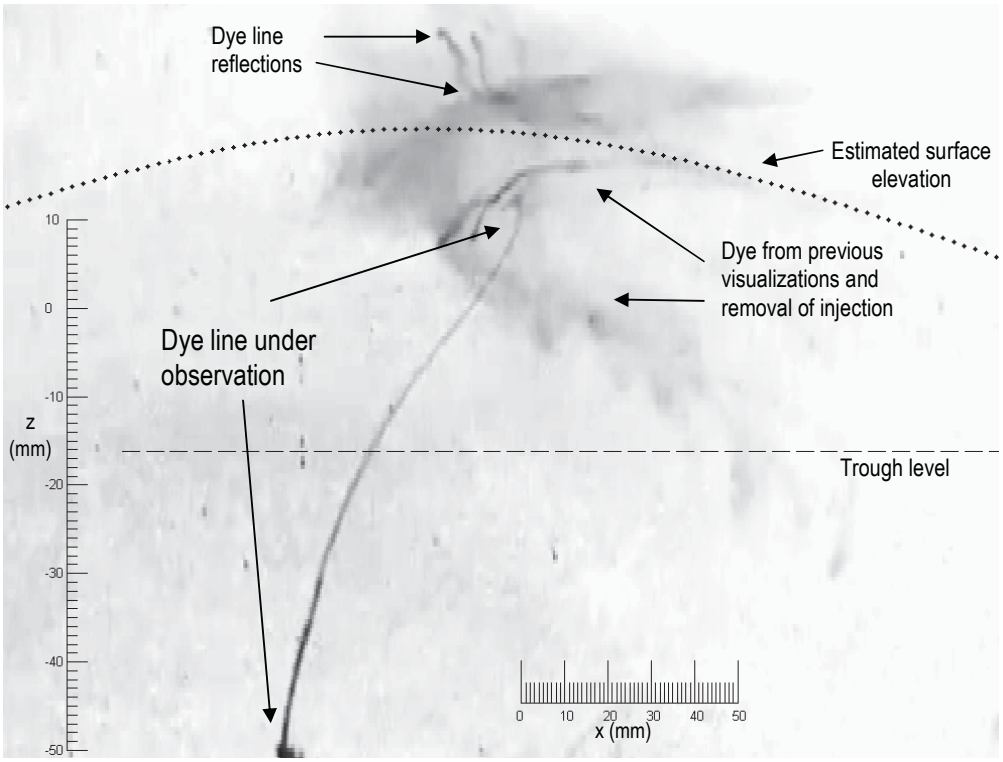

Figure 5-5: Rectified image of an evolving dye line at *t=5T* (Case 1) extracted from the video. The camera was set looking through the glass side wall below the still water level and looking slightly upwards. Note image H:V distortion shown in the scales. Note the stretching (thinning) of dye line near the surface caused by the Stokes (forward) drift, waves propagating from left to right. No turbulent dispersion of the dye line was observed even after many more waves passed. Dispersed dye patches correspond to previous visualisations and to the near-surface dye released during the removal of the injection tube. Mirrored dye features by the water surface (Reflections, centre-up) provide an indication of the water surface position. Dotted line indicates the estimated Fenton (1985) fifth order theory water surface elevation. Dashed line indicates the wave trough level. The vertical scale correspond to the *z* axis where *z*=0 is the still water level.

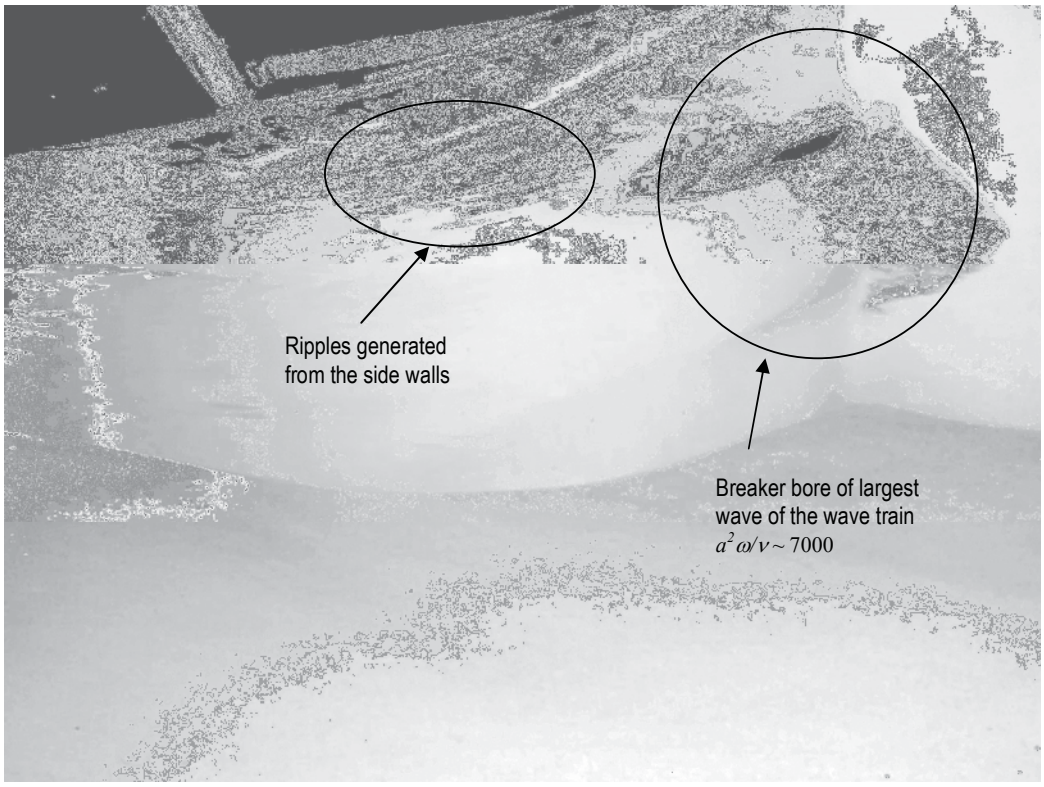

Figure 5-6: Image showing the breaking (right encircled area) of the initial largest wave shown in (Figure 5-4) for a monochromatic wave train ($a^2\omega/\nu \sim$ 7000) propagating on still water. The image was taken from the tank side wall below the water surface near the tank floor and looking up towards the surface in an angle of approximately 60°. Capillary ripples triggered by side walls can also be observed at the water surface (left encircled area).

5.2.3 Subsurface Point Velocity Measurements

Complementary fixed point, near-surface wave velocity field measurements were obtained with the ADV as described in section 3.4. Measurements were carried out for one single monochromatic wave of ω=9.42$rads^{-1}$, a=0.019m at z=-0.03m and 5.5m from the wave generator. The ADV was submerged horizontally with the head pointing upwards allowing z to be the coordinate with the lowest noise (Figure 5-3).

A time series of 8192 points was sampled at the highest rate (50Hz) in the ±30cms^{-1} velocity range. The water level was recorded after the ADV measurement as for the dye visualization experiments.

An 8192 points FFT analysis of the ADV velocity timeseries was performed to obtain a raw autospectrum. The autospectrum was then smoothed using 11 bin averages.

5.3 Results and discussion

5.3.1 Preliminary Observations

Preliminary experiments were undertaken with steep monochromatic waves with $a^2\omega/\nu$ above the threshold specified by Babanin and Haus (2009). No turbulent dispersion of the dye could be observed from the side walls or the top of the tank (Figure 5-5). However, for steep, non-breaking waves of steepness $\xi=kH/2>0.22$, capillary ripples triggered by the side walls could be observed at the water surface (Figure 5-6).

When started from rest, the wave train generated an initial larger wave as shown in Figure 5-4 which broke for waves steeper than $\xi=0.24$ (Figure 5-6). Five wave periods after this initial large wave, zero-crossing wave heights and periods observations showed that the subsequent wave train stabilized to an approximate steady monochromatic form. This dictated the start of wave probe and video monitoring during each experiment. The duration of the experiments was then determined from the visual detectability of the dye line whose intensity decreased in time primarily due to its continuous stretching by the Stokes drift.

It is important to note that the turbulence generated by the breaking of this initial wave (Figure 5-6) induced rapid mixing of the dye line that was observed to continue in bursts for several wave periods. The mixing deepened with time to a depth greater than the wave height, in qualitative agreement with Rapp and Melville (1990).

On the basis of these preliminary observations, three wave height cases were selected for detailed investigation with $a^2\omega/\nu > 3000$ while carefully avoiding the

triggering of turbulence by wave breaking during the initial wave field formation. The conditions of each experiment are summarised in Table 5-1.

Table 5-1: Test cases monochromatic wave train generated from a still water start condition. (ω=9.42$rads^{-1}$, $k_0=\omega^2/g$=9.05$radm^{-1}$, $c_0=\omega/k_0$=1.041ms^{-1}, d=0.405m water depth).

Case		1	2	3
Half wave height, *H/2* (*mm*)		18.7 ± 0.2	22.7 ± 0.1	26.9 ± 0.3
Wave steepness, ξ		0.17	0.21	0.24
$a^2\omega/\nu$		3295	4856	6819
Wave number, k ($radm^{-1}$)	Doppler-shifted	9.14	9.17	9.21
	Fifth order	8.88	8.91	8.94
Fifth order wave speed, c (ms^{-1})		1.032	1.029	1.025
Mean return veloc., $\bar{U}$ (mms^{-1})	Stokes	-4.1	-6.0	-8.4
	Fifth order	-3.6	-5.2	-7.2
	* Direct meas.	-3.2	-5.4	-7.1
	* Best fit	-3.1	-4.9	-7.6

Note: Discussion and explanations of the wave number and mean return velocity calculation methods and results are described in detail in the text.

5.3.2 Presence of Turbulence

For each test case, the thickness of the dye line was measured at different depths at t=0 and t=5T in order to quantify the turbulent mixing caused by the wave motion (Figure 5-4). Note that in absence of turbulence, the dye line could potentially reduce in thickness due to stretching associated to the Stokes drift. This effect is shown in Figure 5-5 where the thickness and the colour intensity of the dye line decreases near the surface. Note also the general narrowing of the line in time caused by the stretching. The 5T time interval was selected as the monitoring period because for longer time intervals the stretching made difficult the detection of the dye line close to the surface.

In the dye line experiments, the fact that the line could still be identified, i.e. its thickness measured, indicates that no turbulent mixing had taken place (Reynolds 1883). This is contrary to the conclusions of Babanin and Haus (2009).

Babanin and Haus (2009) showed a velocity spectra in which the turbulence integral length, l, is O(5mm), (see their Figure 1), and reported turbulent dissipation rates, ε, O($10^{-2} m^2 s^{-3}$) for $a^2\omega/\nu$>3000 (see their Figure 2). These ε levels are comparable to the highest near surface values observed under strong winds in Lake Ontario (Terray *et al.* 1996). For an ε value O($10^{-3} m^2 s^{-3}$) the turbulent velocity fluctuations, u', must be O($0.02 ms^{-1}$) taking in consideration the scaling relation in equation (2-9).

This u' value is large and about 10% of the maximum orbital velocity near the surface (Figure 5-8) but is smaller than the accuracy of their PIV system ($0.03 ms^{-1}$ see their p.2677). Present experiments showed no turbulent velocity fluctuations of that order of magnitude (Figure 5-5 and Figure 5-11).

a)

b)

c)

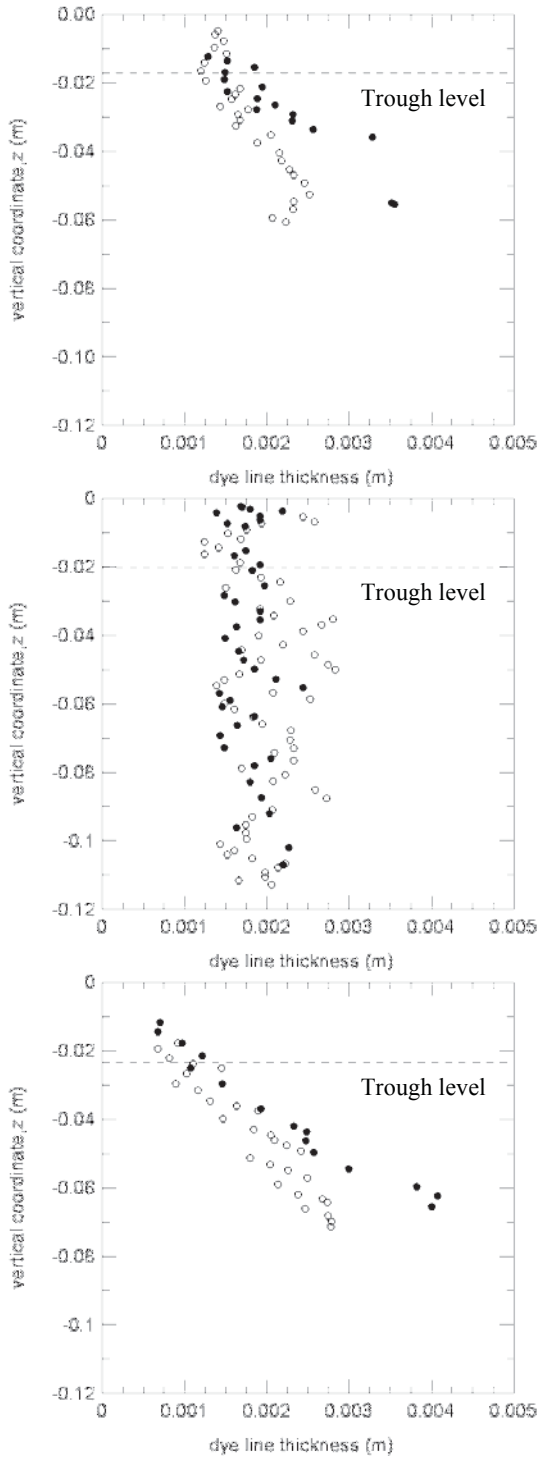

Figure 5-7: Vertical profile of dye line thickness at time (t=0) (solid circles) and (t=5T) (hollow circles). a) Case 1, Fig. b) Case 2, Fig. c) Case 3. Horizontal dashed lines indicate estimated fifth order trough levels.

5.3.3 Wave Orbitals

Orbital velocities from dye observations were compared and showed good agreement with Fenton (1985) fifth order wave theory (Figure 5-8). Errors bars show the standard error obtained with the fitting technique explained earlier. Note the difference of approximately 20% in the near-surface values for the steepest case.

The dye features showed open orbital trajectories as predicted by Stokes theories (Figure 5-9). A comparison with Fenton (1985) fifth order theory was carried out by integrating the particle paths using a fourth order Runge-Kutta method to solve:

$$\frac{\partial x_i}{\partial t} = \frac{\partial \Phi}{\partial x_i} \qquad (5\text{-}1)$$

where x_i is the position in the *'i'* direction.

Note the increasing difference in time between predicted and theoretical particle trajectories due to the integration of the uncertainties in the wave parameters in equation (5-1), (Figure 5-9).

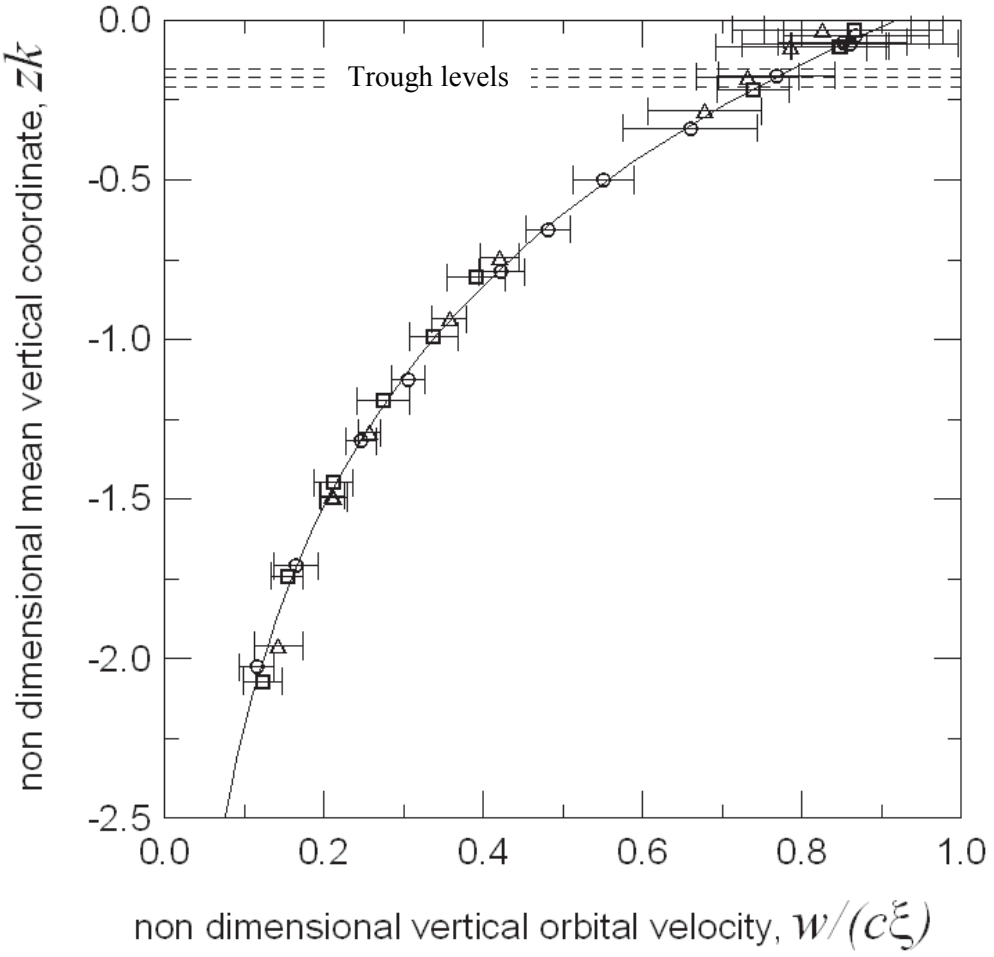

Figure 5-8: Vertical orbital velocities (symbols) compared with Fenton (1985) fifth order theory prediction (solid line). Case 1, circles; Case 2, squares; Case 3, triangles. Horizontal dashed lines indicate estimated fifth order trough levels for cases 1, 2 and 3 in descending order. Theoretical predictions for the different cases collapsed almost identically when plotted under this non-dimensional form.

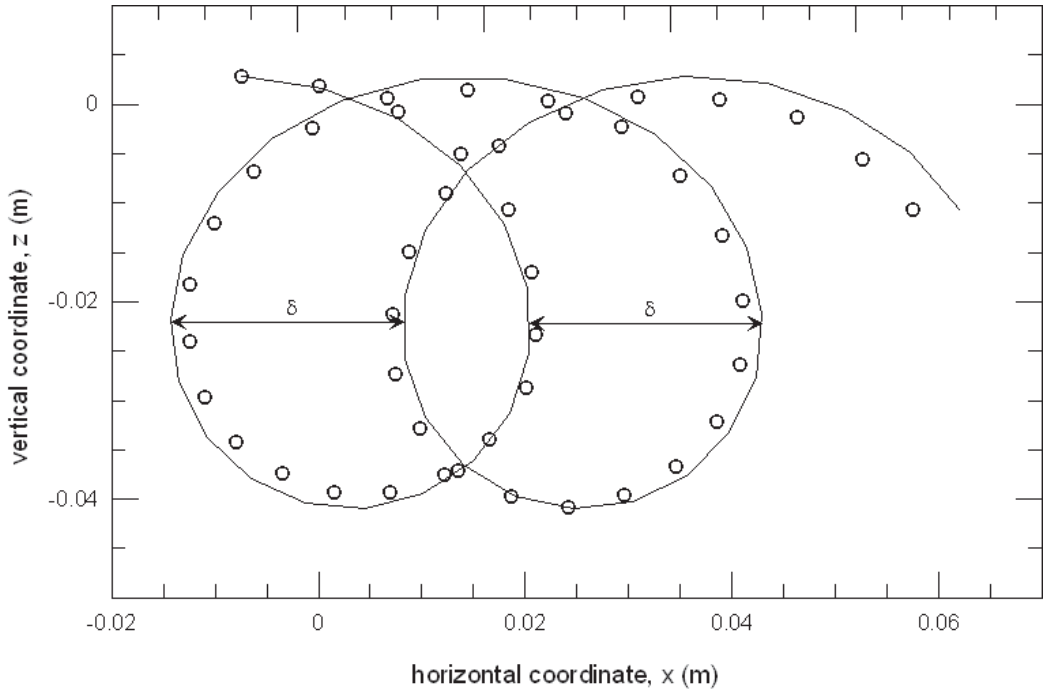

Figure 5-9: Measured particle trajectory, z=-0.02*m*, Case 3 (circles) from the dye visualization experiment and fifth order theory (solid line). Arrows indicate measured total particle displacement over one wave period where the mean velocity at the average z is estimated as δ/T. Note the significant difference in position between the theoretical and measured Stokes drift after 2¼ wave cycles.

5.3.4 Stokes Drift

Stokes (1847) wave theory predicts a mean velocity in the direction of wave propagation, the Stokes drift, see equation (2-5). Kinsman (1984), p.258 extended the Stokes drift formula to third order.

$$U_s(z)=\xi^2 c\, e^{2kz} \qquad (5\text{-}2)$$

At second order, Stokes theory corrections to the extreme water elevations are identical, and consequently, a=H/2 exactly making ξ=ak and equations (2-5) and (5-2) equivalent. However, at higher order, modifications to the crest and trough amplitudes are no longer identical and $\xi \neq ak$ (Table 2-1).

In closed systems, including wave tanks, surface waves must induce a mean velocity ($\bar{U}$) that is opposite in direction to wave propagation and balances the Stokes drift. $\bar{U}$ can be assumed to be uniform with depth and is calculated as the integral of the Stokes drift over the water depth (Wiegel 1964, p.32).

Depth averaging equation (2-5) provides a direct estimate of $\bar{U}$:

$$\overline{U} = \frac{-a^2\omega}{2d}(1 - e^{-2kd}) \tag{5-3}$$

On the other hand, by definition, $\bar{U}$ must also be the time and depth average of the horizontal velocity.

$$\overline{U} = -\frac{1}{Td}\int_0^T \int_{-d}^{\eta(t)} \frac{\partial \Phi}{\partial x} dz dt \tag{5-4}$$

The calculation of equation (5-3) and (5-4) require iterative methods that consider Φ, η, $\bar{U}$, k and c as functions of k and ω (eq. (5-5) and Fenton 1985, eqs. 26, 27 and 31). Conventional Stokes theories (Wiegel 1964, p.31) do not include such effects which must be corrected using the Doppler-shifted dispersion relation in equation (5-5) and adding $\bar{U}$ to the horizontal velocity (Massel 1996, p. 266).

$$\left(\omega - \overline{U}k\right)^2 = gk\tanh(kd) \tag{5-5}$$

Table 5-1 shows measured and theoretical mean return velocities. Theoretical values were calculated according to the Stokes and fifth order theories (equations (5-3) and (5-4) respectively). Measured mean return velocities were obtained by two methods:

1) A direct measurement of the displacement of the deepest dye features recorded. Measurements were undertaken at kz~2.1 where the influence of the Stokes drift can produce errors of approximately 14%.

2) A fit to the exponential decline of the mean velocity in Figure 5-10. A $\ddot{\zeta}^2 ce^{Akz}+B$ model based on equation (5-2) was fitted minimizing the least squared relative error, with A and B constants to be determined, B corresponding to $\bar{U}$.

Both methods produce values with errors less than 14% of the fifth order estimates. This is remarkable considering the small values of $\bar{U}$ and it is indicative of the consistency of the measurements and the validity of the assumption that modifies the wave number and velocity field by deducting a constant mean return flow, $\bar{U}$, that balances the integral Stokes drift in a closed system, (Fenton 1985, Wiegel 1964, p.32).

The least squares fit in the second method yielded a Stokes exponent constant A=2.12±0.06. This result is remarkable though 6% higher than the Stokes drift formula which predicts a value of A=2.

Table 5-1 also shows the wave number calculated for the Doppler–shifted Stokes (1847) and the fifth order theories (equation (5-5) and Fenton 1985, eq.26). Note the counter-intuitive decrease in the wave speed with the wave steepness caused by the increase in the mean return velocity.

Mean flow measurements agree reasonably well with Stokes (1847) prediction, though the near surface, values are systematically lower in approximately 20%, (Figure 5-10). Significantly higher near surface values would be expected if the Stokes drift gradient increase anticipated by the Longuet-Higgins (1953) viscous boundary layer theory was present.

The method used to estimate the Stokes drift from the dye measurements was validated using synthetic particle trajectories calculated from the fifth order theory and by solving equation (5-1) (Figure 5-8). The mean velocity obtained this way was almost indistinguishable from the U_s value obtained from equation (5-2).

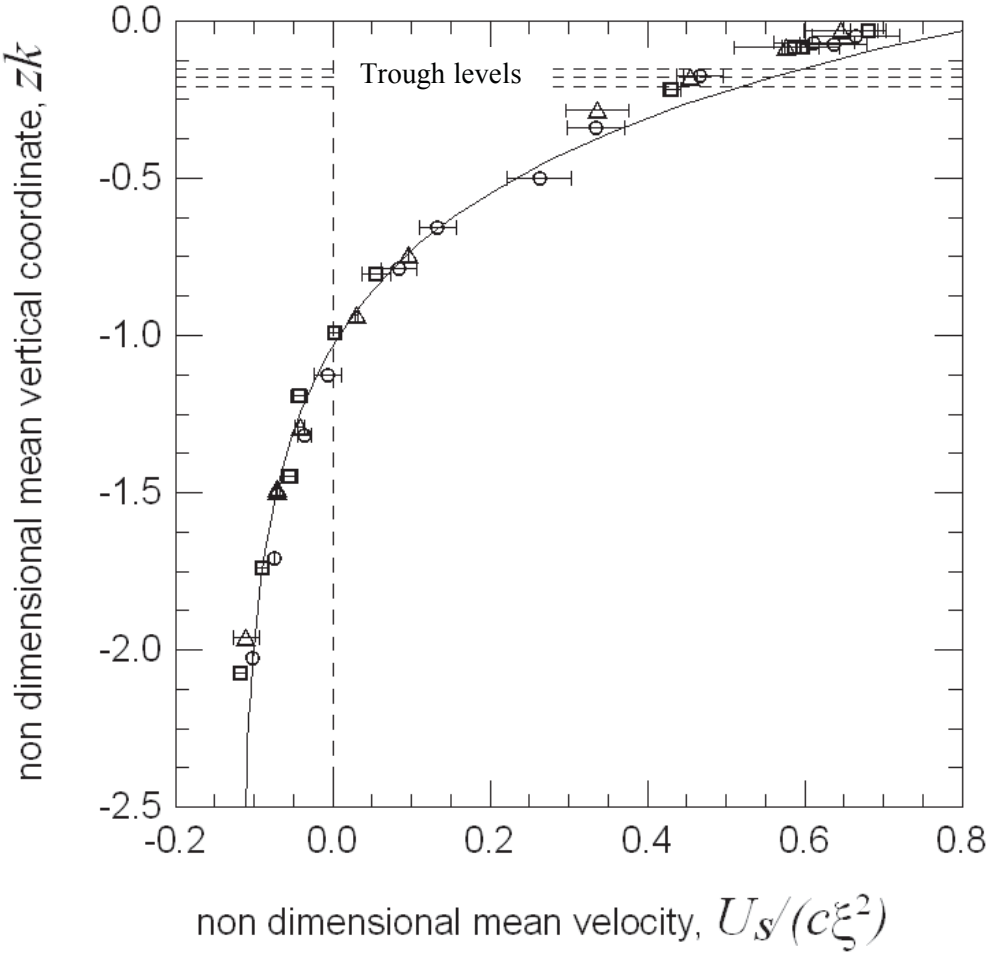

Figure 5-10: Measured Stokes drift (symbols) compared with theory (solid line). Case 1, circles; Case 2, squares; Case 3, triangles. Horizontal dashed lines indicate estimated fifth order trough levels for cases 1, 2 and 3 in descending order. Theoretical predictions for the different cases collapsed almost identically when plotted under this non-dimensionalised form.

Longuet-Higgins (1953) extended Stokes theory to explain the existence of bottom boundary layer transport in wave tank experiments by determining the vorticity generated within the viscous boundary layers adjacent to the water surface and the bed. The theory predicted an increase in the Stokes drift gradient near the surface which induces a second order vorticity diffusing from the surface on a time scale $O(z^2/\nu)$. It is to be noted that the existence of this second order vorticity does not imply turbulent flow. His findings were verified by laboratory experiments (Longuet-Higgins 1960).

The time scale $O(z^2/\nu)$ needed for the diffusion of the vorticity indicates that the dye visualization experiments were not significantly influenced by wave induced vorticity diffusion. Measurements were taken between 12*s* and 16*s* after movement in the water was perceptible (Figure 5-4) indicating that only observations at depths smaller than 4*mm* may have been influenced by this effect.

Present findings contrast with Monismith *et al.* (2007) results who challenged the validity of Stokes theories. They compared several tank experiments of waves propagating in closed tanks and over currents and found that, in most cases, the Lagrangian drift is cancelled locally (i.e. not in an integral sense) by a mean negative Eulerian velocity. Furthermore, they indicated that irrotational theories that predict a Lagrangian drift may not be adequate and postulated that the Gerstner rotational wave theory may provide a better representation of inferred closed orbital motion from the wave tank experiments they compared. Their conclusions were drawn from a compilation of fixed-point laboratory observations of waves running for long periods of time. It is plausible that the significant differences between those experiments and the present observations may have been caused by effects such as the previously discussed Longuet-Higgins (1953) vorticity diffusion and the vorticity convection from boundaries, as pointed out by Swan (1990b) for long running time experiments in wave tanks.

Fenton (1985) published a fifth order Stokes wave theory that considers a correction for waves propagating on a mean current which accurately describes velocity fields and particle motion for steep non breaking waves, including the observed open orbital motion. This is consistent with measurements by Swan (1990a) who also compared his laboratory measurements of surface elevation and velocity with Fenton (1985) fifth order theory, finding also an excellent agreement.

Additional to the discussion on the mean flow induced by waves it is important to note the range of the validity of the Stokes drift formula in equation (2-5). The original formula was derived by Stokes (1847) for deepwater waves using a first order Taylor expansion for a particle parcel with circular trajectory. The velocity field and the particle positions used in the derivation are similar to the expressions given by the linear (Airy) theory (Table 2-2). However, this appears contradictory with the conventional understanding on linear theory particle orbits (Wiegel 1964).

5.3.5 Continuous measurements of surface elevations and subsurface velocities

Continuous preliminary wave and velocity measurements have been included to complement the results obtained from the dye measurements. These complementary measurements are long time series observations under steady conditions of waves running for extended periods that may induce effects such as the Longuet-Higgins (1953) vorticity diffusion and Swan (1990b) vorticity convection from boundaries.

ADV velocity measurements (see sections 3.4 and 5.2.3) showed a general good agreement with Fenton (1985) fifth order theory, yet higher harmonics appear underestimated in the velocity field. The velocity spectrum in Figure 5-11 shows no evidence of turbulence adding to the findings with the dye measurements. The ADV focusing depth of z=-0.03m was chosen to match Babanin and Haus (2009) PIV measurement depth.

Wave measurements carried out in a calibration stage including waves of different steepnesses (ω=9.42$rads^{-1}$, d=0.405m) also showed an underestimation of the higher harmonics (Figure 5-12). Water elevation time series of 36000 points sampled at

600*Hz* were recorded within a short time interval between measurements. Post processing was carried out as explained in section 3.3.

ADV and wave measurements enabled us to evaluate the Stokes coefficients directly by integrating the energy associated to the spectral harmonic peaks within a ±5% frequency band of the harmonic frequency. In the integration, the average spectral noise level in the neighbourhoods of the harmonic frequency band was removed. Spectral noise is most likely due to spectral leakage, an intrinsic characteristic of discrete FFT spectral analysis (Press *et al.* 1999, p.551). Only values with a signal to noise ratio greater than 3 were considered reliable and were included in Figure 5-13 and Figure 5-14.

A phase analysis of the higher harmonics detected in the water elevation spectra was carried out using the inverse FFT combined with a digital Gaussian band filter centred at each harmonic frequency (1^{st} to 5^{th} harmonic). The resulting filtered subharmonic time series were compared with the time series of the first harmonic. The phase difference was calculated by measuring the time of the peak of the subharmonics time series and comparing it with the peak time of the first harmonic obtaining a maximum phase difference of ±11% the fundamental wave period. This is in reasonable agreement with Stokes theories which require that all subharmonics are in phase with the fundamental frequency.

Figure 5-13 and Figure 5-14 show the harmonic coefficients compared with the Stokes theories using the equations and format given in Table 2-1 and Table 2-2 respectively.

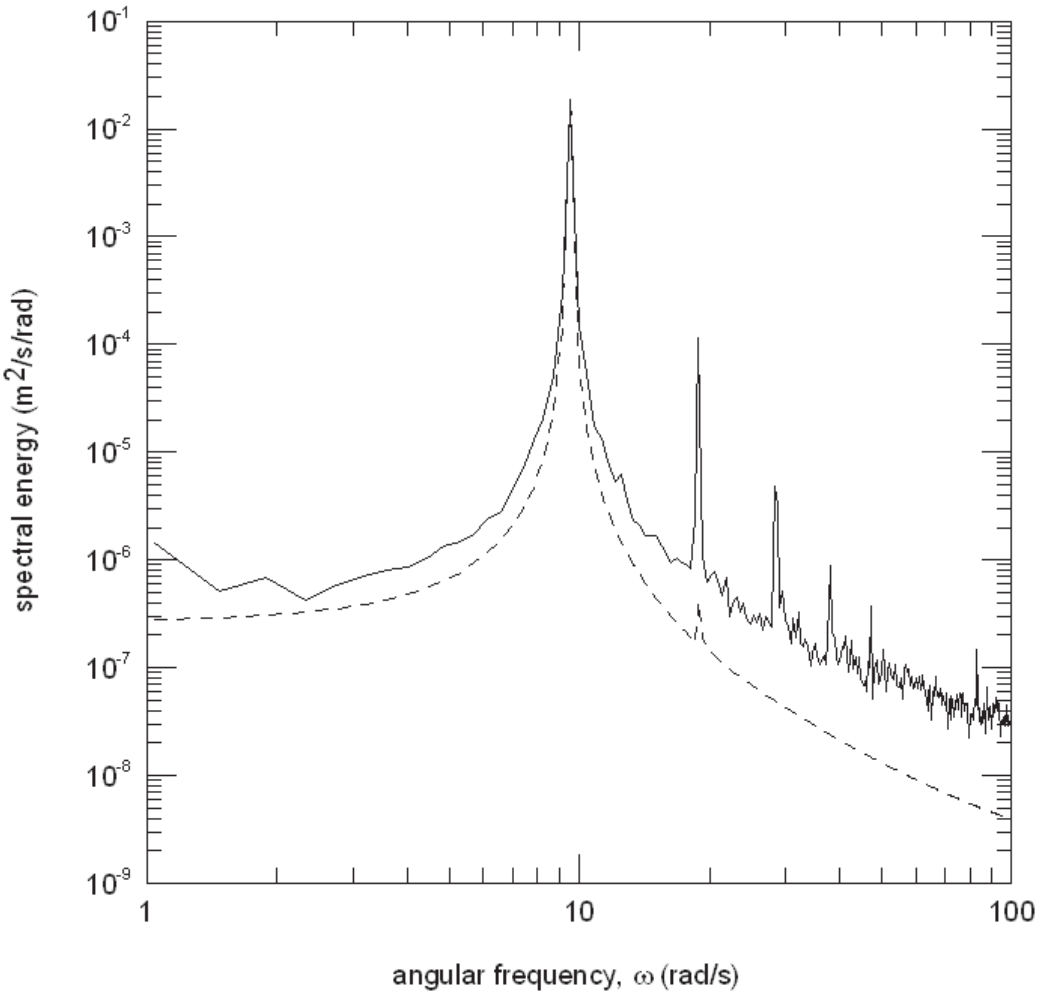

Figure 5-11: Autospectra of the vertical velocity (ξ=0.17, *w*, the least noisy ADV velocity coordinate, solid line) compared with the vertical velocity given by the fifth order Stokes theory (dashed line).

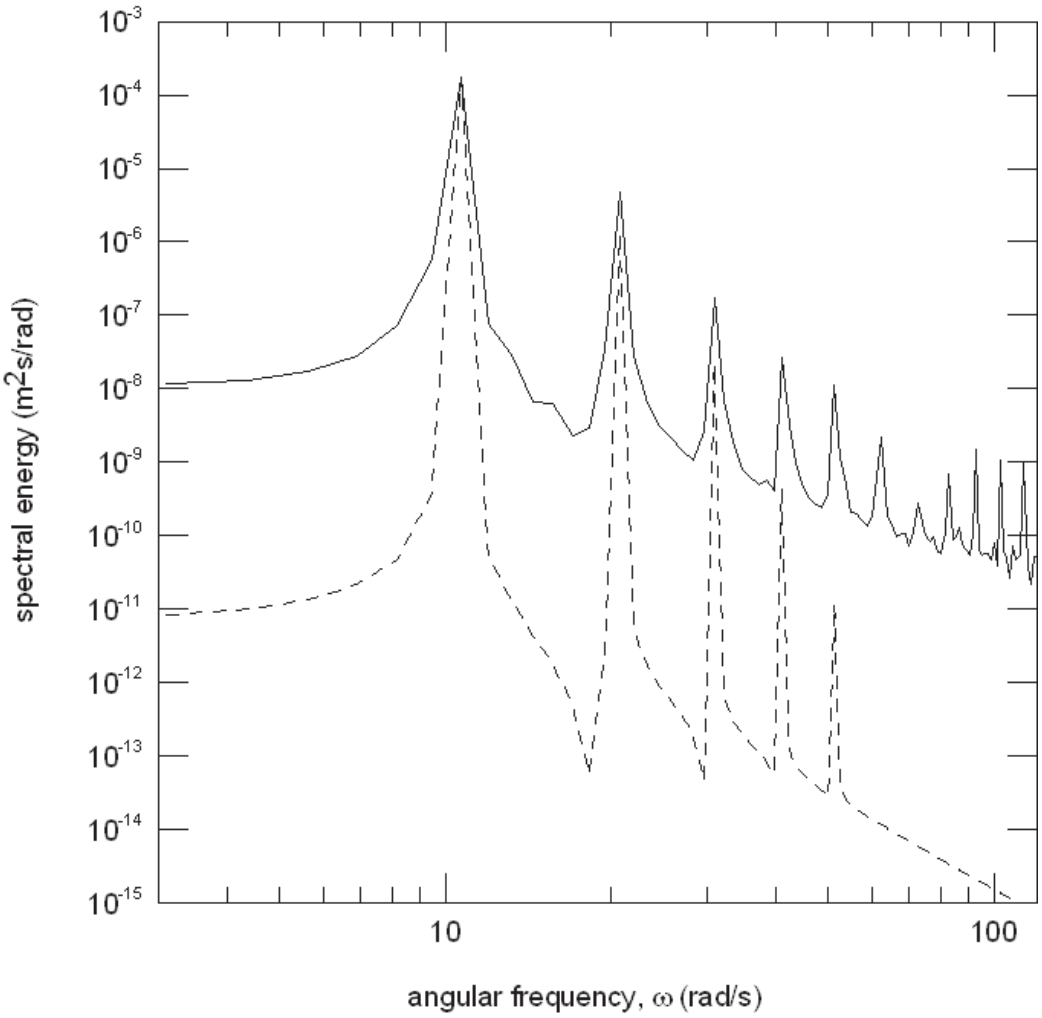

Figure 5-12: Autospectra of the measured water elevation (solid line) compared with the fifth order prediction (dashed line), ξ=0.17. FFT calculated from a 600*Hz*, 2^{15} points timeseries. Values were smoothed with 11 bin averages.

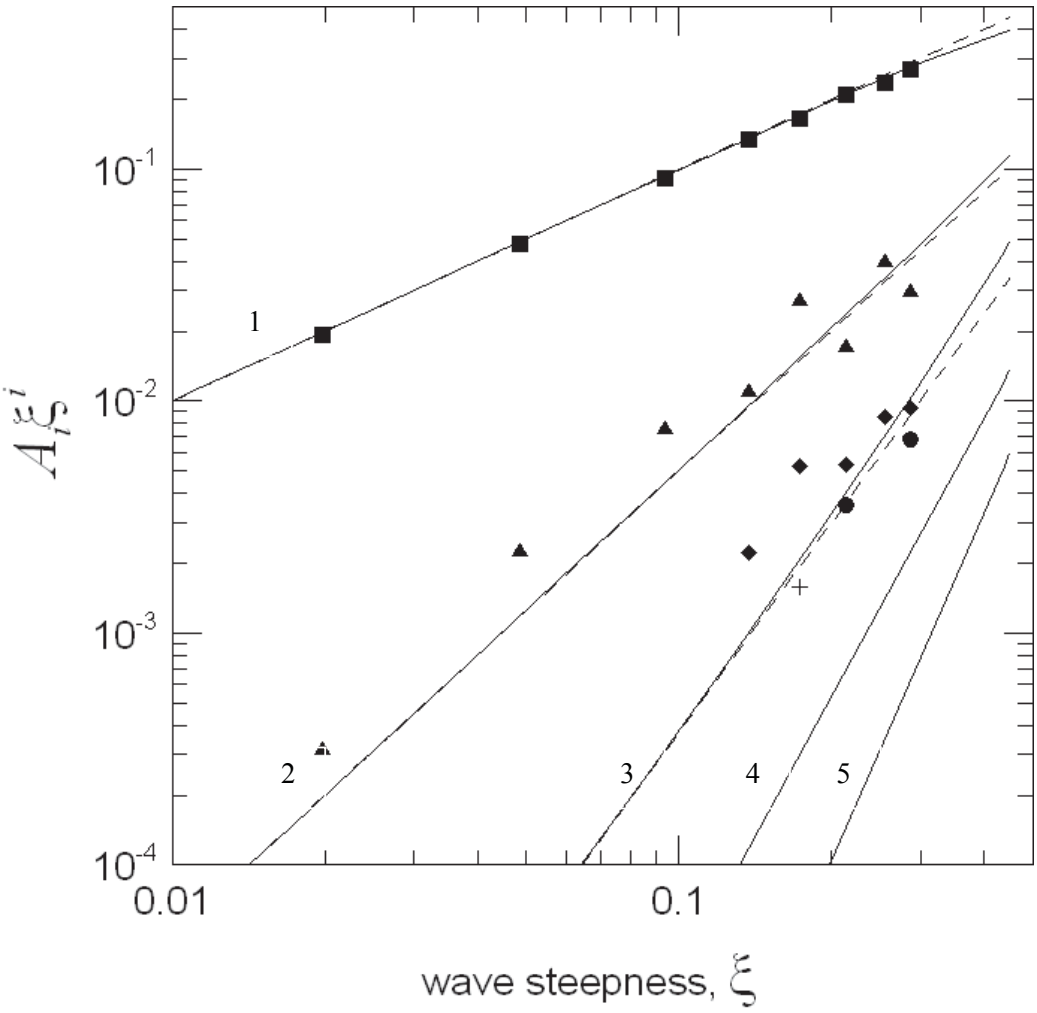

Figure 5-13: Measured and predicted surface elevation harmonic coefficients as a function of wave steepness following description in Table 2-1. Measured harmonics 1st (squares), 2nd (triangles), 3rd (diamonds), 4th (circles), 5th (crosses). Solid line Fenton (1985), Dashed lines lower order predictions when different from Fenton (1985), the '*i*' index represents the subharmonic number in the vertical axis caption.

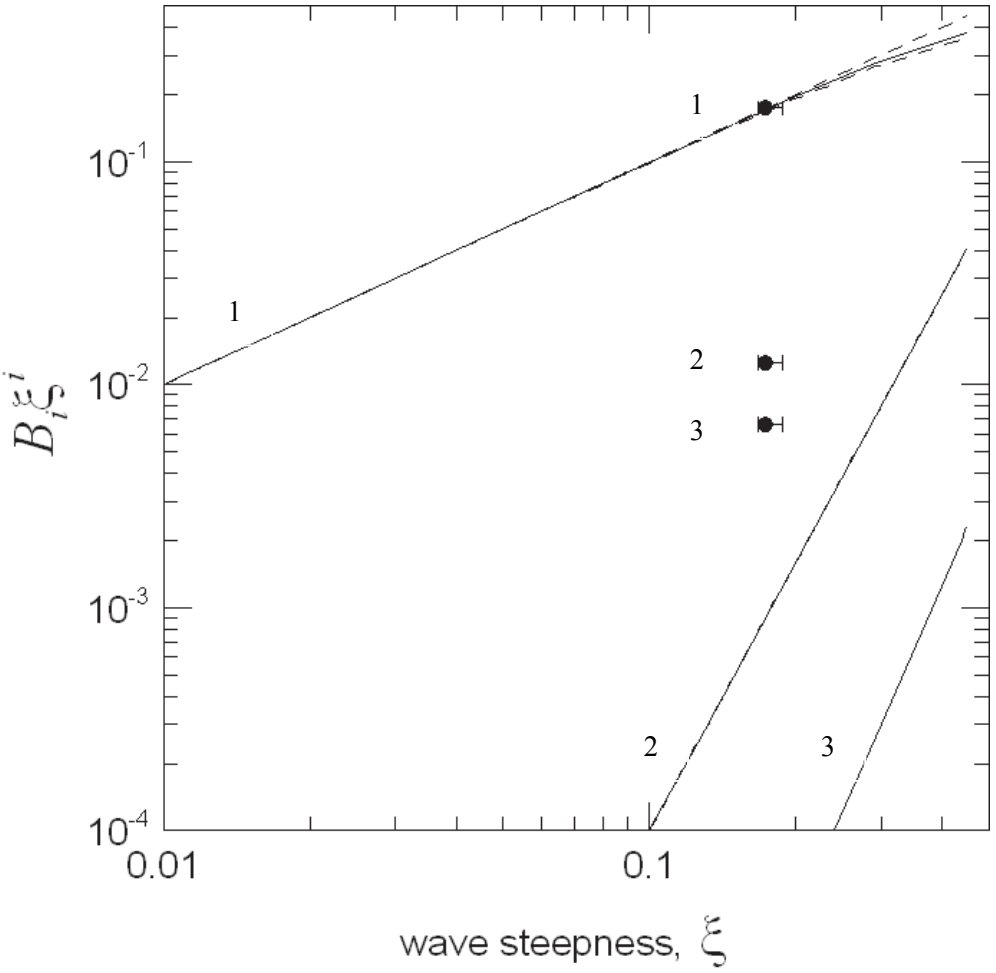

Figure 5-14: Measured and predicted velocity harmonic coefficients as a function of wave steepness following description in Table 2-2. Measured harmonic coefficients (circles). Solid line Fenton (1985), Dashed lines lower order prediction when different from Fenton (1985), the '*i*' index represents the subharmonic number in the vertical axis caption.

6 CONCLUSIONS AND RECOMMENDATIONS FOR FUTURE WORK

This thesis consisted of two sets of tank laboratory experiments where the interaction of deep water waves and turbulence was investigated: In the first set, detailed in Chapter 4, wave attenuation and velocity fluctuations induced by rainfall were measured. In the second, detailed in Chapter 5, flow visualizations measurements using dye were carried out for non-breaking surface gravity waves. The main accomplishments and recommendations for future work derived from each of these experimental studies are detailed below.

6.1 Wave attenuation due to rainfall-generated surface turbulence

Measured wave attenuation induced by surface generated turbulence was significantly greater than the expected from the Teixeira and Belcher (2002) theoretical predictions, a fact also pointed by Peirson *et al.* (2003). This theory has been recently incorporated in wave propagation models to include explicitly the effect of turbulence in wave energy dissipation (Ardhuin and Jenkins 2006, Tolman 2009). It is based on the Hunt and Graham (1978) turbulence profile which is significantly different from the conditions found in the ocean where turbulence is generated at the surface and diffused downwards (Craig and Banner 1994). Further, the theory validation was carried out with laboratory experiments by Olmez and Milgram (1992) who used grid generated turbulence, a mechanism also significantly different from the conditions in the ocean.

During the rainfall experiments, the water surface is disrupted by impinging raindrops which generate complicated features that are markedly different from those

generated by white-capping and surface wind shear during ocean storms. The effect that these different features may have in the wave attenuation process has not been investigated in detail in this study. Theoretical estimates of wave attenuation due to turbulence (e.g. Teixeira and Belcher 2002) neither account for this effect. However, the roughness length (z_0) in the Craig and Banner (1994) ocean turbulence diffusion model, offers a parametric representation of the length scale of the fluid depth influenced by the surface disruption.

Only recently have wave propagation models incorporated turbulence attenuation explicitly in the energy source-sink terms (Tolman 2009). Conventionally wave-turbulence interactions have been implicitly included in the generation and dissipation terms (wind generation, white-capping and wave breaking). There is potential for significant improvements in wave propagation models if ocean turbulence can be appropriately identified and characterised separately from the wave generation and dissipation processes. However theoretical parameterizations of the wave attenuation coefficient are very sensitive to turbulence intensities. This added to the complexity in the measurement and estimation of the turbulence statistics from the forcing parameters, especially near the surface. It introduces serious challenges in the application of such parameterizations in practical wave modelling. The inclusion of an explicit turbulence source-sink term will require modifications in the generation and dissipation terms.

Difficulties in the measurement and characterization of the turbulence in the ocean as well as in generating laboratory conditions representative of the processes in the sea still presents a major challenge. Attempts undertaken in this investigation using rainfall as a turbulence generation mechanism were partially unsuccessful due to the low levels and the low dynamic range of the observed subsurface turbulence in spite of

the high levels and wide range of the kinetic energy input (rainfall rate) supplied in the experiments.

Nevertheless, observed low levels of rainfall generated subsurface velocity fluctuations were successfully compared with Braun (2003). Conversely, these observations showed significant differences with extensive investigations on air-sea gas transfer (e.g. Ho *et al.* 2000) where a direct energy transfer from rainfall to subsurface turbulence has been long assumed. Recent observations of strong levels of turbulence under rainfall by Zappa *et al.* (2009) support this hypothesis. This is contrary to the conclusions of the present study and all the evidence presented showing that the energy transfer from the rain to subsurface turbulence is a very inefficient process.

The attenuation of waves by rainfall is of fundamental importance for radar-scatterometer wave measurements. The observed invariability with respect to the rainfall kinetic energy in the wave attenuation and the subsurface turbulence should be of primary importance for investigators focused in this area.

Thus, the following recommendations for future work in this topic are given:

- Design and undertake wave-turbulence attenuation experiments for a stronger and a wider range of turbulence intensities which shall be generated at the water surface to emulate the turbulence generation mechanism in the ocean. Turbulence measurements should be compared with wind-wave and wave-breaking turbulence studies (e.g. Cheung and Street 1988, Rapp and Melville 1990) in order to extend the results for wind and locally-forced wave breaking-generated turbulence.
- Revise the Teixeira and Belcher (2002) model including a modification of the theoretical analysis by replacing the existing turbulence profile for one representative of the conditions in the ocean (such as the Craig and Banner 1994

model). The theory validation shall require complementary laboratory and field observations.

- Evaluate the practical use of explicitly integrating turbulence wave attenuation in the wave propagation models by following the work of Ardhuin and Jenkins (2006) but considering that present models include turbulence effects implicitly in the generation and dissipation terms. Appropriate scaling parameters for turbulence intensities, lengths and times should be considered when transferring results from laboratory experiments to larger scales in the ocean.
- Investigate the influence in wave attenuation of the surface roughness generated in the sea and in the laboratory by the turbulence generation mechanism, considering that different water surface conditions attenuate waves at significantly different rates (section 4.5.2, van Dorn 1966) and that different turbulence generation mechanisms generate different surface roughness, air entrainment and other features.
- Quantify the energy transfer in the first few centimetres of the air-gas interface under rainfall where a significant proportion of the energy appears to be dissipated by poorly understood, although complex processes where rain generated surface waves and turbulence magnitudes appear insensitive to variations in the rainfall rate.
- Reanalyse the valuable turbulence measurements undertaken by Zappa *et al.* (2009) in order to reconcile the results with the present study and all the evidence showing that the transfer of rainfall kinetic energy to subsurface turbulence is an inefficient process. The methodology used in this study to extract weak turbulent velocity fluctuations from ADV measurements where the noise may induce a significant bias, may be used as guideline. Investigations on gas transfer at the air-sea interface may find these results useful.

6.2 Non-turbulent flow under non-breaking waves

Unique direct dye measurements of near surface motion beneath steep gravity waves in the absence of breaking and wind forcing confirmed the conventional understanding by showing absence of turbulence beneath waves. Present observations are contrary to Babanin and Haus (2009) who found levels of turbulence under the wave troughs comparable to conditions under strong winds (Terray *et al.* 1996). They proposed the appearance of turbulence above the threshold parameter $a^2\omega/\nu$=3000 for freely propagating waves.

Furthermore, the stretching of the dye filaments induced by the wave induced forward motion evidenced in the preliminary tests inspired a comparison between the mean velocity profiles and the Stokes drift formula. Theory and experiments compared reasonably well, yet the theory systematically overestimates in approximately 20% the near the surface observations.

Wave orbital velocities and particle paths obtained from the dye visualizations are in excellent agreement with Fenton (1985) fifth order theory showing that Stokes irrotational wave theories can adequately predict non-linear wave motion.

Measured mean return velocity ($\bar{U}$) induced by the Stokes drift in a closed tank is also in excellent agreement, within 5% of the values computed from Fenton (1985) theory. Further, the assumption of a uniform $\bar{U}$ in the vertical, a hypothesis originated in the 1940s (Wiegel 1964, p.32), yielded adequate results when combined with Fenton (1985) and the Stokes drift formula.

These experimental evidence is in contrast with Monismith *et al.* (2007) who compared a compilation of wave laboratory experiments, for which waves have been running for a long time, and found that the Stokes drift was cancelled locally by a return current. From this result they inferred that particles moved in closed orbits and proposed

a plausible re-examination of the Gerstner (rotational) waves as a replacement for the Stokes irrotational theory. The experiments compared by Monismith *et al.* (2007) may have significant differences with the present observations with rotational flow effects such as those observed by Longuet-Higgins (1960) and Swan (1990b).

Complementary continuous wave and velocity measurements were compared with higher order Stokes theories showing also an excellent agreement. These measurements, in comparison with the dye observations, involved waves propagating for longer periods and may be subject to the effects of the Longuet-Higgins (1953) vorticity diffusion. Spectral analysis of these measurements showed that Stokes theories consistently underestimate non-linearities which are evidenced in the theoretical under prediction of the subharmonic coefficients.

It appears that, at least for the range of steepnesses tested in this study, the fourth and fifth order Stokes coefficients are not of primary importance in predicting water elevations and velocities. Second and third order theories may provide with an adequate description when used in combination with the description of the wave number and horizontal velocity for steep waves propagating on a mean current introduced by Fenton (1985) which significantly improves the performance of conventional Stokes theories.

Thus, the following recommendations for future work in this topic are given:

- Reconcile Monismith *et al.* (2007) conclusions with the present investigation considering that the testing conditions of the experiments they compared were different and may include rotational effects induced by long running time experiments. If Monismith *et al.* (2007) findings are confirmed, a revision of the Teixeira and Belcher (2002) model should be undertaken considering that the basis of their theory is on the strain created by the wave induced Stokes drift on the turbulence.

- Measure the Stokes coefficients for the surface elevation and the velocity field for a wider range of waves and compare them with theoretical predictions. The present comparison shows a consistent under prediction of the higher harmonics by the theory.

7 REFERENCES

1. Acton F. S., 1959, Analysis of Straight-Line Data. Wylie.
2. Agrawal Y. C., E. A. Terray, M. A. Donelan, P. A. Hwang, A. J. Williams, W. M. Drennan, K. K. Kahma and S. A. Kitaigorodskii, 1992, Enhanced dissipation of kinetic energy beneath surface waves, Nature 359: 219–220.
3. Anis A. and J. N. Moum, 1995, Surface wave–turbulence interaction: Scaling ε (z) near the sea surface, J. Phys. Oceanogr., 25:2025–2045.
4. Ardhuin F. and Jenkins A. D., 2006, On the interaction of surface waves and upper ocean turbulence. J. Phys. Oceanogr., 36:551-557.
5. Banner, M. L. and D. H. Peregrine, 1993, Wave breaking in deepwater, Annu. Rev. Fluid Mech., 25:373–397.
6. Banner M. L. and Peirson W. L., 2007, Wave Breaking Onset and Strength for two-dimensional deep-water wave groups, J. Fluid Mech., 585: 93–115.
7. Benjamin, T.B. and Feir, J.E., 1967, The disintegration of wavetrains in deep water, Part 1, J. Fluid Mech., 27: 417-430.
8. Bliven L., Sobieski P. and Craeye C., 1997, Rain generated ring-waves: measurements and modelling for remote sensing. Int. J. Remote Sensing, 18-1: 221-228.
9. Boussinesq J., 1872, Théorie des ondes et des remous qui se propagent le long d'un canal rectangulaire horizontal, en communiquant au liquide contenu dans ce canal des vitesses sensiblement pareilles de la surface au fond. Journal de Mathématique Pures et Appliquées, Deuxième Série, 17: 55-108.
10. Boyev A. G., 1971, The damping of surface waves by intense turbulence, Izv. Atmos. Ocean Phys., 7: 31-36.

11. Bradshaw P., 1971, An introduction to Turbulence and its Measurement, Pergamon Press, First edition.
12. Braun N., Gade M., and Lange P.A., 2002, The effect of artificial rain on wave spectra and multi-polarisation X band radar backscatter, Int. J. Remote Sens., 23:4305-4322.
13. Braun N., 2003. Untersuchungen zur Radar-Rückstreuung und Wellendämpfung beregneter Wasseroberflächen, Dissertation, Universität Hamburg, Fachbereich Geowissenschaften ."On the Radar Backscattering and Wave Damping on Water Surfaces Agitated by Rain", Dissertation thesis, Hamburg University, Geoscience department.
14. Burchard H., Craig P., Gemmrich J., van Haren H., Mathieu P., Meier H.E., Smith W., Prandke H., Rippeth T., Skyllingstad E., Smyth W., Welsh D., Wijesekera H., 2008, Observational and numerical modeling methods for quantifying coastal ocean turbulence and mixing, Progress In Oceanography, 76-4: 399-442.
15. Chang K-A. and Liu PL-F., 1999, Experimental investigation of turbulence generated by breaking waves in water of intermediate depth, Phys. Fluids, 11-11: 3390-3400.
16. Chang K-A. and Liu PL-F., 2000, Pseudo turbulence in PIV breaking-wave measurements, Exp Fluids, 29:331–338.
17. Cheung T.K. and Street R.L., 1988, The turbulent layer in the water at an air–water interface, J. Fluid Mech., 194:133–151.
18. CEM2008, U.S. Army Corps of Engineers, 2008. Coastal Engineering Manual. Engineer Manual, U.S. Army Corps of Engineers, Washington, D.C., (in 6 volumes).

19. Constantin A. and Strauss W., 2004, Exact steady periodic water waves with vorticity, Communications on Pure and Applied Mathematics, LVII:0481–0527, Wiley Periodicals, Inc.
20. Constantin A., 2006, The trajectories of particles in Stokes waves, Invent. math., 166, 523-535.
21. Constantin A. and Villari G., 2006, Particle Trajectories in Linear Water Waves, J. Math. Fluid Mech., 10:.1-18.
22. Craeye C., and Schlussel P., 1998, Rainfall on the sea: Surface renewals and wave damping, Boundary Layer Meteorol., 89: 349 – 355.
23. Craig P. and Banner M., 1994. Modelling wave-enhanced turbulence in the ocean surface layer. J. Phys. Oceanogr., 24:2546–2559.
24. Craig P. 1996, Velocity profiles and surface roughness under breaking waves, J. Geophys .Res., 101:1265–1277.
25. Drazen D. A. and Melville W. K., 2009. Turbulence and mixing in unsteady breaking surface waves, J. Fluid Mech., 628: 85–119.
26. Duncan, J. H., 1983. The breaking and non-breaking wave resistance of a two-dimensional hydrofoil, J. Fluid Mech., 126: 507-520.
27. Fenton J., 1985, A fifth-order stokes theory for steady waves, J. Waterw. Port Coast. Ocean Eng, 111: 216-234.
28. Foken Th., Kitajgorodskij S.A., Kuznecov O.A., 1978, On The Dynamics Of The Molecular Temperature Boundary Layer Above The Sea, Boundary-Layer Meteorology, 15: 289-300.
29. Foster J., 1999, On the action of rain in Calming the sea and generating Sea Surface Roughness, Proceedings of IGARSS '99 Hamburg Germany: IEEE 1999 International Geoscience and Remote Sensing Symposium.

30. Garcia C., Cantero M., Rehnmann C. and Garcia M., 2004, New methodology to subtract noise effects from turbulence parameters computed from ADV velocity signals, Proceedings of the 2004 World Water and Environmental Resources Congress, ASCE 2004.
31. Garcia C., Jackson R., Garcia M., 2006, Confidence intervals in the determination of turbulence parameters, Research article, Exp. Fluids, 40: 514-522.
32. Gemmrich J. and Farmer D., 2004, Near-surface turbulence in the presence of breaking waves, J. Phys. Oceanogr., 34: 1067–1086.
33. Green T., and Houk D. F., 1979, The mixing of rain with near-surface water, J. Fluid Mech., 90(3): 569–588.
34. Ho D. T., Asher W. E., Bliven L. F., Schlosser P., and Gordan E. L., 2000, On the mechanisms of rain-induced air-water gas exchange, J. Geophys .Res., 105(C10):24045–24057.
35. Hornbeck R.W., 1974, Numerical Methods. Quantum Publications, New York, NY.
36. Houk D. F., and T. Green, 1976, A note on surface waves due to rain, J. Geophys. Res., 81:4482-4484.
37. Hristov T. S., Miller S. D. and Friehe C. A, 2003, Dynamical coupling of wind and ocean waves through wave-induced air flow, Nature, 422: 55-58.
38. Hughes S.A., 1993, Physical Models and Laboratory Techniques in Coastal Engineering, Advanced Series on Ocean Eng., Vol. 7, World Scientific Publ., Singapore.
39. Hunt, J.N., 1952. Viscous damping of waves over an inclined bed in a channel of finite width, Houille Blanche, 7:836-842.
40. Hunt J. and Graham J., 1978, Free-stream turbulence near plane boundaries, J. Fluid Mech. 84: 209–235.

41. Jahne B. and Haußecker H., 1998, Air-water gas exchange. Annu. Rev. Fluid Mech., 30:443–68.

42. Janssen P., 2004, The Interaction of Ocean Waves and Wind, Cambridge University Press.

43. Jiang L., Perlin M. and Shultz W., 1998, Period tripling and energy dissipation of breaking standing waves, J. Fluid Mech., 369: 273-299.

44. Kinsman B., 1984, Wind waves, their generation and propagation on the ocean surface, Dover publications, inc. New York.

45. Lange P.A., G. van der Graaf, and Gade M., 2000, Rain-Induced Subsurface Turbulence Measured Using Image Processing Methods, Proceed. Intern. Geosci. Remote Sens. Sympos. (IGARSS) '00, IEEE, Piscataway, NJ, USA, 3175-3177.

46. Lamb H., 1932, Hydrodynamics, Cambridge University Press.

47. Le Méhauté B., and Khangaonkar T., 1990, Dynamic Interaction of Intense Rain with Water Waves J. Phys. Oceanogr., 20: 1805-1812.

48. Longuet-Higgins M. S., 1953, Mass Transport in Water Waves, Phil. Trans. R. Soc. Lond. A, March 31, 245:535-581.

49. Longuet-Higgins M. S., 1960, Mass transport in the boundary layer at a free oscillating surface, J. Fluid Mech., 8: 293–306.

50. Magnaudet J., and Thais L., 1995, Orbital rotational motion and turbulence below laboratory wind water waves, J. Geophys. Res., 100(C1): 757–771.

51. Manton M. J., 1973, On the attenuation of sea waves by rain, J. Geophys. Fluid Dyn., 5:249-260.

52. Mitsuyasu H. and Honda T., 1982, Wind-induced growth of water waves, J. Fluid Mech, 123: 425–442.

53. Nikora V. and Goring D., 1998, ADV Measurements of Turbulence: Can We improve Their Interpretation?, J. Hydr. Engrg. 124-6: 630-634. ASCE.

54. Nystuen J., 1990, A note on the attenuation of surface gravity waves by rainfall, J. Geophys.Res., 95: 18353-18355.

55. Olmez H. and Milgram J., 1992, An Experimental study of attenuation of Short Water Waves by Turbulence, J. Fluid Mech., 238:133-156.

56. Peirson W. L., 1997, Measurement of surface velocities and shears at a wavy air-water interface using particle image velocimetry, Exp. Fluids 23: 427-437.

57. Peirson W. L., Garcia A. W. and Pells S .E., 2003, Water wave attenuation due to opposing wind, J. Fluid Mech., 487: 345-365.

58. Peregrine D.H. and Svendsen L.A., 1978, Spilling breakers, bores and hydraulic jumps. In: (2nd ed.), Proc. 16th Inter. Conf. Coastal Engng. 1, 540–550.

59. Phillips O. M., 1977, The Dynamics of the Upper Ocean, Cambridge University Press, second edition.

60. Poon Y., Tang S. and Wu J., 1992, Interactions Between Rain and Wind Waves, J. Phys. Oceanogr., 22: 976-987.

61. Pope S., 2000, Turbulent flows, Cambridge University Press.

62. Rapp R. J. and Melville W. K., 1990, Laboratory measurements of deep water breaking waves, Phil. Trans. R. Soc. A, 331:735–800.

63. Reynolds O., 1874, On the Action of Rain to Calm the Sea, Fourteenth volume of the Proceedings of the literacy and philosophical society of Manchester, Session 1874-5.

64. Reynolds O., 1883, An experimental investigation of the circumstances which determine whether the motion of water shall be direct or sinuous, and of the law of resistance in parallel channels, Phil. Trans. R. Soc. Lond., 174: 935-982.

65. Richardson L.F., 1922, Weather Prediction by Numerical Process, Cambridge: Cambridge University Press.

66. Segur H., Henderson D., Hammack, Lia J., C. Pheiff D., Sochac K., 2004, Stabilizing the Benjamin-Feir instability, J. Fluid Mech., 539: 229–271.

67. Shelton C.H., von Bernuth R. D., Rajbhandari S.P., 1985, A Continuous Application Rainfall Simulator, American Society of Agricultural Engineers, Vol 28(4), Paper N 84-2049.

68. Sheng J., Meng H., Fox R. O., 2000, A large eddy PIV method for turbulence dissipation rate estimation, Chemical Engineering Science, 55: 4423-4434, Pergamon-Elsevier science Ltd.

69. Skjelbreia L. and Hendrickson J., 1961, Fifth order gravity wave theory, Proceedings 7th conference of coastal engineering, 184-196.

70. SPM84, Shore Protection Manual, 1984, 4th ed., 2 Vol., U.S. Army Engineer Waterways Experiment Station, U.S. Government Printing Office, Washington, D.C.

71. Soloviev A. and Lukas R., 2006, The Near Surface Layer of the Ocean, Atmospheric and Oceanographic Sciences Library, Springer.

72. Swan C., 1990[a], Wave kinematics within the crest to trough region, Environmental forces on offshore Structures and their Prediction, 26: 45-60, Dept. of Civil Eng., Imperial College, London, SW7 2BU.

73. Swan C., 1990[b], Convection within an experimental wave flume, J. Hydraul. Res., 28: 273-282.

74. Takagaki N., Komori S., 2007, Effects of rainfall in mass transfer across the air-water interface, J. Geophys. Res., 112- C06006.

75. Teixeira M. A. C. and Belcher S.E., 2002, On the Distortion of Turbulence by a Progressive Surface Wave. J. Fluid Mech. 458: 229-267.

76. Tennekes H. and Lumley J. L., 1972, A First course in Turbulence, 15th printing MIT Press Design Department.

77. Terray, E. A., M. A. Donelan, Y. C. Agrawal, W. M. Drennan, K. K., Kahma, A. J.Williams III, P. A. Hwang, and S. A. Kitaigorodskii, 1996, Estimates of kinetic energy dissipation under breaking waves, J. Phys. Oceanogr., 26: 792–807.

78. Thorpe S.A., 1995, Dynamical processes of transfer at the sea surface, Prog. Oceanog. Vol., 35: 315-352.

79. Thorpe S.A., 2005, The Turbulent Ocean, Cambridge University Press

80. Tolman H., 2009, User manual and system documentation of WAVEWATCH III TM version 3.14., Technical note, MMAB Contribution No. 276. NOAA.

81. Tsimplis M.N., 1992, The effect of Rain in calming the Sea, J. Phys. Oceanogr., 22: 404-412.

82. Voulgaris G. and Trowbridge J., 1998, Evaluation of the acoustic Doppler velocitmeter (ADV) for Turbulence Measurements, J. Atmos. Ocean Tech., 15:272-289. American Meteorological Society.

83. Van Dorn W.G., 1966, Boundary dissipation of oscillatory waves, J.Fluid Mech. 24:769-779.

84. Vennard J. and Street R., 1976, Elementary Fluid Mechanics, SI version, fifth edition, Wiley editorial.

85. Wiegel R. L., 1964, Oceanographical Engineering. Prentice-Hall International in theoretical and Applied Mechanics, N. M. Newmark editor.

86. Zappa C. J., D. T. Ho, W. R. McGillis, M. L. Banner, J. W. H. Dacey, L. F. Bliven, B. Ma, and J. Nystuen, 2009, Rain-induced turbulence and air-sea gas transfer, J. Geophys. Res., 114: C07009.